Advanced Topics in Science and Technology in China

Yi Hong
Lizhong Wang

Deformation and Failure Mechanism of Excavation in Clay Subjected to Hydraulic Uplift

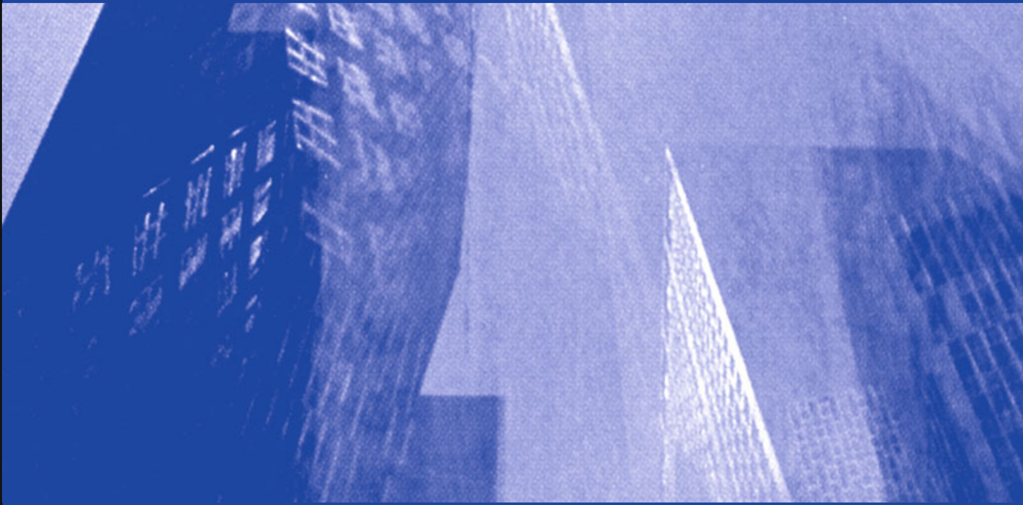

ZHEJIANG UNIVERSITY PRESS
浙江大学出版社

Springer

Advanced Topics in Science and Technology in China

Zhejiang University is one of the leading universities in China. In Advanced Topics in Science and Technology in China, Zhejiang University Press and Springer jointly publish monographs by Chinese scholars and professors, as well as invited authors and editors from abroad who are outstanding experts and scholars in their fields. This series will be of interest to researchers, lecturers, and graduate students alike.

Advanced Topics in Science and Technology in China aims to present the latest and most cutting-edge theories, techniques, and methodologies in various research areas in China. It covers all disciplines in the fields of natural science and technology, including but not limited to, computer science, materials science, life sciences, engineering, environmental sciences, mathematics, and physics.

More information about this series at http://www.springer.com/series/7887

Yi Hong · Lizhong Wang

Deformation and Failure Mechanism of Excavation in Clay Subjected to Hydraulic Uplift

ZHEJIANG UNIVERSITY PRESS
浙江大学出版社

Springer

Yi Hong
College of Civil Engineering
and Architecture
Zhejiang University
Hangzhou, Zhejiang
China

Lizhong Wang
College of Civil Engineering
and Architecture
Zhejiang University
Hangzhou, Zhejiang
China

ISSN 1995-6819 ISSN 1995-6827 (electronic)
Advanced Topics in Science and Technology in China
ISBN 978-3-662-46506-6 ISBN 978-3-662-46507-3 (eBook)
DOI 10.1007/978-3-662-46507-3

Library of Congress Control Number: 2015956360

Printed on acid-free paper

This Springer imprint is published by SpringerNature
The registered company is Springer-Verlag GmbH Berlin Heidelberg

Preface

Deep excavations in soft clay with an underlying aquifer lead to major concerns of ground deformation, soil–structure interaction and base instability due to hydraulic uplift. Given vast amount of case histories reported in the literature, it is still difficult to differentiate and understand ground deformations induced by excavations in densely built urban areas and greenfield sites. Moreover, reliable measurements of earth pressure on walls in excavations in soft clay are rarely reported. In spite of frequently reported base instabilities due to hydraulic uplift, the initiation and failure mechanism of base instability are not systematically investigated and well understood. Existing calculation methods against base instability may be too conservative and reserved to be improved.

As far as the authors are aware, this is the first book to present and interpret state-of-the-art experimental and theoretical work on ground deformation and base instability of deep excavations in soft clay subjected to hydraulic uplift. The technical contents of the book are condensed from the authors' most recent comprehensive research work carried out on the subject, based on dimensional analyses, well-instrumented full-scale field tests, systematic coupled-consolidation finite element analyses and state-of-the-art centrifuge tests.

To study ground deformation and soil–structure interaction, a diaphragm wall panel constructed at a greenfield site in Shanghai soft clay was comprehensively instrumented and monitored. Coupled-consolidation finite element analysis was conducted to back-analyse the case history. Moreover, a parametric study was carried out to investigate, understand and quantify key factors governing relatively small excavation-induced ground deformation in Shanghai. To study base instability due to hydraulic uplift, a new experimental setup was developed to simulate in-flight multi-propped excavation destabilised by hydraulic uplift in centrifuge. Centrifuge model tests and three-dimensional coupled-consolidation finite element analyses were carried out to investigate the initiation and failure mechanism of base instability due to hydraulic uplift in soft clay and effectiveness of using 'anti-uplift piles' for base stabilisation. Together with dimensional analysis and numerical parametric studies, key variables affecting the initiation and failure mechanism of base instability are indentified.

This book consists of ten chapters. Chapters 1, 9 and 10 were jointly authored by Prof. L.Z. Wang and Dr. Y. Hong. The remaining chapters were mainly completed by Dr. Y. Hong, by taking comments and suggestions from Prof. Charles Ng (Dr. Y. Hong's Ph.D. supervisor) and Prof. L.Z. Wang into account. The authors gratefully acknowledge the financial support from the Research Grants Council of the HKSAR (General Research Fund No. 617511), International S&T Cooperation Program of China (No. 2015DFE72830), National Natural Science Foundation of China (No. 51408540), National Science Foundation for Distinguished Young Scholars of China (No. 51325901), State Key Program of National Natural Science of China (No. 51338009) and China Postdoctoral Science Foundation (No. 2013M540494).

The authors would like to express deep appreciation to many colleagues who contributed to the research work presented in this book.

Finally, the authors are very grateful to their family members, for their love, encouragement and support.

Hangzhou, China
March 2015

Yi Hong
Lizhong Wang

Contents

Nomenclature

AL_{max}	Maximum axial load
σ_c	Concrete pressure
σ_h	Horizontal total earth pressure
$\sigma_{h\_0\ \mathrm{m}}$	Total horizontal earth pressure in front of the wall before excavation
$\sigma_{h\_8\ \mathrm{m}}$	Total horizontal earth pressure in front of the wall at the end of excavation
σ'_h	Horizontal effective earth pressure
σ'_{h0}	Horizontal effective earth pressure before excavation
σ_v	Vertical total earth pressure
σ'_v	Vertical effective earth pressure
σ'_{v0}	Vertical effective earth pressure before excavation
γ	Bulk unit weight of soil
γ_w	Bulk unit weight of water
γ_c	Bulk unit weight of concrete
γ_b	Bulk unit weight of bentonite slurry
γ_d	Dry density
γ_{clay}	Bulk unit weight of clay
α	Adhesion factor at clay–pile interface
h_{critical}	Critical depth of concrete pressure
d_p	Grain size of soil
D	Thickness of clay on the excavated side
z	Depth below surface ground
f_s	Unite shaft friction
H_e	Final excavation depth
L	Embedment depth of pile in sandy aquifer
$\delta_{v\text{-max}}$	Maximum ground surface settlement
$\delta_{h\text{-max}}$	Maximum lateral wall displacement
$\delta_{h\text{-max}(2\ \mathrm{m})}$	Maximum lateral ground displacement at 2 m behind the wall
$\delta_{h\text{-max}(13\ \mathrm{m})}$	Maximum lateral ground displacement at 13 m behind the wall
$\delta_{h\text{-}f}$	Lateral wall displacements at the formation level
N_c	Stability factor associated with excavation

N_{c_HU}	Stability factor associated with hydraulic uplift
W	Moisture content
W_p	Plastic limit
W_L	Liquid limit
c'	Effective cohesion
c_u	Vane shear strength
e	Void ratio
ϕ'	Effective angle of shearing resistance
δ'	Soil wall friction angle
E_s	Compressible modulus
K_o	At-rest lateral earth pressure coefficient
K_v	Saturated vertical permeability
K_h	Saturated horizontal permeability
F_R	Equivalent prop loads on the retained side
F_E	Equivalent prop loads on the excavated side
M	Stress ratio
M_R	Moment about top of the wall induced by equivalent prop loads on the retained side
M_E	Moment about top of the wall induced by equivalent prop loads on the excavated side
P_a	Artesian pressure
$P_{\max}$	The maximum hydraulic pressure the greased clay–model box interface can sustain
P_i	Pressure required to initiate hydraulic uplift
P_u	Ultimate hydraulic uplift pressure
Γ	Specific volume of the critical state line at unit pressure
λ	Slope of one-dimensional compression line in v-lnp' space
κ	Slope of unload-reload line in v-lnp' space
μ'	Possion’s ratio for effective stress analysis

Chapter 1
Introduction

1.1 Background

In recent decades, significant economic development in mega cities is driving the expansion of traffic demand, especially underground transportation. A large number of deep excavations have been carried out for underground metro stations.

One major concern relating to excavations in urban areas (especially in soft clay) is the possibility of excessive ground deformation induced by excavation. To date, numerical analysis is still not a promising tool for predicting excavation-induced ground deformations, partially due to lack of reliable constitutive model and soil parameters. Instead, semi-empirical studies based on measured data from large number of similar case histories would serve as a useful guideline. Over the past decades, database of excavation-induced ground deformations in soft clay from case histories worldwide (Peck 1969; Clough and O'Rourke 1990; Long 2001; Moormann 2004) and from local regions (Wang et al. 2005) are summarised and reported. Given the vast amount of case histories collected by various researchers, it is still not easy to differentiate and understand ground deformations induced by excavations in densely built urban areas and so-called greenfield sites. It is therefore of interest and worthwhile to investigate and compare ground deformations induced in a greenfield site and a conjested site influenced by underground structures and foundations nearby.

One essential issue for the design of a retaining wall for multi-propped excavations is the determination of the stress and deformation of the retaining wall and the axial load of props. The beam on elastic foundation analysis method is still commonly adopted in many parts of the world including Shanghai (Onishi and Sugawara 1999; Hu et al. 2003; Shao et al. 2005). It is widely recognised that this analysis is not able to account for stress redistribution in adjacent soil due to wall flexibility, and the accuracy of this analysis heavily relies on assumed earth pressures acting on the wall. To date, reliable field measurements of earth pressure on walls in excavations in soft clay are rarely reported. Since the actual earth pressures

Y. Hong and L. Wang, *Deformation and Failure Mechanism of Excavation in Clay Subjected to Hydraulic Uplift*, Advanced Topics in Science and Technology in China, DOI 10.1007/978-3-662-46507-3_1

acting on a retaining wall are governed by many factors such as ground conditions, construction method and sequence, stiffness of the retaining system, field measurement of earth pressures will be helpful to determine the earth pressures appropriate for practical designs. Besides, to assist with the design of prop loads, it will be useful to establish an apparent earth pressure envelope for excavations, based on extensive field measurements.

In many urban cities and countries worldwide such as Shanghai, Taipei, Singapore, Oxford, Mel bone and Toronto, stratified soil comprising of clay strata and sandy aquifers is frequently encountered. For excavations in clay underlain with a sub-aquifer, the subject is further complicated by introducing potential base instability due to hydraulic uplift. Catastrophic basal failures of excavations in clay subjected to hydraulic uplift have been frequently reported worldwide. Previous studies on this subject are mainly based on coarse field observations (Milligan and Lo 1970; Moore and Longworth 1979; Ramaswamy 1979; Clough and Reed 1984; Davies 1984; Qu et al. 2002; Gue and Tan 2004). Without accurate real-time measurement of uplift movement of clay inside excavation and artesian pressure in the aquifer, initiation of hydraulic uplift in all reported case histories still remain unknown. Neither can ground deformation mechanism within soil body during hydraulic uplift be observed from the field. Systematic study on the initiation and failure mechanism of excavation base instability due to hydraulic uplift are desired.

In current design guidelines worldwide, hydraulic pressure (P_i) required to initiate base instability is simply assumed to be equal to overburden pressure of clay inside excavation. This simple estimation may be over-conservative, as additional basal resistance (against hydraulic uplift) due to downward shear stress along soil-wall interface is not considered. Validity of P_i assumed in current design guidelines needs to be examined. It will be even more helpful to develop calculation chart for estimation P_i of excavations under different circumstances.

The most commonly used method to prevent base instability due to hydraulic uplift is releasing artesian pressure inside excavation within cut-off walls. This method is reported to be ineffective under some circumstance (Haydon and Hobbs 1977) and maybe time consuming and costly. Alternative methods, which are simpler but more effective for base stabilistaion, seem to be necessary.

1.2 Objectives

In view of the aforementioned issues, the major objectives of this study are:

- To improve understanding of ground deformation and soil-structure interaction of multi-propped excavation in soft clay;
- To investigate and understand the initiation and failure mechanism of excavation base instability due to hydraulic uplift;
- To propose and verify alternative ways for base stabilisation.

1.3 Book Outline

In addition to the introduction, this book is presented in 9 chapters, described as follows.

Chapter 2 reviews current understanding of ground deformation, soil-structure interaction and base instability (due to hydraulic uplift) of multi-propped excavation in soft clay. Major findings and limitations of the literature are presented and summerised. In addition, existing methods of simulating in-flight multi-propped excavation in centrifuge are reviewed.

Chapter 3 presents a field investigation of a multi-propped excavation in a greenfield site in Shanghai soft clay. Ground deformation and soil-structure interaction of the case history is documented, analysed and compared to similar excavations in densely built areas in Shanghai and other regions worldwide. Moreover, observed excessive basal heave in the case history raises concerns of base instability due to hydraulic uplift and leads to motivation of investigating this problem in Chaps. 5–9.

Chapter 4 back-analyses the case history documented in Chap. 3. Numerical parametric study is further carried out to investigate key factors governing excavation-induced ground deformation in Shanghai soft clay.

Chapter 5 presents dimensional analysis of excavation in soft clay subjected to hydraulic uplift. Key dimensionless groups (DGs) which are likely to be relevant to hydraulic uplift are indentified.

Chapter 6 describes development of a new experimental setup for simulation of in-flight multi-propped excavation in soft clay de-stabilised by hydraulic uplift. Program and objectives of centrifuge tests, model preparation and test procedure are also presented.

Chapter 7 describes finite element analyses for (a) back-analyses of centrifuge tests (results reported in Chap. 8) and (b) parametric study on the initiation and failure mechanisms of base instability (results reported in Chap. 9).

Chapter 8 presents interpretation of measured and back-analysed results of the centrifuge tests conducted. Improved understandings from numerical back-analyses are also presented.

Chapter 9 presents numerical parametric study on effect of key variables affecting the initiation and failure mechanisms of base instability.

Chapter 10 summarises research work conducted, major findings from each aspect of this present study and recommends future research.

References

Clough GW, O'Rourke TD (1990) Construction induced movements of in situ walls. Proceedings of the Design and Performance of Earth Retaining Structure, ASCE Special Conference, Ithaca, New York, pp 439–470

Clough GW, Reed MW (1984) Measured behaviour of braced wall in very soft clay. J Geotech Eng Div, ASCE, 110(1):1–19

Davies (1984) Some geotechnical problems with foundations and basements in Singapore. In: Proceedings of international conference on tall buildings, Singapore, 22–26 October

Gue SS, Tan YC (2004) Two case histories of basement excavation with influence on groundwater. Keynote Lecture, In: International Conference on Structural and Foundation Failures (ICSFF), Singapore, 2–4 August

Haydon REV, Hobbs NB (1977) The effect of uplift pressures on the performance of a heavy foundation on layered rock. In: Proceedings of conference on rock engineering. British geotechnical society and department of mining engineering, University of Newcastle, pp 457–472

Hu ZF, Yue ZQ, Zhou J, Tham LG (2003) Design and construction of a deep excavation in soft soil adjacent to the Shanghai Metro tunnels. Can Geotech J 40(5):933–948

Long M (2001). Database for retaining wall and ground movements due to deep excavation. J. Geotech Geoenviron Eng, ASCE, 127(3):203–224

Milligan V, Lo KY (1970) Observations on some basal failures in sheeted excavations. Can Geotech J 7(2):136–144

Moore JFA, Longworth T (1979) Hydraulic uplift at the base of a deep excavation in Oxford Clay. Géotechnique 29(1):35–46

Moormann C (2004) Analysis of wall and ground movements due to deep excavations in soft soil based in a new worldwide database. Soils Found 44(1):87–98

Onishi K, Sugawara T (1999) Behavior of an earth retaining wall during deep excavation in Shanghai soft ground. Soil Found 39(3):89–97

Peck RB (1969) Deep excavation and tunneling in soft ground. In: Proceeding of the 7th international conference on soil mechanics and foundation engineering, Mexico City, State-of-the-Art Volume, pp. 225–290

Qu JL, Liu GB, Zhang JF (2002) Study on the ground settlement induced by artesian pressure release at Dongchang road metro station. China Civil Eng J 35(5):93–98

Ramaswamy SD (1979) Some aspects of practice and problems of foundations in Singapore. In: Proceeding of 6th Asian regional conference on soil mechanics and foundation engineerings, Singapore

Shao Y, Macari EH, Cai WM (2005) Compound deep soil mixing columns for retaining structures in excavations. J Geotech Geoenviron Eng, ASCE, 132(4):1370–1377

Wang ZW, Ng CWW, Liu GB (2005) Characteristics of wall deflections and ground surface settlements in Shanghai. Can Geotech J 42(5):1243–1254

Chapter 2
Literature Review

2.1 Introduction

For deep excavations in soft clay with an underlying aquifer, there are three major concerns: excavation-induced ground deformation, soil-structure interaction and base instability due to hydraulic uplift. In this chapter, previous studies on these three aspects are reviewed. More importantly, major short-comings of previous works are indentified.

2.2 Ground Deformation Due to Excavation

2.2.1 Field Investigation

(1) Effect of construction of diaphragm wall on ground deformation

One major reason for ground deformations adjacent to an excavation is due to construction of the wall. Poor construction techniques for diaphragm walling were shown to result in large ground movements adjacent to the wall.

Based on several case histories, O'Rourke (1981) reported that total settlements due to construction of diaphragm wall are in the range of 50 to 70 % of the total settlements observed during the entire process of excavation. It was further detailed that during trench excavation, settlements in soft clay and sand occurred due to stress release. During the subsequent placement of concrete, "soil squeeze" (soil moved away from the trench) may occur in soft clay, depending on the amount of time the trench remains open before concreting.

O'Rourke (1981) found that the 18 observed surface settlements due to diaphragm walling were related to the time period when trenches remained unsupported. It is measured that ground surface settlement was approximately 0.2 % of the wall depth. The measured ground surface settlement was smaller that that

Y. Hong and L. Wang, *Deformation and Failure Mechanism of Excavation in Clay Subjected to Hydraulic Uplift*, Advanced Topics in Science and Technology in China, DOI 10.1007/978-3-662-46507-3_2

estimated. This is probably due to the reason that excavated trench was supported laterally by slurry pressure prior to placement of concrete.

(2) Typical deformation profiles due to excavation

Based on field observation from several case histories, Clough and O'Rourke (1990) summerised typical profiles for lateral wall movement and ground surface settlement solely due to excavation. It can be seen that during the first excavation, prior to installation of the first prop, the wall deforms as a cantilever. Correspondingly, settlement trough behind the wall may be represented by a triangular shape. When the excavation reaches deeper elevations, lateral wall movement in the propped region is restrained horizontally. Deformation profile of the wall changes from cantilever to deep-seated type of deflection profile, with the maximum lateral wall displacement located near the formation level of the excavation. In the meantime, settlement trough behind the wall changes from a triangular shape to a trapezoidal shape.

The typical deformation profiles summerised by Clough and O'Rourke (1990) are confirmed by field observations reported by O'Rourke (1981) and Finno et al. (1989).

(3) Empirical method for predicting ground surface settlement

The first rational approach for estimating ground surface settlement adjacent to excavations was proposed by Peck (1969), based on filed data measured adjacent to temporary braced sheet pile and soldier pile walls. Based on soil conditions and workmanship employed when constructing the wall, filed data collected by Peck (1969) are divided into three categories. Category I includes excavations in sand, stiff clay, and soft clay of small thickness. Category II includes excavations in very soft to soft clay extending a small distance below the bottom of the excavation or with a stability number, N_b, less than 6 or 7. Category III includes excavations in very soft to soft clay that extend to a significant depth below the bottom of the excavation, and with stability numbers greater than the critical stability number for basal heave. For Category I soil, the maximum surface settlement is limited to 1 % of the final excavation depth. The maximum surface settlement and influence zone of settlement trough behind the wall increase from excavations in Category I to those in Categories II and III.

Clough and O'Rourke (1990) found that by plotting normalised ground settlement (by the maximum value) against normalised distance behind the wall (by final excavation depth H), a relatively well-defined grouping of settlement data can be obtained. Separate profiles were proposed for sand, stiff to very hard clay, and soft to medium clay, respectively. With given maximum ground surface settlement, the proposed charts can be used to estimate the actual surface settlement. The figure shows that influence zone of settlement trough behind the wall is $3H$ and $2H$ for excavations in stiff to very hard clay and in sands and soft to medium clay, respectively. It can also be seen that settlement trough in soft clay was bounded by a trapezoidal envelope. Inside the envelope, two zones of settlement can be identified. The maximum settlement is located within the zone where $0 \le d/H \le 0.75$

(d denotes distance behind the wall). Within the zone when $0.75 < d/H \leq 2.0$, ground surface settlement decreases from maximum to negligible values. It should be noted that the design diagrams proposed by Clough and O'Rourke (1990) are only valid for estimation of ground settlement due to main excavation. Settlement induced by other construction activities such as diaphragm walling and dewatering is not taken into account.

Based on field observations, Hsieh and Ou (1998) suggested that there are two types of settlement profiles due to excavations: (i) spandrel shape, in which maximum settlement occurs very close to the wall; (ii) concave shape, in which maximum settlement occurs at a certain distance away from the wall. Spandrel shape of settlement profile was found where a large amount of cantilever type of wall deflection occurs at the first stage of excavation while further lateral wall displacement due to subsequent excavation is relatively small. Concave shape of settlement profile was found where after the initial stages of excavation, additional cantilever wall deflection is restrained by installation of support as the excavation proceeds to deeper elevations. The concave shape of settlement profile is corresponding to deep-seated deformation profile of the wall. It is pointed out by Hsieh and Ou (1998) that distance from the wall to the location where the maximum ground surface settlement occurred was approximately equal to half the excavation depth. Assuming the maximum lateral wall deflection occurs near the formation level of the excavation, the maximum ground surface settlement occurs at about half the final excavation depth behind the wall. Based on field data, settlement near the wall was estimated as half the maximum ground surface settlement. The primary influence zone of settlement trough was approximately two times of excavation depths behind the wall. The design diagram also shows that settlement becomes negligible at a distance of four excavation depths behind the wall ($4H$). For simplicity, a linear relationship was assumed between each turning point.

(4) Database based on large number of excavations worldwide

Long (2001) collected measured data from 296 case histories. The database shows that for excavations in stiff clay, the normalised maximum lateral wall displacement ($\delta_{h\text{-max}}/H_e$, H_e denotes final excavation depth) and normalised maximum ground surface settlement ($\delta_{v\text{-max}}/H_e$) are in the range of 0.05 0.25 % and 0 0.2 %, respectively. For excavations in soft clay, $\delta_{h\text{-max}}/H_e$ may be up to 3.2 %. Moreover, dependency of $\delta_{h\text{-max}}$ on system stiffness proposed by Clough et al. (1989) and flexibility number are examined. It is concluded that the deformations of deep excavations in non-cohesive soil as well as in stiff clay are independent of the stiffness of the retaining system (i.e., stiffness of wall and props, as well as prop spacing). For excavations in soft clay, lateral wall displacements of deep excavations appear to have some correlation to stiffness terms proposed by Clough et al. (1989), but with relatively large scatters. The stiffness of retaining system only significantly affects deformations of excavation in soft clays with a low factor of safety against base heave.

Moormann (2004) studied lateral wall displacement and ground surface settlement of 530 case histories in soft soil ($c_u < 75$ kPa). The database shows that $\delta_{h\text{-max}}/H_e$ lies in a range between 0.5 and 1.0 %, with an average value of about 0.87. The locations of $\delta_{h\text{-max}}$ occur at $0.5H_e$ to $1.0H_e$ below the ground surface. $\delta_{v\text{-max}}/H_e$ ranges from 0.1 to 10 %, with an average value of about 1.1 %. The maximum ground surface settlements are located within $0.5H_e$ behind the wall, with some exceptional cases in soft clay (i.e., up to $2.0H_e$). The $\delta_{v\text{-max}}/H_e$ ratios roughly range from 0.5 to 1.0. Similar to conclusion made by Long (2001), it is found that deformations of excavation in soft clay seems to be largely independent of the system stiffness of the retaining system. Instead, deformations are mostly related to ground conditions.

Wang et al. (2010) summerised an extensive database of deformations of 300 deep excavations in Shanghai soft soils. According to construction methods and types of retaining systems, the 300 case histories are divided into five categories, namely top-down method, bottom-up method, sheet pile walls, compound soil nail walls, and deep soil mixing walls. Average $\delta_{h\text{-max}}/H_e$ of these five categories is 0.27, 0.40, 1.5, 0.55 and 0.91 %, respectively. Average $\delta_{h\text{-max}}/H_e$ of the 300 case histories is about 0.42 %. Influence zone of settlement trough behind the wall varies between $1.5H_e$ to $3.5H_e$. The $\delta_{v\text{-max}}/\delta_{h\text{-max}}$ ratios are in the range from 0.4 to 2.0, with a mean of 0.9. Dependency of measured deformations on system stiffness (Clough et al. 1989) and factor of safety against basal heave are examined. It appears that the maximum lateral wall displacement is slightly relevant to the two factors.

2.2.2 *Numerical Analysis*

(1) Influence of system stiffness and ground conditions

Mana and Clough (1981) carried out numerical parametric study to investigate effects of wall stiffness, prop spacing, prop stiffness, prestress and elastic soil stiffness on ground deformations due to excavation. It was revealed that ground deformations decreases with increased wall bending stiffness or decreased prop spacing. This effect is more significant when factor of safety against basal heave is relatively low. Ground deformations decrease with increased prop stiffness, with a decreasing rate at high stiffness. Moreover, ground deformations are also significantly affected by soil modulus. Higher modulus leads to smaller movement.

Based on results from numerical parametric study (by finite element analysis), Clough et al. (1989) developed a design chart. The chart correlates lateral wall displacement of excavation in soft to medium clay to system stiffness and factor of safety against basal heave. The factor of safety against basal heave used in the figure is derived by Terzaghi (1943).

For wide excavations ($B/H_e > 1$), factor of safety against basal heave is given as:

$$FS = c_{ub}N_c/(H(\gamma - c_{uu}/(0.7B))) \tag{2.1}$$

For wide excavations where there is a strong stratum near the base of the excavation, the factor of safety is given as:

$$FS = c_{ub}N_c/(H(\gamma - c_{uu}/D)) \tag{2.2}$$

where c_{ub} and c_{uu} are undrained shear strength below and above formation level of excavation, respectively; H_e denotes final excavation depth; B is width of excavation; γ is bulk density of clay; D is distance from the bottom of the excavation to a relatively hard stratum; N_c represents stability factor, which is equal to:

$$N_c = \gamma H_e/c_u \tag{2.3}$$

It should be noted that this design chart does not take effect of diaphragm walling into account. The chart illustrates that for a given system stiffness, a lower factor of safety against basal heave results in a larger lateral wall displacement after excavation. For excavations in soft clays, where the factor of safety against basal heave is low, a larger stiffness of the support system results in a smaller lateral wall displacement.

Clough and O’Rourke (1990) conducted a series of finite element parametric studies on excavations in stiff clay. The computed results show that parameters such as wall stiffness and prop spacing have only a small influence on deformations around excavations in stiff clay. This is because the model soils are stiff enough to minimise the need for stiff retaining systems. It was found that soil modulus and coefficient of lateral earth pressure have a more significant impact on the ground movements, compared to stiffness of retaining systems. Clough and O’Rourke (1990) also pointed out that base instability is usually not concern for excavations in stiff clays.

Addenbrooke (2000) proposed a new term, displacement flexibility, $\Delta = h^5/(EI)$, to quantify overall stiffness of a retaining system. Dependency of lateral wall displacement on the displacement flexibility was confirmed by computed results from a series of elastic-perfectly plastic finite element analyses. Correlation of the displacement flexibility to lateral wall displacement was checked by extensive case histories worldwide (Long 2001; Moormann 2004). Both suggest that measured maximum lateral wall displacement appears to be independent of the displacement flexibility.

(2) Influence of excavation geometry

Mana and Clough (1981) conducted a two-dimensional numerical parametric study to investigate effects of excavation geometry such as excavation width and depth of the underlying firm layer on ground deformations due to excavation. It was revealed that ground deformations increase with excavation width and depth to an underlying firm layer.

Hashash and Whittle (1996) carried out a series of two-dimensional numerical parametric studies to study effects of wall embedment depth and prop spacing on ground deformations due to multi-propped excavations. Constitutive model (MIT-E3) adopted in the numerical analyses is capable of considering anisotropic stress-strain relationship, stress path dependency and strain dependency of clay. Computed results show that wall length has a minimal effect on the pre-failure deformation for excavations in deep layers of clay, but does have a major effect on the location of failure within the soil. Use of very depth wall can improve base stability. However, large bending moment can be resulted and may cause flexure failure of the retaining wall. Not only is basal affected by final excavation depth, but also influenced by vertical prop spacing. Larger vertical prop spacing can result in additional basal heave.

Jen (1998) carried out numerical parametric studies to study effects of excavation geometry, retaining system and stress history of clay on ground deformations due to excavation. The computed results reveal that distribution of ground deformation is significantly affected by depth of hard stratum below soft clay. While magnitude of ground deformation is governed by excavation width, excavation depth and stress history of clay. Based on the computed settlement troughs behind the wall, new design charts are proposed to correlate ground settlement to excavation depth, wall length, depth of hard stratum and soil profile.

2.2.3 *Analytical Solution*

Osman and Bolton (2006) proposed an analytical solution for estimating ground deformation around excavation in ‘undrained’ clay. The basic idea of this solution follows early study on using ‘mobilised strength’ to predict ground strain and hence displacement (Bolton and Powrie, 1988). A simplified deformation mechanism of excavation was assumed in the mobilised strength design (MSD) method. Ground deformations are linked to stress via stress-strain data from soil tests on undisturbed samples taken from representative elements. This approach has the advantage that one can use a single stress-strain curve from a single soil test, together with a simple hand calculation, to estimate both stability and soil deformation. However, the solution ignored structural energy stored in the retaining system. Ground deformation due to dissipation of excess pore water pressure during and after excavation is not taken into account. Moreover, the solution considers the total energy terms starting from the beginning of excavation. Therefore, the progressive accumulation of mobilised shear strain at different excavation depths is not considered.

Lam (2010) made further improvement of the MSD method developed by Osman and Bolton (2004), using observed ground deformation mechanisms from a series of centrifuge tests of multi-propped excavations in soft clay. In the improved MSD method, structural energy stored in the retaining system is considered. Progressive accumulation of mobilised shear strain at different excavation depths is also taken into account. Ground deformations calculated by the improved MSD method are compared with those computed by an advanced MIT-E3 model. In general, the predictions fell within 30 % of the finite element computed results.

2.2.4 Centrifuge Modelling

Powrie and Daily (2002) reported eight centrifuge model tests on berm-supported embedded retaining walls in over-consolidated clay. Variables between centrifuge tests are depth of wall embedment, berm volume and groundwater level. The test results reveal that for a wall deep enough not to collapse, increasing the size of the berm will result in a more significant reduction in wall and soil movements than increasing the depth of embedment of a wall supported by a smaller berm. An increase in the depth of embedment of a wall of given stiffness supported by a berm of a given size will lead to an increase in wall bending moments, but only a small reduction in wall and soil movements, especially in the short term. Increasing the depth of embedment of a wall supported by a berm of a given geometry is of more benefit if prolonged support is required or perhaps where the time taken to excavate is long. However, even in the long term, the percentage decrease in movements is likely to be rather less than the percentage increase in wall bending moments. The initial groundwater regime, which influences the undrained shear strength and stiffness of the soil, and the timescale for excavation in relation to the timescale for excess pore water pressure dissipation, both have a significant effect on the performance of the wall during and shortly after excavation. Also, the influence of a berm in limiting movements and possibly preventing collapse becomes more significant as drainage occurs within the soil and long-term pore water pressure equilibrium is approached.

Lam (2010) reports five centrifuge tests simulating multi-propped excavation in soft clay. The major objective of the tests is to study ground deformation mechanism due to excavation in clay with varied system stiffness and depth of hard stratum below the soft clay layer. It is observed that incremental wall deformation profiles generally followed O'Rourke's (1993) cosine bulge equation. New deformation mechanisms were postulated with respect to the wall toe fixity condition and excavation geometry. Settlement profiles in a shallow clay bed show a tapering-off trend as the extent of the deformation mechanism is limited by the shallow depth of soft layer.

2.3 Soil-Structure Interaction of Multi-propped Excavation

2.3.1 Field Investigation

(1) Excavation in stiff clay

Tedd et al. (1984) reported a multi-propped excavation in stiff clay at Bell Common. A typical panel was heavily instrumented, for measurements of lateral earth pressure, pore water pressure, lateral wall movement, ground surface settlement and roof loading have been during the construction of retaining wall (secant pile wall) and the subsequent main excavation. It is found that the ground movements occurred during the construction of the secant pile wall itself were surprisingly large and formed a significant proportion of the total movements that were monitored during the entire excavation period. Both construction of wall and the subsequent main excavation caused lateral wall movement into the excavation. Based on measured pore water pressure and lateral total earth pressure adjacent to the excavation, effective stress paths were deduced. During the main excavation, earth pressure behind the wall within propped region moved towards and approached Rankine's active failure boundary. In front of the wall and near the formation level, soil approached passive state at the end of excavation. The wall is very stiff and its movement by the end of construction was mainly a rotation about its toe. Bending moments in the wall were small.

Ng (1998) reported field measurement of a 10 m deep excavation in over-consolidated stiff-fissured gault clay in Lion Yard, Cambridge. The field monitoring programme includes lateral total earth pressure and pore water pressure on both sides of the wall, prop load, lateral wall displacement, ground settlement behind the wall and basal heave inside excavation. The field measurement reveals that due to construction of diaphragm wall, a significant reduction of lateral total earth pressure at the soil-wall interface is resulted. The piling operation inside the site caused a negligible reduction of lateral total earth pressure. Due to low lateral stress in the ground before the main excavation, relatively low prop load and lateral wall displacement are resulted during excavation. The reduction of lateral earth pressure due to excavation was substantially less than that induced by diaphragm walling.

Based on measured total earth pressure and pore water pressure at soil-wall interface, Ng (1999) interpreted effective stress path (in h-h' space) of the case history documented previously (Ng 1998). It was found that immediately after the installation of the instrumented panel, there were substantial reductions in horizontal effective stress at the soil-wall interface at all seven measurement points. During the main excavation, vertical effective stress behind the wall increased significantly with little change of horizontal effective stress. This is as a result of reducing pore pressures accompanied by a small increase in horizontal effective stress. The states of stress behind the wall at the soil-wall interface reached, or were close to, the assumed active condition. In front of the wall, all three stress paths show an increase in horizontal effective stress with a decrease in vertical effective stress during main excavation. At the end of excavation, soil element located near the formation level appears to have reached passive failure. In contrast, two lower soil elements show a continuation of the same stress paths but do not appear to have reached passive failure.

Richards et al. (2007) presents measured changes of pore water pressure and lateral earth pressure on both sides of the wall during an excavation in stiff clay. The measured results show that during excavation, pore water pressure and lateral earth pressure in the soil on both sides of the wall reduced significantly. As expected, the reductions in lateral earth pressure and pore pressure decreased with increasing distance from the wall. In front of the wall, the reduction in lateral stress due to the removal of overburden was a more dominant effect than the increase in lateral stress due to inward movement of wall.

(2) Excavation in soft clay

Ou et al. (1998) presented field performance of an excavation constructed by top-down method in Taipei soft clay. The field measurement include lateral total earth pressure and pore water pressure on both sides of the wall, prop load, lateral wall displacement, ground settlement behind the wall and basal heave inside excavation. Measured results show that prop load corresponds to Peck's apparent earth pressure diaphragm. The lateral ground movement located at 2 m away from the wall was close to that of the wall. The maximum lateral wall displacement is about 0.51 to 0.57 % of final excavation depth (H_e), located near the formation level of the excavation. Lateral earth pressure behind the wall within propped region decreased first and then increased to at-rest earth pressure, due to 'soil arching'. Below propped region behind the wall, lateral earth pressure decreased to less than Rankine's active earth pressure after excavation. The authors explained this as a result of ignorance of soil-wall friction in Rankine's theory. Major influence zone of settlement trough behind the wall is about $2.5H_e$, with the maximum ground settlement located at $0.63H_e$ to $0.78H_e$ behind the wall.

2.3.2 Numerical Analysis

Potts and Fourie (1984) reported finite element analyses (FEA) simulating single propped excavations. An elasto-plastic model with Mohr-Coulomb failure criteria was adopted in the FEA. Objective of the study is to investigate the effects of construction methods (i.e., excavation and backfilling) and of in situ at rest lateral earth pressure coefficient K_o on soil-structure interaction. It is found that for backfilled walls, K_o of soil has only a small influence on wall deformation. On the contrary, K_o has a significant effect on wall deformation for excavated walls. For backfilled walls and excavated walls in a low K_o soil, the simple design calculations underestimate values of prop forces and bending moments. For excavated walls in high K_o soils, prop forces and bending moments greatly exceed those calculated using the simple limit equilibrium approach currently in use. Moreover, relatively large soil movements are induced. The behaviour of excavated walls in a high K_o soil is dominated by the excavation-induced vertical unloading. By installing more props, horizontal movements of the wall and soil can be reduced. But this has a much smaller effect on basal heave. Increasing the embedment of excavated walls in high K_o soils does not reduce the prop force or bending moments, even though the factor of safety is increased. For excavated walls in high K_o soils, soil in front of the wall reached passive state at small excavation depths. The lateral earth pressures behind the wall differ substantially from the classic active distribution. However, for backfilled walls and excavated walls in low K_o soils, lateral earth pressures shows agreement with the classical distributions. Soil behind the wall reached active failure at small excavation depths, prior to passive failure of soil in front of the wall.

Hashash and Whittle (2002) studied effective stress paths around a multi-propped excavation, by adopt MIT-E3 soil model in a finite element program. The adopted MIT-E3 model can capture strain dependency, stress path dependency and strength anisotropy of soil. It is found that soil in front of the wall (1E) follows typical path of plane strain passive mode of shearing. For soil element behind the wall within propped region, the stress paths move towards active failure line first and then experiences a stress reversal, shifting to passive failure line (soil aching). The arching mechanism behind the wall is further interpreted. It is revealed that the major principal stresses are directed toward the lowest level of strut, while an underlying compressive arch transfers loads onto the embedded section of the wall. After installation of the lowest strut, a deeper arching mechanism forms due to the next stage of excavation. The lowest props therefore carry the majority of the supportive earth pressure removal in the subsequent stages of excavation.

2.3.3 Centrifuge Modelling

Richards and Powrie (1998) reported a series of centrifuge tests of twin-propped excavations in stiff clay. The tests aim at studying effects of the groundwater regime, initial lateral earth pressure coefficient, embedment depth of wall and propping sequence on soil-structure interaction associated with multi-propped excavations. Locations of two levels of prop are at the crest of the wall and at the formation level of the excavation, respectively. The physical investigation reveals that an increase in embedment depth of wall can lead to an increase in wall bending moment and a reduction in bottom prop load. Increase of embedment depth of wall without also increasing the wall stiffness can not effectively limit excavation induced ground deformation. The maximum bending moments and prop loads generally increase with the pre-excavation lateral earth pressure coefficient above the excavated surface. By lowering the groundwater behind the retaining wall, bending moments of the wall and prop loads reduce significantly. The bending moments and top prop loads may be greater in the short term, soon after excavation, than in the long term after dissipation of excess pore water pressure.

Lam (2010) reported a series of centrifuge tests simulating multi-propped excavation in lightly over-consolidated clay. Variables between tests are stiffness of wall and props, and distance of excavation to hard stratum. Based on the centrifuge tests, it is found that the empirical estimation by Peck's envelope underestimates apparent earth pressure for a stiff support system by 30 % in relation to the build-up of a vertical arching mechanism. Reducing the bending stiffness of the wall or the axial stiffness of the props caused a reduction in apparent earth pressures. Only cases of excavation with a flexible support system agree reasonably well with Peck's recommendations. By assuming that the total vertical stress is dominated by the overburden weight of the soil, effective stress paths were deduced for soil elements at different locations. Effective stress paths of soil elements in front of the wall move towards passive failure line, as expected. While effective stress paths of soil behind the wall within propped region move towards active failure line first, then shift to move towards passive failure line due to increased horizontal effective stress by soil arching. The rate of mobilisation of shear strength is insignificant for soil elements around excavations with a rigid supporting system. For excavations with flexible retaining system, the rate of mobilization of a soil element at mid depth of the wall is more significant than for shallower and deeper depths.

2.4 Excavation Base Instability Due to Hydraulic Uplift

2.4.1 Field Investigation

Milligan and Lo (1970) summerises eight case histories in Canada related to base instability caused by hydraulic uplift. Based on the reported field observations, base instability associated with hydraulic uplift is accompanied by excessive basal heave, inward movement of the wall and hence ground surface settlement behind the wall. If the large basal heave is not effectively controlled, cracks can be developed inside excavation and create preferetical flow path. Following the path, water in the aquifer would flood into the excavation. In some cases, artesian pressure in the aquifer is released by dewatering. But the dewatering in turn induced excessive ground settlements. The field observation seems to infer that undrained shear strength of clay along the soil-wall interface may help to resist hydraulic uplift to some extend. If the retaining wall was penetrated through the clay layer, base instability may occur, due to greatly reduced undrained shear strength along the soil-wall interface. From observations on a limited number of case histories summarised in the study, it has been proposed that it is possible to dig a narrow trench or excavation in undisturbed intact clay significantly below a depth limited by the ratio of $t/h = 0.5$ (where t is the distance from the bottom of the excavation to the top of a water bearing stratum and h is the critical head at the top of the water bearing stratum). It is suggested that, with the sides of an excavation adequately supported, sheeting or foundation piles should not be driven below the base of the excavation, unless provision is made to relieve uplift water pressure acting on the impervious layer or the pore pressure set up by pile driving. In spited of the summerised observations, initiation and failure mechanism of each case history still remains unknown.

Haydon and Hobbs (1977) reported uplift of excavation base of a 9 m deep excavation for a large nuclear reactor underlain by alternating beds of Lower Lias limestone and clay shale in UK. In the latter case water was found to flow through open joints in the limestone under hydrostatic pressure relative to a water table near ground level. An attempt made during excavation to prevent hydraulic uplift by drilling relief wells was only partly successful due to the difficulty of intersecting the water-bearing joints.

Moore and Longworth (1979) reported a local hydraulic uplift failure in the base of a 29 m deep, large brick pit excavation in Oxford Clay. The failure was preceded by at least a 150 mm rise of the pit base as water accumulated under pressure beneath impermeable clay surface layers. Hydrogeological studies have indicated that the source of water was a thin underlying bed of limestone. Rupture of the capping clay finally resulted in the rapid release of about 7000 m^3 of water which flooded part of the pit and caused an immediate settlement of up to 100 mm of the pit base.

Clough and Reed (1984) presented a braced excavation in very soft clay in California. Base instability problem due to hydraulic uplift was reported to be involved in the excavation. However, details information was not provided.

Davies (1984) reported one excavation in clayey decomposed granite in Singapore. It was observed that when the excavation reached about 6.5 m below ground surface, the southern half of the excavation base suddenly ‘heaved’, accompanied by a rapid water flow into the excavation. Increase of water content of the clay inside excavation resulted in a reduction of undrained shear strength. Accordingly, construction traffic sunk into the very soft clay. Subsequent investigations showed that there is an aquifer located underneath the excavation. Prior to the excavation, designers were not aware of the presence of the aquifer and hence no base stability calculation against hydraulic uplift was conducted. Ramaswamy (1979) reported a similar case history in Singapore where damage to a raft occurred due to high artesian pressure in permeable laminations within stiff clay.

Qu et al. (2002) presented a case history in Shanghai soft clay, which involves concern on base instability due to hydraulic uplift. To study ground settlement induced by artesian release, pumping tests were carried out. Some empirical relationships were obtained between reduced water table in the aquifer and resulted settlement around the pumping well. However, water tables in each pumping wells were found to interact with each other. Measured settlement at a certain location may be affected by various pumping wells, from which artesian release was conducted at different moments. This makes it rather difficult to interpret the measured results. The established empirical equations were therefore questionable.

Gue and Tan (2004) reported two case histories in soft clay underlying with an aquifer in Malaysia. Before reaching formation level of the excavations, hydraulic failure had already taken place and water flow into the clayey subsoil at the base of the excavation pit was evident. Subsequently, continued pumping was conducted to release artesian pressure. The dewatering caused significant drawdown in the groundwater in the surrounding retained ground. The lowering of the groundwater in the retained ground induced significant settlement (both immediate and consolidation) resulting in large cracks and differential settlement of adjacent buildings. It is found that dewatering may extend the influence zone of ground settlement to about 30 times the final excavation depth.

2.4.2 Recommendations in Design Codes

To design for excavations in clay with an underlying aquifer, calculation checking against base instability due to hydraulic uplift is required. In existing design codes such as codes for designing excavations in Shanghai (SMCC code), UK (BSI code) and Europe (EC code), hydraulic pressure which would initiate base instability is simply estimated as overburden pressure of clay inside excavation. This simplified estimation may be too conservative.

CIRIA Report 515 (Preene et al. 2000) suggests to consider effect of undrained shear strength of clay along soil-wall interface in resisting hydraulic uplift. But no specific guidelines are given. Moreover, mobilisation of undrained shear strength is accompanied by shear strain and hence basal heave. Therefore, the suggestion may not be applicable for cases where basal heave is concerned.

2.5 Techniques for Simulation of Multi-propped Excavation in Centrifuge

To model a multi-propped excavation in a centrifuge, process of excavation and propping ideally has to be carried out in-flight. As far as the author is aware, only three cases of in-flight simulation of multi-propped excavation in centrifuge have been reported in the literatures.

Richards and Powrie (1998) simulated in-flight twin-propped excavations in stiff clay. In the test, effect of stress release due to excavation was simulated by draining away zinc chloride fluid with equivalent density as that of clay to be excavated. Prop was achieved with the aid of hydraulic locking unit. Before propping, the locking devices on each prop were held in the open position, so that the props were free to slide and would not support the wall. While there is a need for prop installation, the locking device on prop was activated in-flight to hold the prop in position.

Mcnamara (2001) developed an experimental setup for in-flight simulation of multi-propped excavation in centrifuge. Same as the setup developed by Richards and Powrie (1998), effect of excavation was modelled by draining away zinc chloride fluid (creating stress release). Model props were connected to hydraulic cylinders. By pressurising hydraulic cylinders, model props can be advanced against the retaining wall to simulate prop installation.

Lam (2010) reported development of a 2D actuator to simulate real in-flight excavation. A scraper was connected to the 2D actuator, which is able to move vertically and horizontally. By operating the 2D actuator, the scraper can remove soil in front of the wall in-flight. Model props were connected to a set of horizontally placed hydraulic actuators. When the in-flight excavation reaches each target level, hydraulic actuators at the corresponding levels were pressurised to simulate in-flight prop installation.

2.6 Summary

A review of the literatures to-date on ground deformation, soil-structure interaction and base instability (due to hydraulic uplift) of deep excavation in soft clay is reported in this chapter. Short-comings from existing literature are discussed and summaries as follows.

(1) Given the vast amount of case histories collected by various researchers, it is still not easy to differentiate and understand ground deformations induced by excavations in densely built urban areas and so-called greenfield sites.
(2) It has been reported from eight multi-propped excavations in Shanghai that excavation-induced ground deformations are relatively small than those in similar case histories in soft clay worldwide. Possible reasons are postulated but not justified.
(3) To date, reliable field measurements of earth pressure on walls in excavations in soft clay are rarely reported.
(4) Previous studies on base instability due to hydraulic uplift are mainly based on coarse field observations, from which ground deformation mechanism within soil body can not be obtained. In addition, without accurate real-time measurement of uplift movement of clay inside excavation and artesian pressure in the aquifer, the initiation of hydraulic uplift in all reported case histories still remains unknown. To date, systematic study on the initiation and failure mechanism of excavation base instability due to hydraulic uplift is not available in the literatures.
(5) In current design codes (BSI, 1985; SMCC, 1997; EC 7, 2004), hydraulic pressure which initiates base instability is simply estimated as overburden pressure of clay inside excavation. This simplified solution may be too conservative.

(6) The most commonly used method to prevent base instability due to hydraulic uplift is releasing artesian pressure inside excavation within cut-off walls. This method is reported to be ineffective under some circumstance (Haydon and Hobbs 1977) and maybe time consuming and costly. Existing alternative methods for base stabilisation are very rare.

References

Addenbrooke TI, Potts DM, Dabee B (2000) Displacement flexibility number for multi-propped retaining wall design. J Geotech Geo-environ eng 126(8):718–726

Bolton MD, Powire W (1988) The behaviour of diaphragm walls in clay prior to collapse. Géotechnique 38(2):167–189

Clough, GW, O'Rourke TD (1990) Construction induced movements of in situ walls. Proc. Design and Performance of Earth Retaining Structure, ASCE Special Conference, Ithaca, New York, pp. 439–470

Clough GW, Reed MW (1984). Measured behaviour of braced wall in very soft clay. J Geotech Eng Div, ASCE, 110(1):1–19

Clough GW, Smith EW, Sweeney BP (1989) Movement control of excavation support system by iterative design. Foundation Engineering Current Principles and Practices, Vol. 2, ASCE, New York, NY, pp. 869–882

Davies (1984) Some geotechnical problems with foundations and basements in Singapore. In: Proceedings of international conference on tall buildings, Singapore, 22–26, October

Finno RJ, Atmatzidis DK, Perkins SB (1989) Observed performance of a deep excavation in clay. J Geotech Eng, ASCE, 115(8):1045–1064

Gue SS, Tan YC (2004) Two case histories of basement excavation with influence on groundwater. Keynote Lecture, In: International Conference on Structural and Foundation Failures (ICSFF), Singapore, 2–4, August

Hashash YMA, Whittle AJ (1996) Ground movement prediction for deep excavations in soft clay. J Geotech Eng, ASCE, 122(6):474–486

Hashash YMA, Whittle AJ (2002) Mechanism of load transfer and arching for braced excavations in clay. J Geotech Geoenviron Eng, ASCE, 128(3): 187–197

Haydon REV, Hobbs NB (1977) The effect of uplift pressures on the performance of a heavy foundation on layered rock. In: Proceedings.of Conference on Rock Engineering. British Geotechnical Society and Department of Mining Engineering, University of Newcastle, pp. 457–472

Hsieh PG, Ou CY (1998) Shape of ground surface settlement profiles caused by excavation. Can Geotech J 35(6):1004–1017

Jen LC (1998) The design and performance of deep excavation in clay. Ph.D thesis, MIT

Lam SY (2010) Ground movements due to excavation in clay: physical and analytical models. Ph.D thesis, University of Cambridge, UK

Long M (2001) Database for retaining wall and ground movements due to deep excavation. J Geotech Geoenviron Eng, ASCE, 127(3):203–224

Mana AI, Clough GW (1981) Prediction of movements for braced cuts in clay. J Geotech Eng, ASCE, 107(6):759–777

Mcnamara MA (2001) Influence of heave reducing piles on ground movements around excavations. Ph.D thesis, City University of London, UK

Milligan V, Lo KY (1970) Observations on some basal failures in sheeted excavations. Can Geotech J 7(2):136–144

Moore JFA, Longworth T (1979) Hydraulic uplift at the base of a deep excavation in Oxford Clay. Géotechnique 29(1):35–46

Moormann C (2004) Analysis of wall and ground movements due to deep excavations in soft soil based in a new worldwide database. Soils Found 44(1):87–98

Ng CWW (1998) Observed performance of multi-propped excavation in stiff clay. J Geotech Geoenviron Eng, ASCE 124(9):889–905

Ng CW (1999) Stress paths in relation to deep excavations. J Geotech Geoenviron Eng, ASCE, 124(5):357–363

O'Rourke TD (1981) Ground movements caused by braced excavations. J Geotech Geoenviron. Eng, ASCE, 107(9):1159–1178

O'Rourke TD (1993) Base stability and ground movement prediction for excavations in soft clay. Retaining Structures, Thomas Telford, London, pp 131–139

Osman AS, Bolton MD (2004) A new design method for retaining walls in clay. Can Geotech J 41 (3):453–469

Osman AS, Bolton MD (2006) Ground movement predictions for braced excavations in undrained clay. J Geotech Geoenviron Eng, ASCE, 132(4): 465–477

Ou CY, Liao JT, Lin HD (1998) Performance of diaphragm wall construction using top-down method. J Geotech Geoenviron Eng ASCE, 124(9): 798–808

Peck RB (1969) Deep excavation and tunneling in soft ground. In: Proceeding of the 7th international conference on soil mechanics and foundation engineering, Mexico City, State-of-the-Art Volume, pp 225–290

Potts DM, Fourie AB (1984) The behaviour of a propped retaining wall-the results of a numerical experiment. Géotechnique 34(3):383–404

Powire W, Daily MP (2002) Centrifuge model tests of embedded retaining walls supported by earth berms. Géotechnique 52(2):89–106

Preene M, Roberts TOL, Powrie W, Dyer MR (2000) Groundwater Control: Design and Practice. Publication, CIRIA C515

Qu JL, Liu GB, Zhang JF (2002) Study on the ground settlement induced by artesian pressure release at Dongchang road metro station. China Civil Engineering Journal 35(5):93–98

Ramaswamy SD (1979) Some aspects of practice and problems of foundations in Singapore. In: Proceeding of 6th Asian regional conference on soil mechanics and foundation engineering, Singapore

Richard DJ, Powrie W (1998) Centrifuge tests on doubly propped embedded retaining walls in over-consolidated kaolin clay. Géotechnique 48(6):833–846

Richards DJ, Powrie W, Roscoe H, Clark J (2007) Pore water pressure and horizontal stress changes measured during construction of a contiguous bored pile multi-propped retaining wall in Lower Cretaceous clays. Géotechnique 57(2):197–205

Tedd P, Chard BM, Charles JA, Symons IF (1984) Behaviour of a propped embedded retaining wall in stiff clay at Bell Common Tunnel. Géotechnique 34(4):513–532

Terzaghi K (1943) Theoretical soil mechanics. John Wiley, New York

Wang J, Xu Z, Wang W (2010) Wall and Ground Movements due to Deep Excavations in Shanghai Soft Soils. J Geotech Geoenviron Eng, ASCE, 136(7):985–994

Chapter 3
Field Investigation of a Multi-propped Excavation in Soft Clay

3.1 Introduction

In recent decades, significant economic development in big cities such as Shanghai is driving the expansion of traffic demand, especially underground transportation. A large number of deep excavations have been carried out for underground metro stations. One major concern relating to excavations in urban areas is the possibility of excessive ground deformations induced by excavation. Based on the field monitoring of six multi-propped excavations in Shanghai, the characteristics of wall deflections and ground surface settlements in Shanghai soft clays have been summarised by Wang et al. (2005). It is worth noting that these six excavations were carried out in the densely built city centre of Shanghai for the Pearl II circle line. The measured ratios of maximum ground surface settlement ($\delta_{v\text{-max}}$) to maximum lateral wall displacement ($\delta_{h\text{-max}}$) ranged from 0.2 to 0.6, which are slightly smaller than the range of 0.5–1.0 reported by Ou et al. (1993) and Moorman (2004) from their worldwide case histories of excavations in soft clays. Given the vast amount of case histories collected by various researchers, it is still not easy to differentiate between ground deformations induced by excavations in well-built urban areas and so-called greenfield sites from the database. It is therefore of interest and worthwhile to investigate and compare ground deformations induced in a greenfield site and a conjested site influenced by underground structures and foundations nearby.

One essential issue for the design of a retaining wall for multi-propped excavations is the determination of the stress and deformation of the retaining wall and the axial load of props. The beam on elastic foundation analysis method is still commonly adopted in many parts of the world including Shanghai (Onishi and Sugawara 1999; Hu et al. 2003; Shao et al. 2005). It is widely recognized that this analysis is not able to account for stress redistribution in adjacent soil due to wall flexibility, and the accuracy of this analysis heavily relies on assumed earth pressures acting on the wall. To date, reliable field measurements of earth pressure on walls in excavations in Shanghai are rarely reported. Since the actual earth

Y. Hong and L. Wang, *Deformation and Failure Mechanism of Excavation in Clay Subjected to Hydraulic Uplift*, Advanced Topics in Science and Technology in China, DOI 10.1007/978-3-662-46507-3_3

pressures acting on a retaining wall are governed by many factors such as ground conditions, construction method and sequence, stiffness of the retaining system, field measurement of earth pressures will be helpful to determine the earth pressures appropriate for practical designs. Besides, to assist with the design of prop loads, it will be useful to establish an apparent earth pressure envelope for excavations, based on extensive field measurements.

In an attempt to address the aforementioned issues regarding excavations in Shanghai, a multi-propped excavation in a greenfield site in Shanghai clay was closely monitored at a typical diaphragm wall panel that was heavily instrumented. The monitoring programme include measurement of lateral wall displacements, lateral ground displacements, surface ground settlements, earth pressures, pore water pressures and prop loads. The soil-structure interaction associated with the instrumented panel is studied and its implications for practical design are investigated. Raw data were obtained from the projected and interpreted solely by the author.

The reported field data in this chapter are also used to calibrate a constitutive model, its model parameters and modelling procedures in a finite element program in Chap. 4.

3.2 The Site

Figure 3.1 shows the plan view of this site. The excavation for the Gu Bei Station is 149.5 m by 17.5 m on plan, and is located at the South-East corner of the New Hong Qiao Central Park (approximately 576 m by 466 m). Prior to the development of the park in the early 1990s, the area was farmland. This site may, therefore, be considered as a greenfield sit.

3.2.1 Geotechnical Profile

Shanghai is located on the southern bank of the Yangtze River along the coast of the East China Sea. Alluvial sediments in Shanghai were deposited during the Quaternary period, due to changes of climate and sea levels. These strata are present to a depth up to 400 m (Lee et al. 1999). As a result of marine deposition, Shanghai clay contains mica, oyster shells and organic matter (Wang et al. 2005). The depth of engineering significance for this 14.5 m deep excavation is about 50 m below the ground surface. Figure 3.2 shows the soil profile and geotechnical parameters obtained from a 50 m deep borehole (BH, see Fig. 3.1) near the location of the instrumented diaphragm wall panel (P4) investigated and discussed in this study.

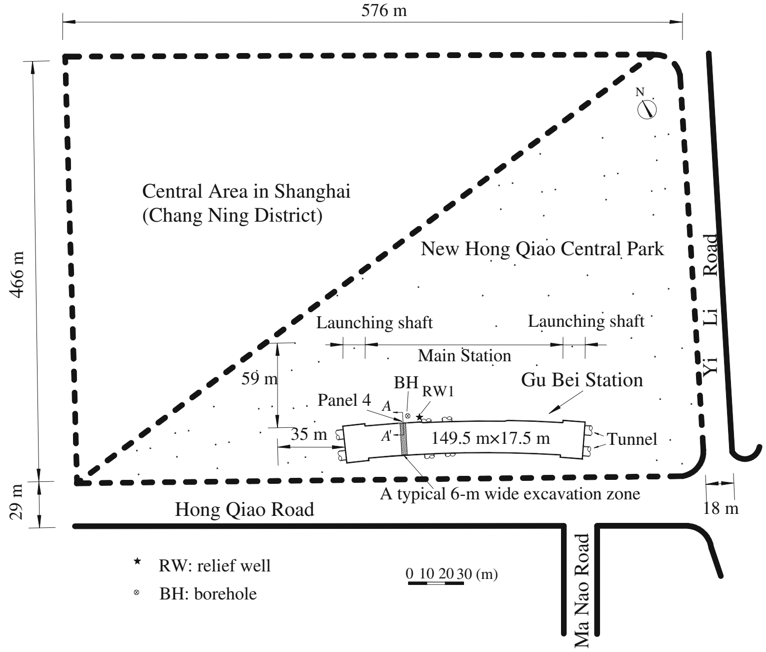

Note: this figure is not drawn to scale

Fig. 3.1 Plan view of the site

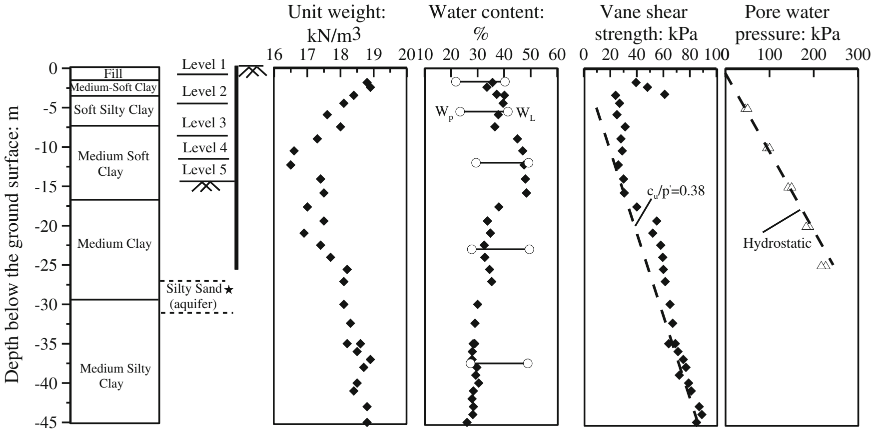

★ The 'silty sand' layer was not found in this current BH.

Fig. 3.2 Soil profile near Panel 4 and geotechnical parameters

At Panel 4, there are 6 strata within the depth of 50 m below the ground surface. In this study, the ground level is taken as the reference datum. The uppermost clay layer (medium-soft clay) is slightly over-consolidated due to desiccation (Liu et al. 2005) while the underlying clay layers are generally normally consolidated (Lee et al. 1999). Both in situ and laboratory tests were carried out to obtain geotechnical parameters of the soil near Panel 4. The undrained shear strength and pore water pressure shown in Fig. 3.2 were obtained by in situ measurements using vane shear tests and standpipe piezometer, respectively. It can be seen from the figure that the measured bulk density of soil generally decreases with depth within the top 16 m. In the same depth range, the measured water contents increase with depth and are close to the liquid limit (W_L) of each soil stratum within the same depth. Below this depth, the measured water contents are close to the plastic limit (W_P) of each clay layer. Except for the top desiccated medium-soft clay layer, the measured vane shear strength stays fairly constant within the top 16 m, below which the shear strength increases with depth. As shown in the figure, the lower bound value of c_u/p' may be 0.38. Similar relatively high value of c_u/p' (i.e., 0.4) for field vane tests was also reported from another excavation site in Shanghai (Liu et al. 2005). It is generally recognised that c_u measured by in situ vane shear tests are likely to be larger than those by laboratory tests such as direct simple shear tests (Ghionna et al. 1983). In addition, the presence of organic matter could result in a relatively high c_u of Shanghai clay.

Relatively undisturbed samples obtained by thin-wall tube sampler from BH (see Fig. 3.1), were taken for laboratory testing. The effective angle of shearing resistance (ϕ') and the effective cohesion (c') of each layer were determined by consolidated drained triaxial tests. Prior to shearing, each soil specimen was consolidated isotropically to a cell pressure equal to the corresponding in situ effective mean normal stress. The constrained modulus (M) was determined by odometer tests, at vertical stress ranging from 100 to 200 kPa. The saturated vertical permeability (k_v) and horizontal permeability (k_h) were determined by laboratory constant head tests. Table 3.1 summarises average geotechnical parameters for each layer measured by in situ tests (i.e., W, γ, I_p and c_u) and laboratory tests (i.e., ϕ', c', M, K_v and K_h). In the table, the relatively high c' values may be due to the presence of organic matter, which provide greater bonding at the contact points between mineral particles (Beekman 1987).

The ground water table was located at about 0.6 m below the ground surface. According to other geological explorations at the site, there is an aquifer located at about 27 m below the ground surface, with a sub-artesian head at approximately 5 m below ground surface. According to Qu et al. (2002), the thickness of this aquifer is about 4 m. It can be seen from Fig. 3.2 that the measured in situ pore pressures below 20 m are slightly less than the hydrostatic pressures, probably due to under-drainage resulting from the presence of the aquifer.

Table 3.1 Geotechnical parameters

Stratum	W (%)	γ (kN/m^3)	I_p (%)	ϕ' (°)	c' (kPa)	M (MPa)	k_v (m/s)	k_h (m/s)	c_u^a (kPa)
Medium-soft clay	36	18.8	18	29	6	4.0	4.3×10^{-9}	1.16×10^{-8}	48
Soft silty clay	40	17.2	14	27	3	3.2	7.7×10^{-9}	4.4×10^{-8}	24
Medium soft clay	49	17.6	21	26	6	2.3	4.3×10^{-9}	6.0×10^{-8}	28
Medium clay	34	18.2	15	31	7	3.1	4.2×10^{-9}	1.1×10^{-8}	50
Medium silty clay	25	18.4	12	30	11	5.3	2.4×10^{-9}	4.2×10^{-8}	80

[a] c_u were measured by in situ vane shear tests

3.2.2 Construction Sequence

Figure 3.3 shows the cross section (section *A-A′*, Fig. 3.1) and geometry of the excavation at Panel 4. A top–down construction sequence was adopted in this excavation. The 26 m deep and 0.6 m thick cast-in-place diaphragm wall was supported by 4 prop levels. The first prop was cast using in situ reinforced concrete while the remainder were pre-stressed steel props. The dimensions of pre-stress applied (if any) to each prop are summarised in Table 3.2. It should be noted that the aim of pre-stressing is to minimize further lateral wall movement at the prop level after prop installation. The pre-stress applied was intended to balance 70 % of the vertical total earth pressure behind the wall.

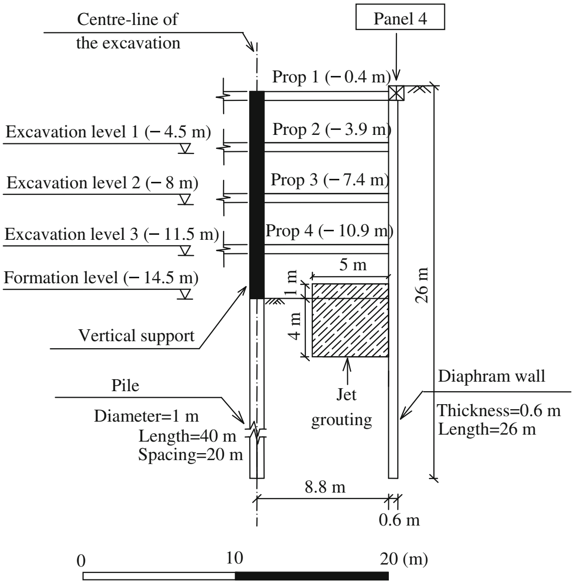

Fig. 3.3 Cross section and geometry of excavation at Panel 4 (section *A-A′*, Fig. 3.1)

Table 3.2 Dimension, spacing and applied pre-stress of each prop

Prop level	Cross section	Horizontal prop spacing (m)	Applied pre-stress (kN)
Prop 1	Rectangular: 0. 6 m (width) × 0.8 m (height)	6	Nil
Prop 2	Circular: 609 mm external diameter with a 16 mm thickness	3	600
Prop 3		3	720
Prop 4		3	700
Grouted prop	Rectangular: 3 m (width) × 5 m (height)	3	Nil

Note The vertical spacing for each prop (except the grouted prop) is 3.5 m

Table 3.3 Stages of construction at Panel 4

Stage		Day No.	Construction activity
Pre-excavation	I(a)	1–2	Construct Panel 4
	I(b)	75	Construct grouted props (–13.5–19.5 m)
	I(c)	96	Cast Prop 1 (–0.4 m)
Main excavation	II(a)	126–128	Excavate to Level 2 (–4.5 m)
	II(b)	129	Install Prop 2 (–4 m)
	III(a)	130–136	Excavate to Level 3 (–8 m)
	III(b)	137	Install Prop 3 (–7.5 m)
	IV(a)	138–149	Excavate to Level 4 (–11.5 m)
		147	Start artesian release in RW1 (Fig. 3.1)
	IV(b)	150	Install Prop 4 (–11 m)
	V	151–163	Excavate to Level 5 (–14.5 m)[a]
		163	Cease artesian release in RW1
	VI	164–168	Cast basement slab after removal of top 1 m of the grouted prop
After excavation	VII(a)	187	Remove Prop 3 and Prop 4
	VII(b)	204	Construct middle slab (−7.5 m)
	VII(c)	216	Remove Prop 2
	VII(d)	233	Construct top slab at ground surface (0 m)

[a] At Stage V, top 1 m of the grouted prop was removed (see Fig. 3.4a)

Following diaphragm walling (Stage I(a) as listed in Table 3.3) and prior to the main excavation, the ground inside the site was improved by jet grouting to form a 5 m thick 'grouted props' (see Fig. 3.4a), spanning across full-width of the excavation.

During main excavation, the site was divided into 25 excavation zones (or segments) along the longitudinal direction of the station. Each excavation segment was approximately 6 m wide, which is equal to the width of each diaphragm wall panel. Within each segment, excavation was carried out from the centre line of the site towards the two diaphragm wall panels perpendicularly. The main excavation at

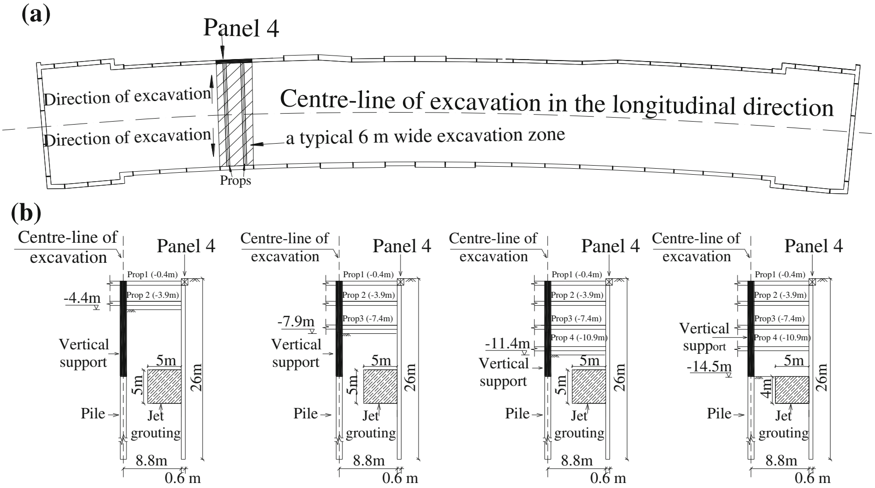

Excavate to -4.5m [stage II(a)] and install pre-stressed prop 2 at -4m [stage II(b)]
(Day 126-129)

Excavate to -7.4m [stage III(a)] and install pre-stressed prop 3 at -8m [stage III(b)]
(Day 130-137)

Excavate to -11.5m [stage IV(a)] and install pre-stressed prop 4 at -10.9m [stage IV(b)]
(Day 138-150)

Excavate to -14.5m (stage V)
(Day 151-163)

Note: The dimesion of prop and pre-stressed load applied to each prop are summerised in Table 3.

Fig. 3.4 **a** Plan view of excavation zone and props at Panel 4; **b** Cross section view showing cycles of excavation and propping at Panel 4 (section *A-A*′, Fig. 3.1)

Panel 4 consisted of alternative cycles of excavation and propping as illustrated in Fig. 3.4b and summarised in Table 3.3. On completion of the excavation (after Stage V), top 1 m of the grouted prop was removed for the construction of the basement concrete slab at the final formation level (Stage VI). It was observed that the grouting and the clay were generally uniformly mixed although some air voids can be seen in the mixture. Grouted props were generally in contact with diaphragm wall. After construction of basement slab, props 3–4 were removed (Stage VII(a)) and a middle slab was cast at the same elevation as Prop 3 (Stage II(b)). Other detailed construction stages are summarised in Table 3.3.

Inside the excavation, any free water on the exposed ground surface (mainly due to rainfall) was removed by vacuum pumps during each excavation stage. To limit ground settlements around the excavation, no dewatering was carried out outside the site, with an exception of emergency pumping to release artesian pressure from Day 147 to Day 163 (i.e., between Stage IV(a) and Stage V). It is a common practice to reduce artesian pressure in the underlying aquifer when an unacceptable basal heave (i.e., larger than 2 mm per day) is measured during excavation in Shanghai. Dewatering was conducted by pumping water out through a submerged pump located in a deep relief well, RW1 (see Fig. 3.1), which was installed about 8 m away from Panel 4, about 30 m depth below the ground surface into the underlying aquifer. This deep well consists of granular filter backfill within and surrounded by a slotted well screen.

3.3 Instrumentation

To verify design assumptions and to improve understanding of ground response induced by the deep excavation, various instruments were installed on site. In this study, only the instrumentation in and near Panel 4 is reported. As shown in Fig. 3.5, seven vibrating wire earth pressure cells (EP) were installed at each side of Panel 4 to measure the lateral total earth pressures at the soil-wall interface. Each earth pressure cell was accompanied by one pneumatic piezometer (PP), which was located at the same elevation as the EPs, to measure corresponding pore pressures. Each EP and PP was connected to an air cylinder, which was fixed to the reinforcement cage before lowering it into a slurry trench. Initial readings of EPs and PPs were monitored when the instruments were lowered into the slurry trench. The initial reading of each EP and PP was calibrated against hydrostatic bentonite slurry pressure (unit weight of bentonite slurry γ_b = 12 kN/m^3) and hydrostatic water pressure at each elevation, respectively. It is worth noting that γ_b normally ranges from 11.5 to 12 kN/m^3 in Shanghai.

After setting initial readings, EPs and PPs were jacked out against the excavated ground surface by air cylinders.

The axial load of each prop was measured by a load cell (LC) installed at each wall-prop connection. To minimise temperature effects, prop loads were measured daily in the evening.

To measure wall deflection, an inclinometer tube (I4-1) was fixed to the reinforcement cage for Panel 4 before concreting. To obtain lateral movement of the top

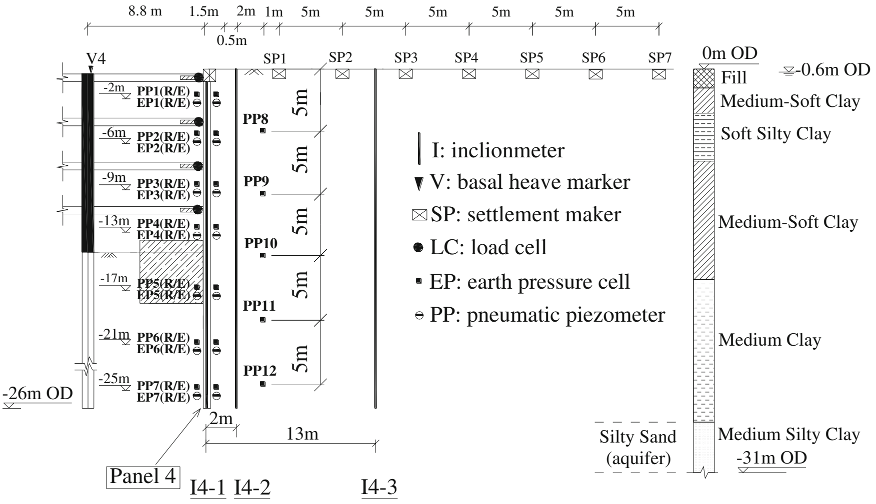

Note: For earth pressure cells (EPs) and pneumatic piezometers (PPs), "R"denotes on the retained side and "E" denotes on the excavated side.

Fig. 3.5 Layout of the instrumentation at Panel 4 (section *A-A′*, Fig. 3.1) of Panel 4 from measured rotations by I4-1, one control target marker was installed at the top of I4-1. Any movement of the control marker was recorded by a theodolite with reference to a surface station located about 100 m (seven times of the final excavation depth (H_e) behind the panel. Based on the measured wall rotations and the lateral movements of the marker, the absolute displacement of Panel 4 could be determined. Two other inclinometers I4-2 and I4-3 were installed to measure the lateral ground movements 2 and 13 m behind Panel 4, respectively. Since the control target markers installed at the top of I4-2 and I4-3 were damaged prior to excavation, zero displacement was assumed when converting the measured rotations to lateral displacements at I4-2 and I4-3.

Seven settlement markers (SP1–SP7) were installed at 5 m intervals behind Panel 4. Each settlement marker penetrated through any overlying pavements to 0.5 m below the ground surface. The vertical movements of settlement markers were measured by levelling with reference to a benchmark socket located 100 m ($7H_e$) behind the wall, approximately.

To monitor the effects of basal heave in the centre of the excavation, one marker (V4) was installed on top of the central column opposite Panel 4. The vertical movement of V4 was measured in the same way as that of settlement markers. It should be noted that the central column was socketed 2 m into a cast-in-place pile. Due to the presence of the relatively long pile (i.e., 40 m), measured heave of column should have included the constraints imposed by the pile.

During the construction of Panel 4, the EPs and PPs located at the soil-wall interface were installed during concreting. All other instruments were installed after the construction of Panel 4 but prior to the main excavation. The accuracy for each instrument is summerised in Table 3.4.

Apart from Panel 4, ground surface settlement and lateral wall displacement at Panels 5, 6 and 7 (i.e., P5, P6 and P7 as shown in Fig. 3.1) were also measured, by adopting the same instruments and measuring methods as those for Panel 4.

Table 3.4 Resolution and estimated accuracy for each instrument in this site

Instrument	Resolution	Estimated accuracy
Vibrating wire earth pressure cell (EP)	0.32 kPa	1 kPa
Pneumatic piezometer (PP)	0.32 kPa	1 kPa
Load cell	1.6 kN	3 kN
Levelling	±0.5 mm/km	±0.5 mm/km
Inclinometer	0.1 mm/500 mm gauge length	0.1 mm/500 mm gauge length

3.4 Ground Deformation and Soil-Structure Interaction at Panel 4

This section focuses on ground deformation and soil-structure interaction at Panel 4 during and after the main excavation (from Day 126 to Day 233). As settlement markers (SP1 to SP7) and inclinometers in the ground (I4-2 and I4-3) were installed after the installation of the diaphragm wall, ground deformations recorded were solely induced by the main excavation. For each construction stage, the results presented in this chapter are referred to the end of each stage, except Stage I(c), which refers to the beginning of the excavation.

3.4.1 *Lateral Wall Displacement of Panel 4*

Figure 3.6 illustrates the measured lateral wall displacements at Panel 4 (I4-1). The measured lateral ground movements behind Panel 4 (I4-2, I4-3) are also included for comparisons.

At the first stage of main excavation (Stage II(a)), cantilever type of wall displacement was prevented at Panel 4 due to the casting of the first prop prior to the main excavation. As the excavation proceeded, the lateral wall displacement (I4-1) increased with the maximum lateral wall movement ($\delta_{h\text{-max}}$) of a deep-seated profile moving downward. At each excavation stage, the location of $\delta_{h\text{-max}}$ occurred approximately at the excavation level. When excavation reached the formation level (Stage V), the measured maximum lateral wall movement was 37 mm, which is equal to 0.25 % of the excavation depth (H_e). By considering the resolution of the inclinometer adopted in this study (i.e., 0.1 mm/500 mm gauge length, see Table 3.4), the $\delta_{h\text{-max}}$ (measured at 15 m from the wall top) may be 37 ± 3 mm, which is equivalent to $(0.25 \pm 0.02)\%H_e$. This range is comparable to the

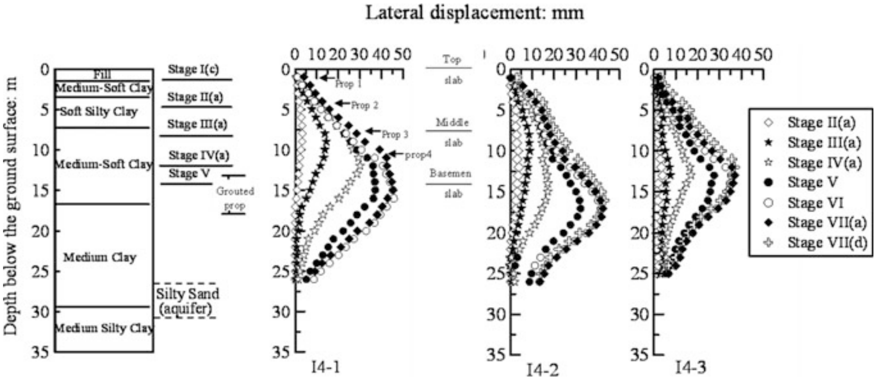

Fig. 3.6 Lateral wall displacements at Panel 4 and lateral ground movements behind Panel 4

measurements from six similar excavations in Shanghai (Wang et al. 2005), in which the measured values of $\delta_{h\text{-max}}$ range from 0.13 $\%H_e$ to 0.43 $\%H_e$. During the 5-day casting of the basement slab (Stage VI), a further 8-mm increment (22 %) in $\delta_{h\text{-max}}$ was recorded. This increase in $\delta_{h\text{-max}}$ was likely caused by the removal of a 1-m thick grouted prop in front of the wall at the end of Stage V (Table 3.3).

In the subsequent Stage VII(a), the slight change in $\delta_{h\text{-max}}$ cannot be differentiated based on the resolution of I4-1.

3.4.2 Lateral Ground Movement Behind Panel 4

As expected, the lateral ground deflection (I4-2 and I4-3) decreased with an increase in the distance from the diaphragm wall. The deformation profiles of the wall (I4-1) and the ground (I4-2 and I4-3) were similar. When the excavation reached the formation level (Stage V), the maximum lateral ground deflection measured at 2 m ($\delta_{h\text{-max(2 m)}}$) and 13 m ($\delta_{h\text{-max(13 m)}}$) behind the wall was 32 and 27 mm, which were corresponding to $0.87\delta_{h\text{-max}}$ and $0.73\delta_{h\text{-max}}$, respectively. During the casting of the basement slab (Stage VI), 25 and 26 % increases in the maximum lateral ground deflections at 2 and 13 m behind the wall were recorded, respectively.

In the subsequent stages (Stages VII(a) and VII(d)), further change in $\delta_{h\text{-max}}$ was not differentiable based on resolution of I4-2 and I4-3.

3.4.3 Ground Surface Settlement Behind Panel 4

Figure 3.7 illustrates measured ground surface settlement at SP1–SP7 (refer to Fig. 3.5) during different excavation stages. To verify the common undrained assumption for the Shanghai clay during excavation, the measured lateral wall displacements (I4-1) are also included for comparisons. Corresponding to the deep-seated deflections of Panel 4, concave settlement profiles were observed behind Panel 4, as expected.

At the first three excavation stages (Stages II(a) to IV(a)), the ratios of the maximum surface ground settlement ($\delta_{v\text{-max}}$) to the corresponding maximum lateral wall movement ($\delta_{h\text{-max}}$) at Panel 4 range from 0.7 to 0.8. At Stage V, the ratio of ($\delta_{v\text{-max}}/\delta_{h\text{-max}}$) increased substantially to 1.3. This substantial increase was possibly caused by the release of artesian pressures in the relief well (RW1 as shown in Fig. 3.1) behind diaphragm wall during Stage V (details to be discussed later).

As shown in Fig. 3.7, the area bounded by the ground settlement profile and the abscissa may be regarded as the incremental volume loss of the retained ground, while the area bounded by the lateral wall displacement profile and the abscissa represents the volume gain of the retained ground. It can be seen from the figure that the incremental volume loss of the retained ground was slightly larger than the

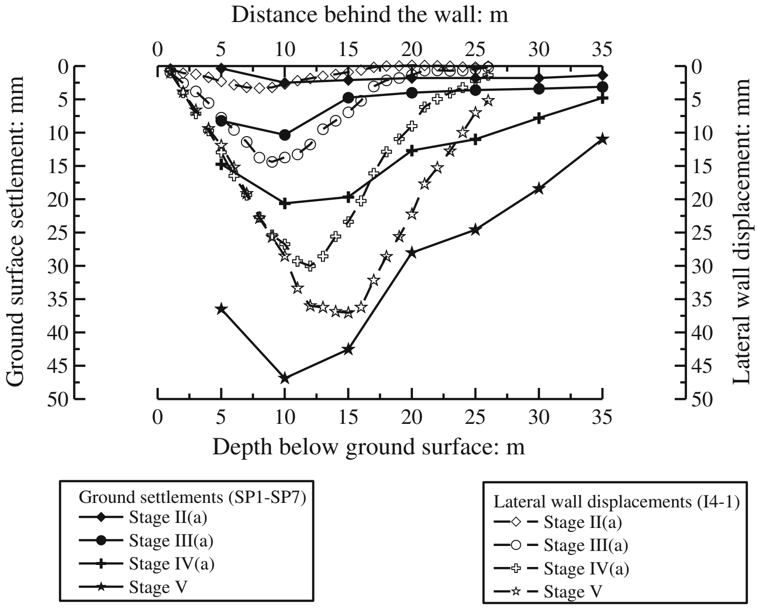

Fig. 3.7 Relationship of ground surface settlement and lateral wall displacement during excavation

incremental volume gain induced by the lateral wall displacement and their difference increased with excavation stages. This suggests that consolidation occurred in the soil behind the wall during excavation. Thus, the typical assumption of constant volume deformation in soft clays was not applicable for this site. Consolidation settlement behind the wall was also observed from excavations in soft clay in Taipei (Ou et al. 2000) and Singapore (Shirlaw and Stewart 1991), respectively.

3.4.4 Ground Surface Settlement and $\delta_{v\text{-}Max}/\delta_{h\text{-}Max}$ Ratios in Shanghai

Figure 3.8 compares normalised ground surface settlements (by H_e) in this unique greenfield site and those in eight other similar multi-propped excavations (with similar ground conditions, retaining systems and construction methods) but constructed in densely built areas in Shanghai (Wang et al. 2005; Tan and Wei 2011; Liu et al. 2011). Since ground surface settlement behind Panel 4 in this study might be influenced by artesian pressure release, ground settlements behind three other panels (see P5, P6 and P7 in Fig. 3.1) far away from the relief well are also included

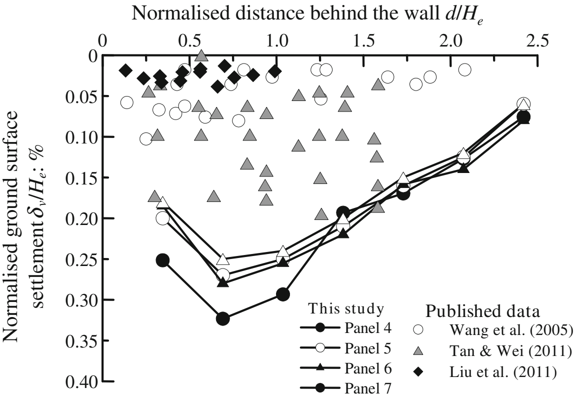

Fig. 3.8 Normalised surface ground settlement

from comparisons. The distances from P5, P6 and P7 to RW1 are about 35, 65 and 85 m, respectively.

It can be seen that at this greenfield site, $\delta_{v\text{-max}}$ values range from approximately 0.25 $\%H_e$ to 0.32 $\%H_e$ and the influence zone of ground surface settlement was larger than $2.5H_e$ behind the wall. Measured $\delta_{v\text{-max}}$ at Panel 4 is the largest among the four settlement troughs (i.e., about 17 % larger than the average $\delta_{v\text{-max}}$ value at Panels 5–7), maybe due to additional settlement induced by artesian pressure release. Compared to ground settlements at this greenfield site, measurements from seven other similar excavations reported by Wang et al. (2005) and Liu et al. (2011) show much smaller $\delta_{v\text{-max}}$ values of 0.1 $\%H_e$ and 0.04 $\%H_e$ and less extensive influence zones ($2.0H_e$ and $1.0H_e$, respectively). Smaller $\delta_{v\text{-max}}$ values (less than 0.2 $\%H_e$) were also reported by Tan and Wei (2011), while the influence zone of ground settlement could not be identified due to the relatively scattered data. It is worth pointing out that the construction duration of main excavation at this greenfield site was 37 days while those of eight other case histories sites ranged from 43 to 165 days. Consolidation settlement was very likely to occur in all these case histories but with different extents. Due to the shorter duration of excavation at this greenfield site than those at the eight other sites, consolidation settlement at this site should be anticipated to be the smallest if the ground conditions were identical at all sites. Therefore, the observed larger magnitude and wider ground settlement troughs at this site might be due to the lack of stiffening effects provided by adjacent underground structures, foundations and services.

Measured $\delta_{v\text{-max}}/\delta_{h\text{-max}}$ ratios at Panels 5–7 at this site range from 1.0 to 1.1, which is about 23 % smaller than that at Panel 4 (i.e., $\delta_{v\text{-max}}/\delta_{h\text{-max}} = 1.3$). The relatively larger $\delta_{v\text{-max}}/\delta_{h\text{-max}}$ measured at Panel 4 might be attributed to artesian pressure release. The measured $\delta_{v\text{-max}}/\delta_{h\text{-max}}$ ratios in excavations reported by Wang et al. (2005), Tan and Wei (2011) and Liu et al. (2011) are in the range of 0.2–0.6, 0.4–1.2 and 0.4–0.5, respectively. By comparing $\delta_{v\text{-max}}/\delta_{h\text{-max}}$ ratios measured from the reported excavations in densely built areas and those from this greenfield site (i.e., P5, P6 and P7), it seems that there is no discernable dependency of greenfield effects on $\delta_{v\text{-max}}/\delta_{h\text{-max}}$ ratios for excavations in Shanghai.

3.4.5 Change of Lateral Total Earth Pressure

Figure 3.9a illustrates measured change of lateral total earth pressures on the retained side during and after excavation. With the commencement of excavation (Stage I(c)), total horizontal stresses (σ_h) recorded by EP1(R) to EP4(R) on the retained side generally reduced at each stage of stress release due to excavation. However, EP1(R) to EP3(R) registered an increase in σ_h when the excavation level proceeded below their corresponding elevations suggesting soil arching took place during the excavation stages. At the end of the main excavation (Stage VI), measured σ_h at EP1(R) was higher than its initial pressure at Stage I(c) whereas the measured σ_h at EP2(R) and EP3(R) returned to their initial pressures. The pre-stress applied to props may increase σ_h behind the wall upon prop installation. But it is unlikely that this effect could have led to a continuous increase in σ_h during the entire excavation process. As shown in Fig. 3.6, the soil above each excavation level behind the wall was relatively well retained by props while the soil below the excavation level moved inwards as excavation proceeded. The relative movement between the well retained soil mass and the inward moved soil mass led to soil arching or upward vertical stress transfer from the soil below the excavation level to that above through shear stress, resulting in an increase in σ_h above each excavation level. After Stage VI, there was no significant change of lateral earth pressures recorded at EP1(R) to EP4(R).

For EPs located on the retained side below the formation level (EP5(R) to EP7 (R)), an abrupt reduction in σ_h was recorded after each stage of excavation (Stage I (c) to Stage V) due to lateral stress release by excavation. Between Stages IV(a) and V, however, EP5(R) to EP7(R) recorded a gradual increase in σ_h, due to the dissipation of negative excess pore water pressures. After Stage VI, EP5(R) to EP7 (R) also registered a small gradual increase in σ_h. As there was no noticeable inward wall movement recorded by I4-1 (see Fig. 3.6), the increase in σ_h might be caused by a further increase in positive pore water pressure resulting from dissipation of excess pore water pressures (details to be discussed later).

Figure 3.9b illustrates changes of lateral total earth pressures on the excavated side during and after excavation. During excavation stages (Stage I(c) to Stage IV (a)), σ_h on the excavated side kept decreasing at all EPs, as expected. Between Stages IV(a) and V, however, there was a slight increase in σ_h at EP6(E) and EP7 (E). These increases in total earth pressure may be due to the relative large inward movements of the wall near and at the toe. As revealed in Fig. 3.6, the increases in lateral wall displacement recorded by I4-1 at depths of 21 and 25 m, corresponding to elevations of EP6(E) and EP7(E), were 190 and 220 % at Stage V relative to that at Stage IV(a).

During the period 70 days after main excavation (Stage VI to Stage VII(d)), EPs on the excavated side recorded a general increase in σ_h, due to recovery of pore water pressure (to be discussed later).

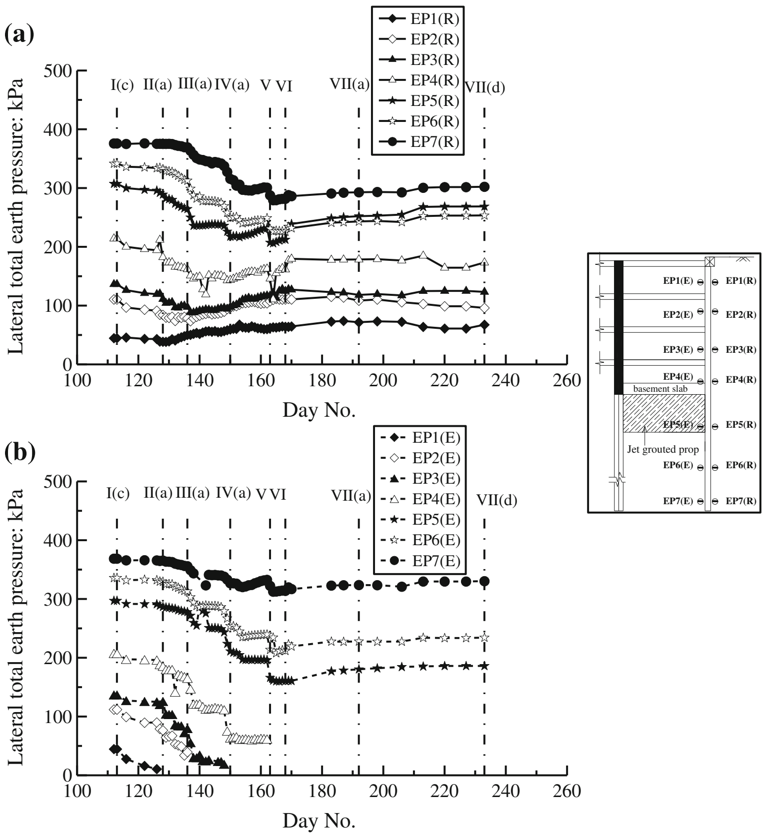

Fig. 3.9 Change of lateral total earth pressure on **a** retained side and **b** excavated side

3.4.6 Distrubtion of Lateral Total Earth Pressure

Figure 3.10 illustrates distribution of measured lateral total earth pressures on both sides of wall at some selected stages. The at-rest earth pressure distribution (Jáky 1944), a theoretical bilinear concrete pressure envelope (Appendix 1 in Lings et al. 1994) and the design earth pressure distribution adopted in Shanghai are also included for reference. For retaining wall design in Shanghai, earth pressure behind the wall is empirically estimated as 0.7 times of total vertical earth pressure. Two pressure limits (K_a and K_p lines) are calculated by adding the limiting horizontal effective stress based on Rankine's theory and pore water pressures measured at Stage V (at the end of the excavation) together. In calculating K_a and K_p pressures, ϕ' value for each soil layer is taken from Table 3.1. Soil wall friction angle (δ') is assumed to be zero in the calculation of K_a and K_p.

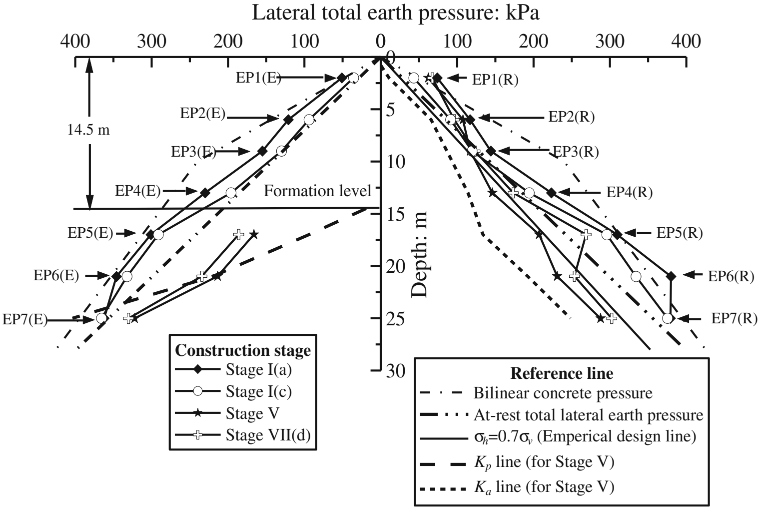

Fig. 3.10 Distribution of lateral total earth pressure on both sides of Panel 4

As shown in Fig. 3.10, the lateral total earth pressures, except EP1(R), EP6(R) and EP1(E), on both sides of the panel generally fell between the at-rest earth pressure and the theoretical concrete pressure envelope immediately after concreting at Panel 4 (Stage I(a)). As the at-rest lateral earth pressure in soft clay is smaller than the lateral concrete pressure, the concreting process resulted in an increase in the lateral earth pressure adjacent to the panel. This is in contrast to the observed significant reduction in lateral stress after the construction of diaphragm wall in overconsolidated clays (Tedd et al. 1984).

The subsequent excavation stages (Stage I(c) to Stage V) resulted in a decrease in the lateral total earth pressures on both sides of the wall, except three earth pressures on the retained side (EP1(R), EP2(R) and EP3(R)) within the propped region. Earth pressures at EP1(R) and EP2(R) at Stage V were even larger than that before excavation (Stage I(c)). While earth pressure at EP3(R) experienced a zero net change during the main excavation. As discussed in the previous section, the lateral earth pressure within propped region was increased by the upward shear stress transfer (soil arching) during excavation.

On completion of main excavation, the distribution of earth pressure on the retained side stayed above the K_a line. On the excavated side, the earth pressure near the formation level (EP5(E)) seems to approach the passive failure while earth pressures at deep depth EP6(E) and EP7(E) stayed below the K_p line. This observation is consistent with the implication given by numerical analysis on a multi-propped excavation in stiff clay (Ng 1999). The computed result shows that the maximum shear strain around the excavation occurred just below the final excavation level on the excavated side, where the soil was yielding. Therefore, earth pressure at EP5(E) was most likely to reach passive state sooner than others on the excavated side. Due to the presence of the ‘grouted prop’ (with a compression resistance of 1.28 MPa) at the formation level, the shear strength of the adjacent soil could have been largely increased.

Figure 3.10 shows that at Panel 4, the earth pressure behind the wall adopted in Shanghai retaining wall design ($\sigma_h = 0.7\sigma_v$) forms a lower boundary of the measured earth pressures at all construction stages. The $\sigma_h = 0.7\sigma_v$ adopted in design actually is simply a sum of the active effective horizontal stress ($K_a = 0.33$) and the hydrostatic pore pressure. The effects of diaphragm walling, soil arching behind the wall and the application of pre-stressed prop on the earth pressure behind the wall are not taken into account. Therefore, the earth pressure adopted in design may underestimate the actual value.

3.4.7 Prop Load and Equilibrium Analysis of Wall

With the measured prop loads, it is of interest to validate the reliability of measured lateral earth pressures by carrying out an equilibrium analysis of Panel 4. A 3 m wide (equal to the horizontal prop spacing) of the panel with a depth of 26 m is taken for the equilibrium analysis of four major excavation stages (i.e., Stage II(a) to Stage V). Figure 3.11 illustrates the equilibrium analysis of the wall at the final stage of excavation (Stage V). Similar equilibrium analyses were carried out for the other three stages of excavation. For equilibrium calculations, measured lateral earth pressures on both sides of the 3 m wide panel were converted to equivalent horizontal forces. Linear interpolation was assumed between two adjacent measured earth pressures during the conversion. The results of equilibrium analysis for each

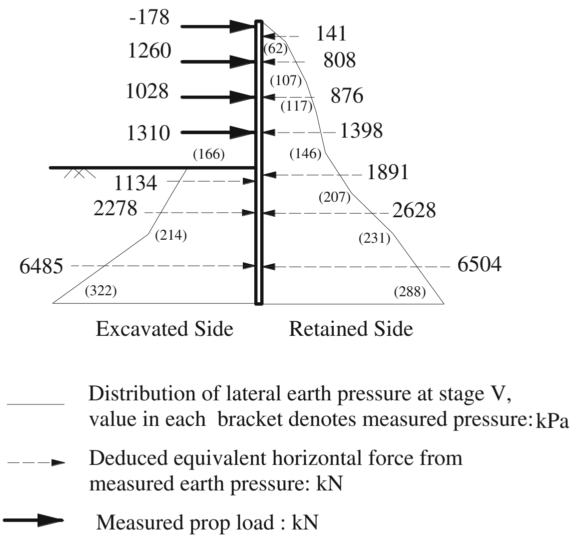

Fig. 3.11 Equilibrium analysis of Panel 4 (Stage V)

Table 3.5 Equilibrium analysis of panel 4 at four major excavation stages

Stage	$\sum F_R/\Sigma F_E$	$\Sigma M_R/\Sigma M_E$
Stage II(a)	1.06	1.12
Stage III(a)	1.05	1.09
Stage IV(a)	0.96	1.07
Stage V	1.08	1.07

excavation stage are summarised in Table 3.5. The $\Sigma F_R/\Sigma F_E$ denotes the ratio of total equivalent horizontal force on the retained side (ΣF_R) to the summation of measured prop forces and total equivalent horizontal force on the excavated side (ΣF_E). It can be seen that the $\Sigma F_R/\Sigma F_E$ ratios vary from 0.96 to 1.08 at the four major stages of excavation. The difference in the total horizontal forces acting on the both sides of the wall is not greater than 8 %. This implies that the measured earth pressures on both sides of the wall are reasonably reliable.

By taking the moment about the top of the wall, the total disturbing moment, ΣM_R, which is caused by each F_R, and the total restoring moment, ΣM_E, which is contributed by each F_E, $\Sigma M_R/\Sigma M_E$ ratios are calculated. As summarised in Table 3.5, the $\Sigma M_R/\Sigma M_E$ ratios vary from 1.07 to 1.12 at the four major stages of excavation. The maximum difference between the total disturbing and total resisting moments is not larger than 12 %. Based on both the force and moment equilibrium analyses, it is evident that the measured earth pressures and prop forces are reasonably consistent and reliable.

It should be noted that compressive forces were recorded at Prop 1 until the final stage of excavation (i.e., Stage V). Tensile force was measured at Prop 1 after the final excavation (Fig. 3.11). The measured tensile force may be induced by the uplift movement of the inner column supporting the prop (Fig. 3.11), resulting from the basal heave due to vertical stress release. It can be seen from Fig. 3.11 that Prop 1 was supported by the diaphragm wall on one end and the inner column on the other end. When the excavation reached the formation level, the uplift movement recorded by V4 at top of the vertical column was 54.9 mm. Due to the differential movement between the column and the diaphragm wall, it can be demonstrated that the measured tensile force is reasonable.

3.4.8 Apparent Pressure Envelope for Excavations in Shanghai

To date, the apparent envelopes proposed by Peck (1969) based on monitoring of excavations supported by sheet pile or soldier pile and lagging walls are still commonly used in engineering design. Prop forces acting on a retaining wall are governed by many factors such as ground conditions, construction sequences and stiffness of the retaining system, thus apparent pressure envelopes deduced from measured prop forces are likely to be site specific.

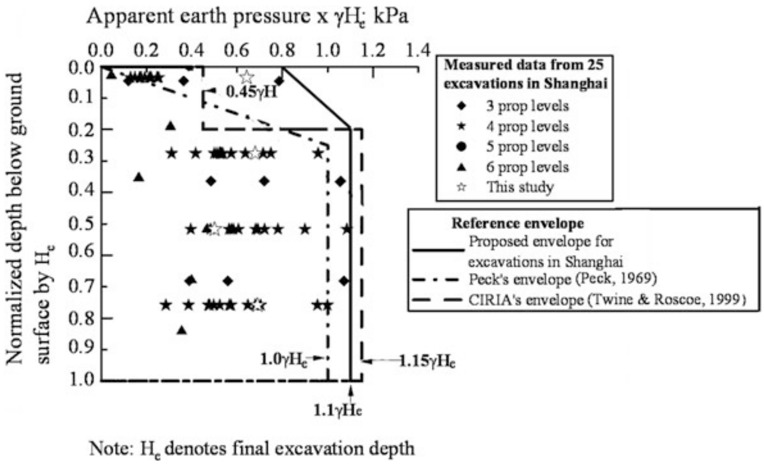

Fig. 3.12 Apparent earth pressure envelop for excavations in Shanghai

Figure 3.12 shows the proposed apparent earth pressure envelope for excavations in Shanghai, in which γ denotes the average total unit weight of soil (γ = 18 kN/m^3) and H_e denotes the final excavation depth. The apparent earth pressure envelope is deduced from maximum measured prop loads from 24 excavations in Shanghai summarised by Shi (2007) and the measurements obtained from this study. The pressure envelope proposed by Peck (1969) with K_a = 1.0 and the CIRIA design envelope (Twine and Roscoe 1999) for excavations supported by stiff walls in soft clay are included for comparisons.

It is worth mentioning that all 25 selected case histories in Shanghai shown in Fig. 3.12 were excavations for long rectangular shape metro stations. The retaining wall for each case history was supported by props installed inside an excavation. Therefore, each retaining wall could be considered to deform under the plane strain conditions. These excavations were supported by different levels of props, varying from 3 to 6 levels. All these excavations were carried out using the top–down construction method and the construction sequences for each site are fairly similar. All props were pre-stressed except the first level of props at these sites (Shi 2007). It can be seen that the measured data show relatively large scatter among different sites. The apparent earth pressures seem to be independent of the levels of props. Approximately 75 % of the measure data are less than the initially applied pre-stress (i.e., below 0.7γH_e). At this site, all maximum apparent earth pressures are approximate equal to γH_e expect one equal to about 0.5γH_e. The measured data from this greenfield site are larger than 70 % of those from other 24 excavations in Shanghai. The maximum apparent earth pressure for the selected excavations in Shanghai is 1.1γH_e. This is larger than the maximum magnitude allowed by Peck's pressure envelope (1.0γH_e). Besides, the apparent earth pressures exceed the trapezoidal boundary of the Peck's pressure envelope for the upper 5 %H_e depth. This may be attributed to the use of the top–down construction method in which high elevation of the first prop level (usually located at –0.5 m) is often installed to minimize ground deformations in urban cities like Shanghai. It is apparent that CIRIA pressure envelope may account for some of effects due to the top–down construction method.

As shown in Fig. 3.12, the apparent earth pressures at the upper 5 % of H_e in Shanghai are well bounded by the CIRIA's envelope, except two cases. Compared with Peck's envelope, the CIRIA pressure envelope (maximized at $1.15\gamma H_e$) is closer to the proposed pressure envelope in Shanghai.

3.4.9 Pore Water Pressure

Figure 3.13 illustrates distribution of pore water pressure measured at soil-wall interface on both sides of the diaphragm wall (PP1(E)–PP7(E), PP1(R)–PP7(R)). No data from PP3(R) is included since it ceased function prior to excavation.

Immediately before excavation (Stage I(c)), the measured pore water pressures on both sides of the wall fall on the hydrostatic line closely. This implies any excess pore pressures induced during diaphragm walling were fully dissipated at the soil-wall interface before excavation. During the subsequent excavation stages (Stage II(a) to Stage V), measured pore pressures on both sides of the wall generally deceased due to the vertical and lateral stress releases and dewatering on the excavated side, except PP1(R) and PP2(R). Between Stages IV(a) and V, measured pore water pressures at PP1(R) and PP2(R) increased slightly. These slight increases might be due to vertical stress transfer from the lower to the upper regions (i.e., soil arching). To reduce basal heave, 'emergency' pumping was carried out in

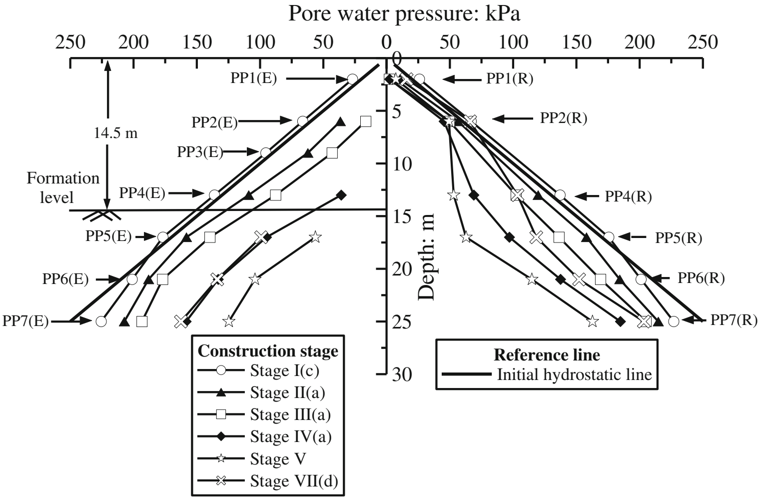

Fig. 3.13 Distribution of pore water pressures on both sides of Panel 4

the aquifer between Days 147 and 163 (i.e., Stages IV(a) and V). Noticeable reductions of pore water pressures at the soil-wall interface were recorded at the lowest three PPs behind the wall (PP5(R) to PP7(R)). The pore water pressure distributions at these three locations were decreased consistently and parallel to the hydrostatic line, suggesting an approximate 5.6 m drawdown of water table at the soil-wall interface in clay. This measured reduction of pore water pressure in the soft clay might be attributed to stress release due to excavation and partial drainage induced by artesian pressure release in the sub-aquifer. Considering the reduction of pore water pressure measured at the clay-wall interface is anticipated to be larger than that in the soft clay layer, the impact of the 'emergency' pumping on ground settlement at Panel 4 might be limited during excavation (as shown in Fig. 3.8).

At Stage VII(d) (i.e., about 70 days after the final excavation), there was a substantial recovery of pore water pressures on both sides of the wall.

3.4.10 *Effective Stress Path*

Figure 3.14 illustrates some representative effective stress path on both sides of soil wall during various excavation stages. The horizontal effective stress (σ'_h) is deduced from the measured total lateral stress and pore water pressure at the soil-wall interface. Behind the wall, the vertical total stress (σ_v) is assumed to be constant. Hence changes in vertical effective stress essentially represent pore water pressure changes on the retained side of the wall. It should be pointed out that the measured total lateral stresses and pore water pressures are likely to reflect the

Fig. 3.14 Effective stress path

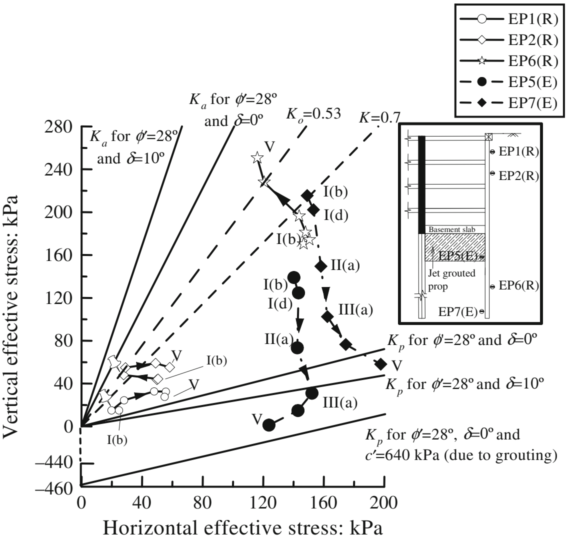

denotes reversal in the direction of stress path localised behaviour at the soil-wall interface only (Ng 1999). For the ease of interpretation of the deduced stress paths, the in situ K_o line estimated using the Jaky's equation (Jáky 1944) and Rankine's passive and active limiting pressures with and without wall friction are included in the figure. The average effective angle of shearing resistance, ϕ' (i.e., 28°), and the average effective cohesion, c' (i.e., 5.5 kPa), are taken from Table 3.1 for calculating the limiting pressures for soil elements at different locations. The soil wall friction angle δ' is taken as one third of ϕ' (10°).

It is worth mentioning that EP5(E) is located inside the 'grouted prop', in which the effective cohesion c' is much larger than that of clay. Based on static cone penetration tests carried out, the unconfined compressive strength of the improved area reached about 1.28 MPa at 28 days after grouting. By using a Mohr-circle, the estimated c' of the 'grouted prop' is 0.64 MPa. Thus, a passive limiting line with the consideration of the stiffened c' value due to grouting is included in Fig. 3.14 for reference. It is obvious that this limiting line is only relevant for the stress path of EP5(E).

At Stage I(b) (74 days after diaphragm walling), the measured lateral earth pressure coefficients were higher than 0.7 (approximate 1.4 times K_o), due to the construction of the diaphragm wall (refer to Fig. 3.10).

During excavation, the effective stress paths for soil on the retained side above the formation level (EP1(R) and EP2(R)) show a decrease in σ_h' first then experience a reversal in the direction of stress path, turning to a continuous increase in both σ'_h and σ'_v. The stress paths at these two EPs generally moved horizontally towards the passive limit, as a result of the increase in total lateral stresses due to soil arching (Fig. 3.9a) and a slight reduction in pore water pressures (Fig. 3.13). This observation is consistent with Lambe and Whitman (1969), in which they stated that soil state near crest of the wall is "more nearly in a passive state of stress than in an active state of stress" due to soil arching. Beneath the formation level, the stress path at EP6(R) shows a decrease in σ'_h (due to lateral stress release) associated with an increase in σ'_v (due to decrease in pore pressure) during excavation. The stress path moved towards the active limiting line but did not reach it at the end of excavation (Stage V).

On the excavated side, σ'_v at EP5(E) and EP7(E) decreased continuously as the excavation proceeded (due to vertical stress release). At Stage III (a), σ'_h at EP5(E) reached the theoretical passive limiting line if the additional grouting strength in the front of the wall were not taken into account. As the excavation continued, the effective stress paths at EP5(E) and EP7(E) moved towards the revised (including grouting effects) and the original passive limiting lines, respectively. However, the stress paths at EP5(E) (near the formation level) and at EP7(E) (near the toe of the wall) showed a decrease but an increase in σ'_h towards the end of excavation, respectively. The measured decrease in σ'_h at EP5(E) was likely attributed to the significant vertical stress release inside the site. To the contrary, the observed increase in σ'_h at EP7(E) might be attributed to the inward toe movement of the wall. Similar stress paths to those at EP5(E) and EP7(E) are also observed in the multi-propped excavation in stiff Gault clay in Cambridge (Ng 1999).

Tedd et al. (1984) and Ng (1999) studied stress paths related to multi-propped excavations in stiff clay. Two major differences can be noted from the comparison between their deduced effective stress paths and that in this study:

(a) The diaphragm walling in soft clay results in an increase in σ'_h at soil wall interface while it leads to substantial reductions in σ'_h in stiff clay, because the lateral fresh concrete pressure (Lings et al. 1994) is found to be larger than the lateral earth pressure in soft clay but is smaller than that in stiff clay.

(b) During excavation, increase in σ'_h behind the wall (soil arching) is less likely to recover for excavations in stiff clay than that in soft clay. Experiments on the relationship between wall displacement and lateral earth pressure indicate that for a given lateral strain (towards active state), stiff clay show almost twice lateral stress release than that in soft clay (NAVFAC DM7.2, 1982). Due to relative large lateral stress release for excavations in stiff clay, σ'_h behind the wall is less likely to be recovered by the soil arching. Data from one recently reported excavation in stiff clay (Richards et al. 2007) has also confirmed this point. On the contrary, it is common to observe an increase in lateral earth pressure behind the wall for excavations in soft (Ou et al. 1998; Tanaka 1994; Liu et al. 2005).

3.5 Summary and Conclusions

Based on the field observations and interpreted results from this greenfield site, the following conclusions can be drawn:

(1) When the excavation reached the formation level, the $\delta_{h\text{-max}}$ at Panel 4 was 0.25 $\%H_e$, which is comparable to those $\delta_{h\text{-max}}$ values ranging from 0.13 $\%H_e$ to 0.43 $\%H_e$ measured from eight other similar excavations in Shanghai.

(2) At this greenfield site, the $\delta_{v\text{-max}}$ at the end of excavation ranges from 0.25 $\%H_e$ to 0.32 $\%H_e$ and the influence zone of ground surface settlement is larger than $2.5H_e$ behind the wall. Both measured $\delta_{v\text{-max}}$ and influence zone of ground settlement at this site are generally larger than those at eight other excavations in densely built areas of Shanghai (Wang et al. 2005; Tan and Wei 2011; Liu et al. 2011).

(3) Measured $\delta_{v\text{-max}}/\delta_{h\text{-max}}$ ratios at Panels 5–7 at this site range from 1.0 to 1.1 while measured $\delta_{v\text{-max}}/\delta_{h\text{-max}}$ ratios in eight other similar excavations in densely built areas are in the range of 0.2–1.2. This seems to suggest that there is no discernable dependency of greenfield effects on $\delta_{v\text{-max}}/\delta_{h\text{-max}}$ ratio.

(4) The force and moment equilibrium analysis of Panel 4 at different excavation stages generally confirms the reliability of the measured earth pressures.

(5) The earth pressure behind the wall adopted in Shanghai retaining wall design ($\sigma_h = 0.7\sigma_v$) forms a lower boundary of the measured earth pressures at all construction stages.

(6) Based on measured earth pressures and pore water pressures at the soil-wall interface, effective stresses were deduced. After diaphragm walling, the lateral earth pressure coefficient (effective stress) at the soil-wall interface was increased by a factor of more than 1.4. During excavation, the stress paths for the retained soil within the propped region generally moved towards the passive state, instead of the active state, during the last few stages of main excavation. On the excavated side, stress paths for soil located near the formation level approached the passive failure state. It is evident that the 'grouted prop' near the formation level prevented the ground in front of the wall from experiencing passive failure.

(7) Based on the maximum prop loads measured at 25 excavations in Shanghai, the maximum apparent earth pressure in Shanghai is found to be $1.1\gamma H_e$. At this greenfield site, the maximum apparent earth pressures are generally larger than the average maximum apparent earth pressures from the other 24 excavations in Shanghai.

References

Beekman F (1987) Soil strength and forest operations. PhD thesis, Agricultural University, Wageningen, The Netherlands

Ghionna V, Jamiolkowski M, Lacasse S, Lancellota R, Lunne T (1983) Evaluation of self-boring pressuremeter. In: Proceedings of the international symposium on soil and rock investigation by in situ testing, Paris, pp 294–301

Hu ZF, Yue ZQ, Zhou J, Tham LG (2003) Design and construction of a deep excavation in soft soil adjacent to the Shanghai Metro tunnels. Can Geotech J 40(5):933–948

Jáky, J (1944) The coefficient of earth pressure at rest. J Soc Hung Arch Eng 78(22):355–358 (in Hungarian)

Lambe TW, Whitman RV (1969) Soil mechanics. Wiley, New York

Lee KM, Ji HW, Shen CK, Liu JH, Bai TH (1999) Ground response to the construction of Shanghai Metro Tunnel line 2. Soils Found 39(3):113–134

Lings ML, Ng CWW, Nash DFT (1994) The lateral pressure of wet concrete in diaphragm wall panels cast under bentonite. Proc Inst. Civ Eng Geotech. Eng 107(3):163–172

Liu GB, Ng CWW, Wang ZW (2005) Observed performance of a deep multi-strutted excavation in Shanghai soft clays. J Geotech Geoenviron Eng, ASCE 131(8):1004–1013

Liu GB, Jiang J, Ng CWW, Hong Y (2011) Deformation characteristics of a 38 m deep excavation in soft clay. Can Geotech J 48(12):1817–1828

Moormann C (2004) Analysis of wall and ground movements due to deep excavations in soft soil based in a new worldwide database. Soils Found 44(1):87–98

Ng CWW (1999) Stress paths in relation to deep excavations. J Geotech Geoenviron Eng, ASCE 124(5):357–363

Onishi K, Sugawara T (1999) Behavior of an earth retaining wall during deep excavation in Shanghai soft ground. Soil and Foundations 39(3):89–97

Ou CY, Hsieh PG, Chiou DC (1993) Characteristics of ground surface settlement during excavation. Can Geotech J 30(5):758–767

Ou CY, Liao JT, Lin HD (1998) Performance of diaphragm wall construction using top–down method. J Geotech Geoenviron Eng, ASCE 124(9):798–808

Ou CY, Liao JT, Cheng WL (2000) Building response and ground movements induced by a deep excavation. Géotechnique 50(3):209–220

Peck RB (1969) Deep excavation and tunneling in soft ground. In: Proceeding of the 7th international conference on soil mechanics and foundation engineering, Mexico City, State-of-the-art volume, pp 225–290

Qu JL, Liu GB, Zhang JF (2002) Study on the ground settlement induced by artesian pressure release at Dongchang road metro station. China Civ Eng J 35(5):93–98

Richards DJ, Powrie W, Roscoe H, Clark J (2007) Pore water pressure and horizontal stress changes measured during construction of a contiguous bored pile multi-propped retaining wall in Lower Cretaceous clays. Géotechnique 57(2):197–205

Shao Y, Macari EH, Cai WM (2005) Compound deep soil mixing columns for retaining structures in excavations. J Geotech Geoenviron Eng, ASCE 132(4):1370–1377

Shi SY (2007) The safety characteristic analysis of supporting system in deep excavation in soft clay area. PhD thesis, Tongji University

Shirlaw JN, Stewart DF (1991) Geotechnical aspects of the construction of the Singapore MRT. In: Symposium of developments in geotechnical aspects of embankments, excavations, and buried structure, Bangkok, pp 507–524

Tan Y, Wei B (2011) Observed behavior of a long and deep excavation constructed by cut-and-cover technique in Shanghai soft clay. J Geotech Geoenviron Eng, ASCE 138(1):69–88

Tanaka H (1994) Behavior of a braced excavation in soft clay and the undrained shear strength for passive earth pressure. Soils Found 34(1):53–64

Tedd P, Chard BM, Charles JA, Symons IF (1984) Behaviour of a propped embedded retaining wall in stiff clay at Bell Common Tunnel. Géotechnique 34(4):513–532

Twine D, Roscoe H (1999) Temporary propping of deep excavations: guidance on design. Construction Industry Research and Information Association, London C517

Wang ZW, Ng CWW, Liu GB (2005) Characteristics of wall deflections andground surface settlements in Shanghai. Can Geotech J 42(5):1243–1254

Chapter 4
Numerical Analyses of the Multi-propped Excavation in Soft Clay

4.1 Background

In the previous chapter, a case history of a multi-propped excavation in a greenfield site in Shanghai soft clay is comprehensively documented. Together with the case history documented in this study and eight others reported in the literature (Liu et al. 2005; Wang et al. 2005; Tan and Wei 2011; Liu et al. 2011), it is found that excavation-induced ground deformation in Shanghai soft clay is relatively smaller than similar excavations in soft clay worldwide (Long 2001; Moormann 2004). Major reasons are considered to be use of jet grouting in front of the wall (i.e., grouted prop) and prestressed props (Liu et al. 2005; Wang et al. 2005; Liu et al. 2011; Ng et al. 2012). These postulations have not been justified, due to difficulties in de-coupling effect of each factor on ground deformations from the field data. Moreover, effect of dissipation of excess pore water pressure on ground deformations should also be considered and quantified.

In this chapter, the case history documented in Chap. 3 was back-analysed by a coupled-consolidation finite element analysis. Numerical parametric studies were also conducted to investigate effect of grouted prop, prestressed prop and dissipation of excess pore water pressure on deformations and soil-structure interaction of multi-propped excavation in soft clay. Descriptions of the excavation simulated, constitutive model and model parameters adopted and analyses undertaken are reported. The computed results are compared with the comprehensive case record of the Shanghai excavation. Major reasons governing excavation-induced ground deformation in Shanghai soft clay are identified.

Y. Hong and L. Wang, *Deformation and Failure Mechanism of Excavation in Clay Subjected to Hydraulic Uplift*, Advanced Topics in Science and Technology in China, DOI 10.1007/978-3-662-46507-3_4

4.2 Finite Element Analysis

To back-analyse the case history, coupled-consolidation analysis was carried out by a finite element program ABAQUS. In addition to the back-analysis, three numerical analyses were conducted to simulate the same excavation but with only upper half of grouted prop, with only bottom half of grouted prop and without prestress applied to steel props, respectively. One undrained analysis was also carried out. By comparing computed results from the four additional analyses to that from the back-analysis, the effects of grouted prop, prestress and dissipation of excess pore water pressure on ground deformations and soil-structure interaction of the excavation can be understood.

The diaphragm wall panel back-analysed in this chapter is located near the middle span of the excavation along its longitudinal direction (Panel 4, see Fig. 3.1). It is worth noting that the ratio of length over width of the excavation is larger than 8. Based on finite element analyses, Finno et al. (2007) concluded that any cross section near the middle span of an excavation with the ratio of length over width larger than 6 can be regarded as being under plane strain condition. In this numerical investigation, excavation at Panel 4 is simplified as a plane strain problem.

4.2.1 *Finite Element Mesh and Boundary Conditions*

Figure 3.3 shows cross section and geometry of Panel 4. Finite-element mesh and boundary conditions for back-analysing this panel is illustrated in Fig. 4.1. Depth of soil strata simulated is 50 m, as strata of important engineering properties for this excavation are about 50 m below the ground surface (Ng et al. 2012). To minimise boundary effect of the mesh, length of ground behind the wall is defined as 90 m

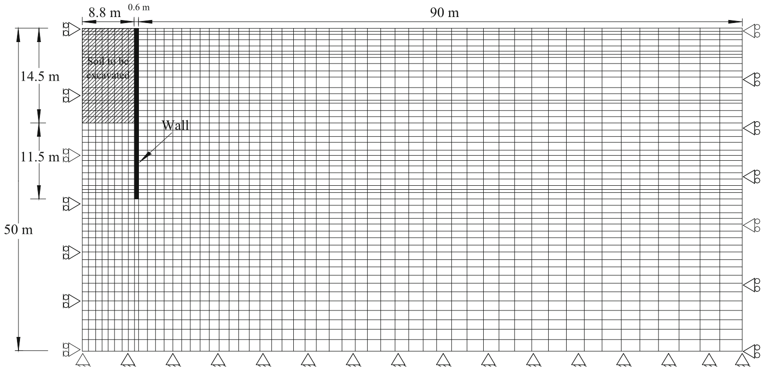

Fig. 4.1 Finite element mesh and boundary conditions

(i.e., 6 times of final excavation depth). All geometries for excavation (i.e. excavation width, excavation depth) and for structural elements (e.g. wall depth, wall thickness, vertical prop spacing and thickness of grouting) in the finite element mesh are identical to those in the case history documented in Chap. 3.

Lateral boundaries and bottom boundary of the finite element mesh are fixed by roller supports and pinned supports, respectively. Initial water table is defined at −0.6 m.

4.2.2 Constitutive Model and Model Parameters

As Shanghai clays are mainly normally consolidated with a thin layer of slightly over-consolidated clay near the ground surface (Wang et al. 2005), Modified Cam-Clay (MCC) constitutive law is adopted to model the soil.

Soil parameters for MCC are mainly determined according to laboratory testing results of relatively undisturbed soil samples, which are obtained by thin-wall tube sampler from a borehole close to Panel 4 (BH in Fig. 3.1). Slopes of compression and swelling line in e-lnp' space (i.e., λ and κ, respectively) are deduced from compression and recompression indices (i.e., C_c and C_r, respectively), which are measured by odometer tests. The relationships are given as follows:

$$\lambda = C_c/2.3 \tag{4.1}$$

$$\kappa = C_r/2.3 \tag{4.2}$$

Based on odometer tests, the void ratio at $p' = 1$ kPa at critical state line in e-lnp' space (i.e., Γ) could also be determined. With effective angle of shearing resistance ϕ' of each layer measured by triaxial drained tests, the stress ratio M_c (for compression) can be deduced by:

$$M_c = 6\sin\phi'/(3 - \sin\phi') \tag{4.3}$$

Stress ratio of triaxial compression (M_c) is simply assumed to be identical to that for triaxial extension (M_e). Since Shanghai clays are generally normally consolidated, the coefficient of lateral earth pressure at rest, K_o are estimated by Jáky's Equation (1944):

$$K_o = K_{nc} = 1 - \sin\phi' \tag{4.4}$$

Effect of construction of diaphragm wall on lateral earth pressure coefficient is not considered (explained later). The saturated vertical and horizontal permeabilities (k_v and k_h) were determined by laboratory constant head tests. Poisson's ratio (μ', in terms of effective stress) of each soil layer is determined based on that back-analysed from a similar case history in Shanghai clays (Ge 2002). Table 4.1 summarises all soil parameters adopted in numerical analyses for this study.

The retaining structures (i.e., prop and wall) are assumed to be elastic within working load range. The Young's modulus (*E*) of concrete (for diaphragm wall and Prop 1) and steel is taken as 30 and 200 GPa, respectively. The jet grouting is simulated as an elasto-plastic material with Mohr-coulomb failure criterion. Based on Hu et al. (2003), Young's modulus, effective cohesion and effective angle of shearing resistance of jet grouting are taken as 100 MPa, 250 kPa and 30º, respectively. Poisson's ratio for concrete and steel is taken as 0.2 (Ge 2002) while that for jet grouting is defined as 0.3 (Hu et al. 2003).

4.2.3 Numerical Modelling Procedure

The in situ construction stages essentially consist of dewatering, excavation and propping. Dewatering is only conducted on excavated side. The water level is remained at 1 m below the formation level of the excavation. In the numerical analysis, dewatering is simulated by setting a zero pore pressure at the level where water table should be maintained. Excavation is simulated by ramp linearly deactivating soil elements on the excavated side. While excavation is reduced to each pre-determined level, prop elements are activated simultaneously, with a prestress. The magnitude of applied prestress is determined according to that in the field (see Chap. 3). In this numerical simulation, the duration for main stages is defined exactly the same as the real situation. No creep effect is considered. Detailed numerical modelling procedure is summaried in Table 4.2. The diaphragm wall is assumed to be wish-in-place. In spite of the awareness that construction of diaphragm wall could change stress state and stress history of soil in vicinity to the wall, diaphragm walling is not simulated, because the relatively simple elasto-plastic model (MCC) adopted in this numerical analysis does not take strain dependency and stress-path dependency of soil into account. This numerical investigation only focuses on ground deformations and soil-structure interaction during main excavation.

4.3 Comparison of Measured and Computed Results

4.3.1 Lateral Wall Displacement

Figure 4.2 shows comparison of measured and back-analysed lateral displacement of wall (δ_h) in three selected stages during excavation. At the first stage of excavation (Stage I), no obvious cantilever-type of wall displacement is observed from both measured and back-analysed results. This is mainly owing to installation of the first prop (at 0.5 m) prior to the main excavation. As the excavation proceeded, both computed and back-analysed lateral wall displacement increased with the

Table 4.1 Soil parameters adopted in numerical analyses

Stratum	Bottom level (m)	λ	κ	ϕ'	K_0	M_c	e_0	Γ	γ_d (kN/m^3)	k_v (m/s)	k_h (m/s)
Medium-soft clay	−3.5	0.10	0.03	29	0.50	1.16	1.01	1.20	13.8	4.3×10^{-9}	1.2×10^{-8}
Soft silty clay	−7.5	0.15	0.04	27	0.54	1.07	0.93	1.35	12.4	7.7×10^{-9}	4.4×10^{-8}
Medium-soft clay	−17.0	0.11	0.03	26	0.55	1.03	1.19	1.57	12.2	4.3×10^{-9}	6.0×10^{-8}
Medium clay	−29.0	0.08	0.02	31	0.49	1.24	1.40	1.72	12.4	4.2×10^{-9}	1.1×10^{-8}
Medium silty clay	−50.0	0.07	0.02	30	0.50	1.20	1.21	1.53	12.9	2.4×10^{-9}	4.2×10^{-8}

Table 4.2 Numerical modelling procedure

Stage		Day No.	Construction activity
Main excavation	I	1–2	Cast Prop 1 and excavated to Level 1 (−0.5 m)
	II(a)	3–5	Excavate to Level 2 (−4.5 m)
	II(b)	6	Install Prop 2 (−4 m)
	III(a)	7–13	Excavate to Level 3 (−8 m)
	III(b)	14	Install Prop 3 (−7.5 m)
	IV(a)	15–26	Excavate to Level 4 (−11.5 m)
	IV(b)	27	Install Prop 4 (−11 m)
	V	28–40	Excavate to Level 5 (−14.5 m)

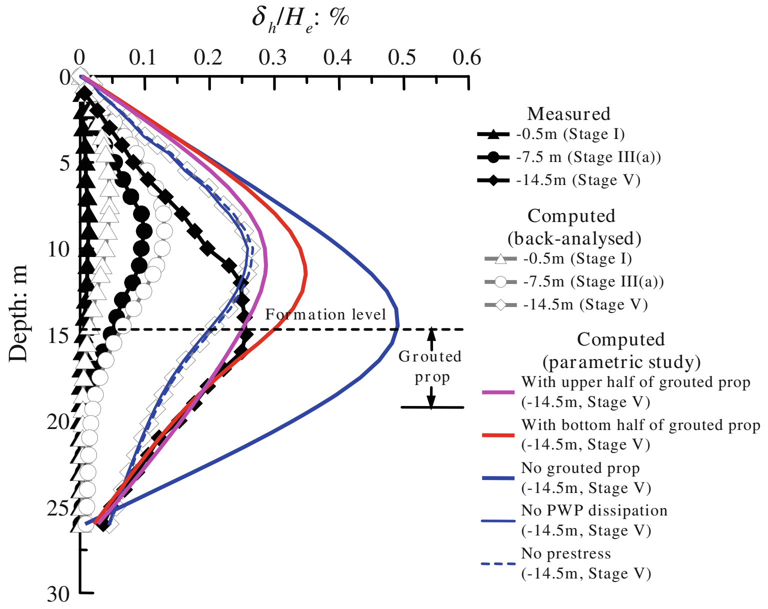

Fig. 4.2 Comparison of measured and computed lateral wall displacement

maximum lateral wall movement ($\delta_{h\text{-max}}$) of a deep-seated deformation profile moving downward. At early stages (i.e., stages I and III(a)), the back-analysed $\delta_{h\text{-max}}$ was larger than that measured. This is likely due to two major reasons. First, non-linearity of soil stiffness at small strains is not considered in MCC model. This probably leads to underestimation of soil stiffness in the numerical analysis at early excavation stages. Second, soil adjacent to the wall was subjected to horizontal loading during concreting prior to excavation (for construction of diaphragm wall) while subjected to horizontal unloading after commencement of excavation. The resulted reversal in the direction of stress path for soil adjacent to the wall should have increased its stiffness. Ignorance of stress path dependency of soil in MCC model also results in underestimation of soil stiffness. In spite of underestimated soil stiffness due to ignorance of strain dependency and stress path dependency in MCC model, effect of the two are shown to become less significant as excavation proceeded (i.e., difference between measured and back-analysed $\delta_{h\text{-max}}$ becomes smaller). At the end of excavation, back-analysed $\delta_{h\text{-max}}$ is only 5 % larger than the measured one. However, the back-analysed location of $\delta_{h\text{-max}}$ was about 5 m higher than that measured. It appears that in the numerical analysis, the downward movement of the deep-seated deformation profile of the wall had been over-constrained by the grouted prop near the formation level. If so, the stiffness of grouted prop defined in the numerical analysis might be overestimated.

Both measured and back-analysed $\delta_{h\text{-max}}$ (at the end of main excavation) are no more than 0.27 % of final excavation depth (H_e). This $\delta_{h\text{-max}}$ is smaller than that measured in most of excavations in soft clay reported by Long (2001) and Moormann (2004). Liu et al. (2005) also observe smaller lateral wall displacements (compared to database worldwide) in one excavation in Shanghai and consider this is due to use of pre-stressed props and grouted prop. In the meantime, time dependency of $\delta_{h\text{-max}}$ (due to dissipation of excess pore water pressure) was observed from the site.

To de-couple effect of prestressed prop, grouted prop and dissipation of pore water pressure on lateral wall displacement, numerical parametric studies were also carried out. Computed results (shown in Fig. 4.4) reveal that if grouted prop was not installed, $\delta_{h\text{-max}}$ may have been increased by 66 %. Moreover, presence of the upper half of the grouted prop is shown to be more effective in reducing $\delta_{h\text{-max}}$ (explained later). Compared to grouted prop, effects of prestressed props and dissipation of excess pore water pressure on $\delta_{h\text{-max}}$ are much less significant (i.e., with percentage differences of 1 and 2 %, respectively). The relatively insignificant increment of $\delta_{h\text{-max}}$ due to dissipation of excess pore water pressure is likely to be relevant to the relatively rapid excavation rate (daily excavation ratio is about 0.37 m deep) in this study. Liu et al. (2005) reported one similar multi-propped excavation (15.5 m deep) in Shanghai. Average excavation rate of the reported excavation is 0.14 m deep per day, which is about 2.5 times slower than that in this site. As a result, percentage increment of $\delta_{h\text{-max}}$ due to dissipation of excess pore water pressure in the reported excavation (about 8.6 %) is more than 4 times of that back-analysed in this study (about 2 %).

4.3.2 Ground Surface Settlement

Figure 4.3 shows comparison of measured and computed ground surface settlements behind the retaining wall during excavation. It should be noted that in this numerical analysis, the dewatering activity conducted at Stage V near Panel 4 for artesian release (details are given in Chap. 3) was not simulated. Thus, comparison

Fig. 4.3 Comparison of measured and computed ground surface settlement

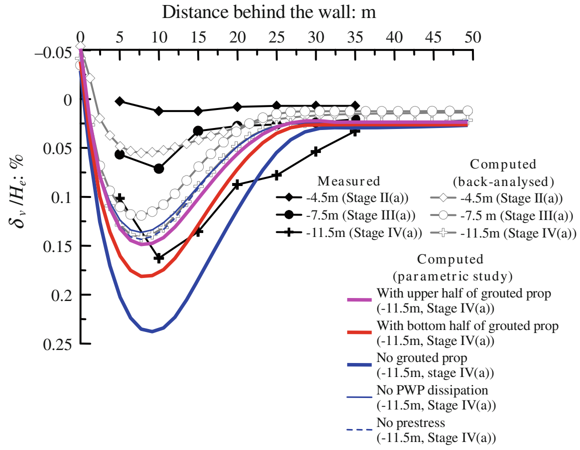

of computed and measured ground surface settlement at Stage V is not included in Fig. 4.3.

Both measured and back-analysed concave settlement profiles were in a concave shape, which is corresponding to deep seated deformation shape of the wall (Fig. 4.2). It can be seen that at early stage (Stage II(a)), back-analysed maximum ground surface settlement $\delta_{v\text{-max}}$ overestimated that measured by a factor of about 3. The accumulative ground settlement at later stages of excavation (stages III(a) and IV(a)) becomes less influenced by the variation of soil stiffness at small strains, compared to that at Stage II(a). At Stage IV(a), the percentage difference between measured and back-analysed $\delta_{v\text{-max}}$ is about 9 %. This seems to imply that near the end of excavation, soil strain in the vicinity to the excavation is beyond very small stain level (evident later) and hence $\delta_{v\text{-max}}$ is less influenced by the non-linearity of soil stiffness at small strains. However, ground settlement at locations relatively far away from the excavation is still relevant to small strain stiffness. As expected, measured influence zone of ground settlement behind the wall is much less extended than that back-analysed. Similar observations were made from computed ground settlement using relatively simple elasto-plastic models (Burland 1989; Ng 1992; Simpson 1992; Whittle and Hashash 1994). Near the wall, some ground heave was computed. This is a common observation while adopting MCC in numerical analysis (Whittle and Hashash 1994). One major reason is considered to be ignorance of stress path dependency of unloading modulus of soil in side of the excavation. This underestimates the unloading modulus and hence leads to an overestimated basal heave.

Comparison of computed results between back-analysis and parametric study reveals that presence of grouted prop could have reduced $\delta_{v\text{-max}}$ by 81 %. Compared to bottom half of groupted prop, the upper half is shown to be more effective in reduction of $\delta_{v\text{-max}}$. Due to use of prestressed props and dissipation of excess pore water pressure, percentage differences in $\delta_{v\text{-max}}$ are only 1 % and 2 %, respectively.

4.3.3 Contour of Deviatoric Strain

General agreement between measured and computed lateral wall displacement (Fig. 4.2) and ground surface settlement (Fig. 4.3) gives confidence to computed shear strain. Figure 4.4a shows contour of back-analysed incremental deviatoric strain due to main excavation. On the excavated side, the most significant shear strain was developed near the formation level (where substantial shearing took place) and near the wall toe (due to shearing between the wall toe and soil underneath). Shear strain developed on the excavated side is no more than 0.5 %, which is even less than that back-analysed in a shallower multi-propped excavation (with a final excavation depth of two thirds of that in this study) in stiff clay (Ng et al. 1998). It is worth noting that grouted prop was not applied in the excavation reported by Ng et al. (1998). Use of grouted prop inside the excavation in this study would have reduced mobilised shear strain (or shear strength) of soil in front of the wall by increasing passive resistance. On the retained side, the most significant shear strains (in the range of 0.2–0.3 %) developed the location where the maximum lateral wall displacement took place. The influence zone of shear strain due to excavation is about one time of excavation depth behind the wall, within which the maximum ground surface settlement behind the wall was located (Fig. 4.4a). The computed maximum incremental shear strain behind the wall is close to that deduced from field measurement in a multi-propped excavation in Taipei soft clay (Ou et al. 2000), where the maximum shear strain was about 0.4 % at an excavation depth of 15.2 m. Based on back-analysed strain levels around excavation, an appropriate stiffness of soil could be determined (based on measured stress-strain relationships from laboratory tests) and used as input parameters while applying simple elasto-plastic models for future design.

Figure 4.4b shows contour of computed incremental deviatoric strain due to excavation in an analysis without grouted prop. It can be seen that the maximum deviatoric strain is developed near the formation level of the excavation. Therefore,

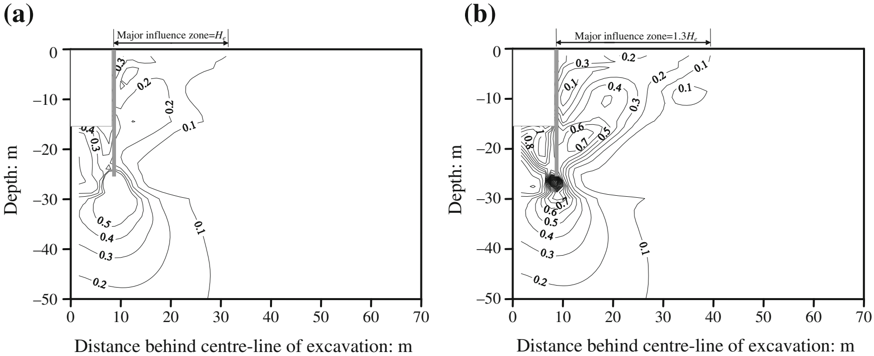

Fig. 4.4 Computed incremental deviatoric strain due to excavation. **a** Analysis with grouted prop (back-analysis); **b** Analysis without grouted prop (parametric study)

the most effective way to reduce excavation-induced shear strain and hence ground deformation is to install grouted prop near the formation level, instead of a few metres below the formation level. This explains why the upper half of grouted prop works more effectively in reducing lateral wall displacement and ground settlement, than the bottom half of grouted prop (see Figs. 4.2 and 4.3, respectively). Comparison of deviatoric strain between analyses with (Fig. 4.4a) and without grouted prop (Fig. 4.4b) reveals that without presence of grouted prop, mobilised deviatoric strain on the excavated and retained sides may be increased by 2.5 and 2.3 times, respectively. Absence of grouted prop also results in a 30 % wider influence zone of deviatoric strain behind the wall. Moreover, location of the maximum deviatoric strain behind the wall in the analysis without grouted prop is lower than that in the analysis with grouted prop. This is because the maximum lateral wall displacement in the case with absence of grouted prop took place at lower elevation (more deep-seated), compared to that with grouted prop (Fig. 4.2).

4.3.4 Mobilisation of Undrained Shear Strength

Figure 4.5 compares computed mobilised undrained shear strength c_{u_mob} (normalised by initial shear strength c_u) with excavation depth h (normalised by final excavation depth H_e) in analyses with and without grouted prop. In each analysis, two soil elements located in front of the wall were selected for comparison (i.e., elements A and B, see the inset in Fig. 4.5). In the same figure, reversal in direction of stress path (from triaxial compression to triaxial extension) of each soil element is also illustrated by open circular symbols.

For each soil element (in both analyses), it can be seen that mobilisation of undrained shear strength decreased with excavation depth first and then increased. This is because soil in front of the wall is under compression ($\sigma'_v < \sigma'_h$) before

Fig. 4.5 Computed moblisation of undrained shear strength

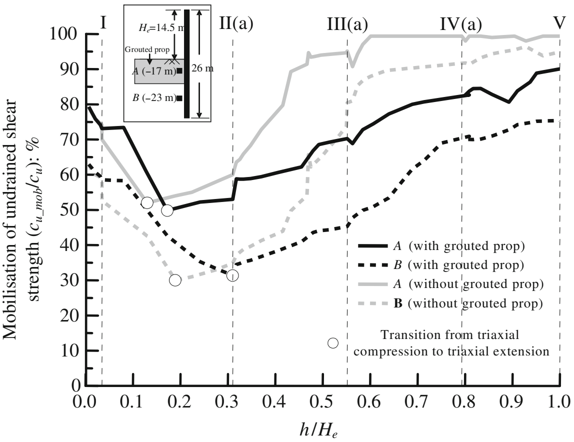

excavation. Commencement of excavation leads to a reduction in σ'_v and a relatively constant σ'_h (Ng et al. 2012), resulting in a reduced deviatoric stress (i.e., reduced mobilisation of c_{u_mob}). As σ'_v becomes less than σ'_h, shearing mode was changed from triaxial compression to triaxial extension. After this reversal in direction of effective stress path, further reduction of σ'_v due to subsequent excavation leads to an increase in deviatoric stress (i.e., increased c_{u_mob}). It can be seen that the reversal in the direction of effective stress path of soil elements in the analysis with grouted prop occurred at slightly larger excavation depth than that in the analysis without grouted prop. Due to presence of grouted prop, part of the passive load should have been transferred from soil to grouted prop. This induces a smaller σ'_h (at each excavation depth) in the analysis with grouted prop than that in the analysis without grouted prop. Hence, a larger reduction of σ'_v (i.e., a lager excavation depth) is required in the case with grouted prop to make σ'_v equal to σ'_h (transition from triaxial compression to triaxial extension).

After the reversal in the direction of stress path, undrained shear strength of soil elements in the case with grouted prop mobilised much less that in the case without grouted prop at each given excavation depth. This is as a result of increased passive resistance due to presence of grouted prop in front of the wall. With absence of grouted prop, undrained shear strength near the formation level of the excavation (Element A) was fully mobilised at early Stage IV(a). By installing grouted prop in front of the wall, full mobilisation of undrained shear strength at Element A had been prevented during the entire process of excavation. At deeper depth (Element B), undrained shear strength in both cases with and without grouted prop did not fully mobilised during excavation. But presence of grouted prop helped to reduce mobilisation of undrained shear strength by 20 %.

Corresponding to reduced mobilisation of undrained shear strength due to grouted prop, less shear strain was mobilised in front of the wall (Fig. 4.5). Accordingly, lateral wall displacement (Fig. 4.2) and ground surface settlement behind the wall (Fig. 4.3) were reduced.

4.3.5 Lateral Total Earth Pressure

Figure 4.6 illustrates distributions of measured and back-analysed lateral total earth pressures on both sides of wall before and after excavation (Stage V). Computed results from an analysis with absence of grouted prop are included for comparison. In the figure, two pressure limits (K_a and K_p lines) and design earth pressure distribution adopted in Shanghai are also included for reference. The K_a and K_p lines are calculated by adding the limiting horizontal effective stress based on Rankine's theory and pore water pressures measured at Stage V (at the end of the excavation) together. In calculating K_a and K_p pressures, ϕ' value for each soil layer is taken from Table 4.1. For retaining wall design in Shanghai, earth pressure behind the wall is empirically estimated as 0.7 times of total vertical earth pressure (SMCC 1997).

Fig. 4.6 Comparison of measured and computed lateral earth pressure

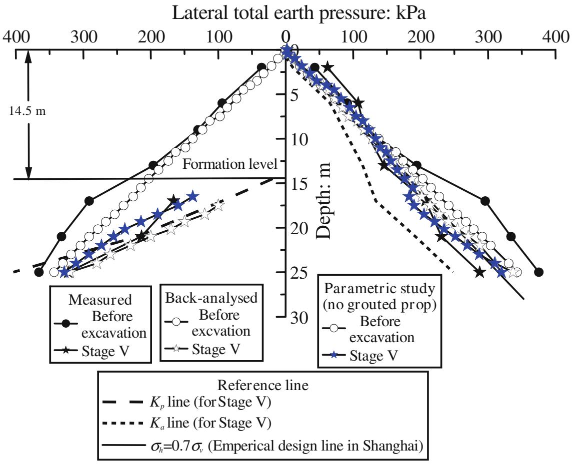

Before excavation, the back-analysed lateral earth pressure distribution is equivalent to at-rest lateral earth pressure, as construction of diaphragm wall is not simulated in the analysis. It can be seen that the measured lateral earth pressure (include effect of diaphragm walling) on both sides of the wall before excavation is larger than that computed. This is expected as construction of diaphragm wall in soft clay should have increased lateral earth pressure (see Chap. 3).

After excavation (Stage V), both measured and back-analysed lateral earth pressures within the propped region (on the retained side) increased, due to upward shear stress transfer (soil arching) during the multi-propped excavation (see Chap. 3). However, back-analysed increase of lateral earth pressure is much smaller than that measured. It is well recognised that magnitude of shear stress transfer depends on relative soil movement (related to lateral wall movement in this study) and soil stiffness. Since measured and back-analysed lateral wall movements (and hence relative movement between soil within the propped region and the region underneath) are similar (Fig. 4.2), it seems to imply that soil stiffness near the wall in the numerical analysis is less than that in the field. This is likely to occur due to ignorance of stain dependency and stress path dependency of soil stiffness in the current numerical analysis, as discussed. Probably because of the same reason, back-analysed reduction of lateral earth pressure on the retained side (excluding that within the propped region) due to excavation is less than that measured. Given grouted prop was absent, lateral earth pressure on the retained side above the formation level remains almost constant while that below the formation level decreases slightly. Therefore, absence of grouted prop mainly increased deviatoric strain below the formation level (see Fig. 4.4a, b). On completion of excavation, lateral earth pressure on the retained side for cases with presence of grouted prop (based on measured and back-analysed results) and without (based on parametric study) all stayed above K_a line. Moreover, it appears that design earth pressure in Shanghai (SMCC 1997) gives a reasonable first approximation of earth pressure behind the wall.

On the excavated side, the measured earth pressure near the formation level (EP5 (E)) approached the passive failure while that back-analysed stayed below the K_p line after excavation. It is worth noting that in the field, measured earth pressure is essentially contact pressure at soil wall interface. Near the formation level, where grouted prop was installed (Fig. 3.3), the measured contact pressure include pressure acting on the soil and on the grouted prop. While in this study, each present earth pressure was obtained from soil element adjacent to the wall. Therefore, comparison between measured and back-analysed earth pressures near the formation level may imply that part of the passive load could have been transferred to grouted prop such that less pressure acted on the soil. The figure shows that with absence of grouted prop, earth pressure near the formation level reached K_p line. As a result, much larger (2.5 times) deviatroric shear strain was developed near the formation level in the analysis without grouted prop (Fig. 4.4b), than that with grouted prop (Fig. 4.4a). At deeper depth on the excavated side (i.e., below 21 m), measured lateral total earth pressure is close to that back-analysed, both stayed below K_p line and were smaller than the computed earth pressure from the analysis without grouted prop. By comparing computed results from analyses with and without grouted prop, it can be readily calculated that presence of grouted prop leads to about 18 % reduction of resultant earth pressure in front of the wall. In another words, grouted prop should have shared 18 % of passive resistance from the soil.

4.3.6 Pore Water Pressure

Figure 4.7 shows computed contour of pore water pressure at the end of the excavation. Measured pore water pressures (on both sides of soil wall interface and at 4 m behind the wall) are also included for comparison. At soil wall interface, computed pore water pressure overestimated measured values at most of measuring points. In another words, computed results underestimate reduction of pore water

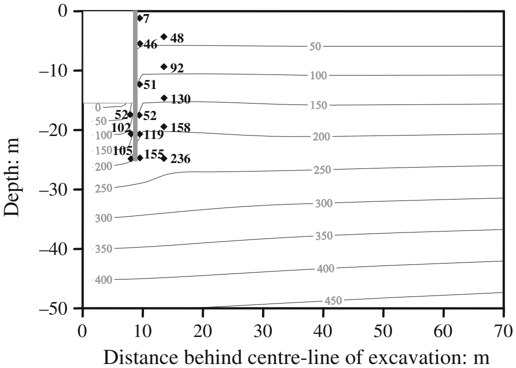

Fig. 4.7 Comparison of measured and computed pore water pressure

pressures at soil wall interface on both sides of the wall. This underestimation may be attributed to two major reasons. First, dewatering in the aquifer in the field is not simulated in the numerical analysis. Given the aquifer is connected with the soil wall interface, pore water pressures at the interface could have been reduced by the dewatering. Second, measured reduction of lateral total earth pressure on both sides of the wall is larger than that computed (as discussed). For pore water pressures in the soil (i.e., 4 m behind the wall), measured and computed results show a reasonable agreement. This gives confidence to computed pore water pressure contour.

As shown by the computed contour, reduction of pore water pressure due to excavation decreases with increasing depth and decreasing distance from the wall. On the excavated side, reduction of pore water pressure near the centre of the excavation is larger than that adjacent to the wall. This because negative excess pore water pressure near the wall should have been partially increased due to inward movement of the wall. The computed results also show that no negative pore water pressure was generated inside the excavation. Similar observation was made from measured pore water pressure inside an excavation in Taipei soft clay (Ou et al. 1998). This implies that in both excavations in normally consolidated clay (i.e., Shanghai soft clay and Taipei soft clay), negative excess pore water pressure due to unloading inside the excavation could have been cancelled out by positive excess pore water pressure due to shearing and inward movement of the wall. Different from response of pore water pressure in soft clay, negative excess pore water pressure was measured and computed inside an excavation in stiff clay (in the top few metres) at Lion yard, Cambridge (Ng et al. 1998). This is expected for heavily over-consolidated clay, in which negative pore water pressure could have been generated in response to both vertical unloading and shearing. Behind the wall, the computed results show that major influence zone of pore water pressure due to excavation is within about 1.5 m behind the wall. This is similar to that observed in an excavation in Taipei soft clay (Ou et al. 1998), in which influence zone of pore water pressure (on the retained side) in response to excavation is about 2 m behind the wall.

4.3.7 Apparent Earth Pressure

To verify applicability of existing apparent pressure envelopes for design, measured and computed (for analyses with and without grouted prop) highest prop load at each level was converted into apparent earth pressure, as shown in Fig. 4.8. The pressure envelope proposed by Peck (1969) with $K = 1.0$ and the CIRIA design envelope (Twine and Roscoe 1999) for excavations supported by stiff walls in soft clay are included for comparison. In Fig. 4.8, each apparent earth pressure was normalised by γH_e.

It can be seen that back-analysed apparent earth pressure at each level is larger than that measured, with a maximum percentage difference of no more than 20 %.

Fig. 4.8 Comparison of measured and computed apparent earth pressure

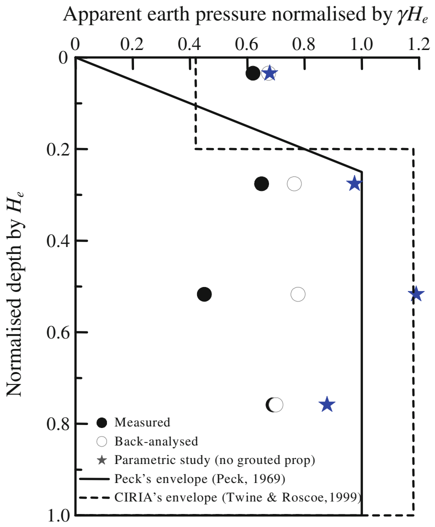

Larger back-analysed apparent earth pressure (i.e., prop load) than the measured result is attributed to larger computed lateral earth pressure (Fig. 4.6).

Comparison between computed results from analyses with and without grouted prop shows that the most significant reduction of prop load due to grouted prop was at the third prop, instead of the prop closest to grouted prop (i.e., Prop 4). This is probably due to the reason that Prop 4 did not become effective until the completion of the second last excavation stage. Due to presence of grouted prop, sum of maximum prop load at each level was reduced by about 28 %.

Compared to apparent earth pressure for cases with grouted prop (based on measured and computed results) and without (based on results from parametric study), existing pressure envelopes (i.e., Peck 1969 and Twine and Roscoe 1999) both failed to include apparent earth pressure at the highest prop. This may be due to the reason that the highest prop was installed before excavation and hence become effective immediately at the commencement of excavation. Apart from the highest prop, apparent earth pressures of the case with grouted prop are bounded by Peck's envelope. With absence of grouted prop, it appears CIRIA's envelope would be more applicable for estimation of prop load.

4.4 Summary and Conclusions

In this chapter, coupled-consolidation finite element analysis was carried out to back-analyse the case history documented in Chap. 3. Further numerical parametric studies (four in total) were conducted to investigate effects of grouted prop, pre-stressed prop and dissipation of excess pore water pressure on deformations and soil-structure interaction of multi-propped excavation in soft clay. Based on the numerical back-analysis and parametric study, the following conclusions can be drawn:

(1) At the end of main excavation, the computed maximum lateral wall displacement ($\delta_{h\text{-max}}$) and maximum ground surface settlement behind the wall ($\delta_{v\text{-max}}$) show a general agreement with measured data. Computed shear strain developed on the excavated side and retained side is no more than 0.4 and 0.3 %, respectively. Major influence zone of shear stain is within a full excavation depth behind the wall.

(2) Numerical analyses reveal that at the end of the excavation, about 18 % of passive load in front of the wall is transferred from soil to grouted prop. Because of the load sharing by grouted prop, mobilised undrained shear strength of clay in front of the wall is reduced by 20 % (on average). Potential passive failure of soil adjacent to the formation level of the excavation has been prevented. Reduced shearing and yielding of soil in front of the wall lead to a decrease of the maximum lateral wall displacement and maximum ground surface settlement by 66 and 81 %, respectively.

(3) Reduction of deformations benefit more from presence of the upper half of jet grouted prop than the bottom half. This is because the upper half of grouted prop is located near the formation level of the excavation, where most significant shear strain is induced by excavation.

(4) Compared to effect of grouted prop, effects of use of prestressed props and dissipation of excess pore water pressure on $\delta_{h\text{-max}}$ and $\delta_{v\text{-max}}$ are much less significant, both with percentage differences of no more than 2 %.

(5) Different from measured pore water pressure near formation level of an excavation in stiff clay (Ng 1998), negative excess pore water pressure was not measured and computed in this study in soft clay. Negative excess pore water pressure due to unloading inside the excavation in soft clay could have been cancelled out by positive excess pore water pressure due to shearing and inward movement of the wall.

References

Burland J (1989) Small is beautiful: the stiffness of soil at small strains. Can Geotech J 26(4): 499–516

Finno, RJ, Blackburn, TJ, Roboski, JF (2007) Three-dimensional effects for supported excavations in clay. J Geotech Geoenviron Eng, ASCE 133(1):30–36

Ge XW (2002) Response of a shield-driven tunnel of deep excavations in soft clay. PhD thesis, The Hong Kong University of Science and Technology

Hu ZF, Yue ZQ, Zhou J, Tham LG (2003) Design and construction of a deep excavation in soft soil adjacent to the Shanghai metro tunnels. Can Geotech J 40(5):933–948

Jáky J (1944) The coefficient of earth pressure at rest. J Soc Hung Arch and Eng, pp 355–358 (in Hungarian)

Liu, GB, Ng, CWW, Wang, ZW (2005) Observed performance of a deep multi-strutted excavation in Shanghai soft clays. J Geotech Geoenviron Eng, ASCE 131(8):1004–1013

Liu GB, Jiang J, Ng CWW, Hong Y (2011) Deformation characteristics of a 38 m deep excavation in soft clay. Can Geotech J 48(12):1817–1828

Long M (2001) Database for retaining wall and ground movements due to deep excavation. J Geotech Geoenviron Eng, ASCE 127(3):203–224

Moormann C (2004) Analysis of wall and ground movements due to deep excavations in soft soil based in a new worldwide database. Soils Found 44(1):87–98

Ng CWW (1992) An evaluation of soil-structure interaction associated with a multi-propped excavation. PhD thesis, University of Bristol

Ng CWW (1998) Observed performance of multi-propped excavation in stiff clay. J Geotech Geoenviron Eng, ASCE 124(9):889–905

Ng CWW, Simpson B, Lings ML, Nash DFT (1998) Numerical analysis of a multi-propped excavation in stiff clay. Can Geotech J 35(1):115–130

Ng CWW, Hong Y, Liu GB, Liu T (2012) Ground deformations and soil-structure interaction of a multi-propped excavation in Shanghai soft clays. Géotechnique 62(10):907–921

Ou CY, Liao JT, Lin HD (1998) Performance of diaphragm wall construction using top-down method. J Geotech Geoenviron Eng, ASCE 124(9):798–808

Ou CY, Liao JT, Cheng WL (2000) Building response and ground movements induced by a deep excavation. Géotechnique 50(3):209–220

Peck RB (1969) Deep excavation and tunneling in soft ground. In: Proceeding of the 7th international conference on soil mechanics and foundation engineering, Mexico City, State-of-the-Art Volume, pp 225–290

Simpson B (1992) Retaining structures: displacement and design. Géotechnique 42(4):541–576

SMCC (1997) Shanghai stand code for design of excavation engineering, DBJ-61-97. Shanghai Municipal Construction Committee, Shanghai

Tan Y, Wei B (2011) Observed behavior of a long and deep excavation constructed by cut-and-cover technique in Shanghai soft clay. J Geotech Geoenviron Eng, ASCE 138(1): 69–88

Twine D, Roscoe H (1999) Temporary propping of deep excavations: guidance on design. Construction Industry Research and Information Association, London C517

Wang ZW, Ng CWW, Liu GB (2005) Characteristics of wall deflections and ground surface settlements in Shanghai. Can Geotech J 42(5):1243–1254

Whittle AJ, Hashash YMA (1994) Soil modeling and prediction of deep excavatoin behavior. In: Proceedings of a conference on the pre-failure deformation of geomaterials (IS-Hakkaido'94), vol 1. Balkema, Rotterdam, The Netherlands, pp 589–595

Chapter 5
Dimensional Analysis of Excavation in Clay Subjected Hydraulic Uplift

5.1 Introduction

As summerised in Chap. 2, accidents and catastrophic basal failure associated with hydraulic uplift are reported worldwide from time to time (Milligan and Lo 1970; Ramaswamy 1979; Clough and Reed 1984; Davies 1984; Qu et al. 2002; Gue and Tan 2004). Concern on potential base instability due to hydraulic uplift is also raised in the case history reported in Chap. 3. In spite of the frequently encountered base instability due to hydraulic uplift, this subject has not been studied systematically and well understood. To assist with systematic study of this subject, dimensional analysis is carried out in this chapter to propose key variables (expressed in dimensionless groups) to be considered in this study. Effects of the proposed dimensionless groups on basal response to hydraulic uplift are investigated by centrifuge tests and finite element analyses (results reported in Chaps. 8 and 9).

This chapter consists of three parts. First, variables which are potentially relevant to basal resistance against hydraulic uplift are listed, based on implications from a similar but relatively well studied subject (clay subjected to uplifting anchor). Finally, a back of envelope calculation is conducted to reveal mechanisms involved and to indentify key dimensionless groups related to this subjected.

5.2 Variables Affecting Basal Resistance Against Hydraulic Uplift

Figure 5.1 shows a schematic diagram of excavation in clay overlying an aquifer. To figure out possible variables related to basal resistance against hydraulic uplift, a simple analogy may be made with a similar but much better studied subject, i.e., uplift resistance of anchor embedded in clay (Meyerhof and Adams 1968; Davie and Sutherland 1977; Rowe and Davis 1982; Sutherland 1988; Merifield et al.

Y. Hong and L. Wang, *Deformation and Failure Mechanism of Excavation in Clay Subjected to Hydraulic Uplift*, Advanced Topics in Science and Technology in China, DOI 10.1007/978-3-662-46507-3_5

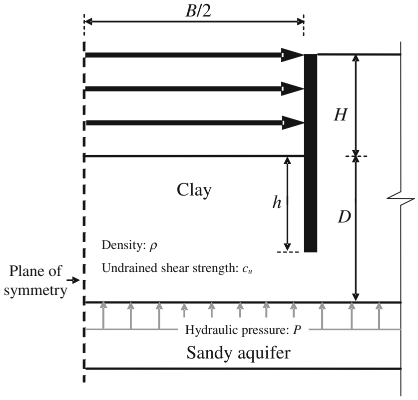

Fig. 5.1 A schematic diagram showing excavation in clay subjected to hydraulic uplift

1999, 2001; Thorne et al. 2004). These extensive studies reveal that uplift resistance of rapidly loaded strip anchor in clay mainly depends on width of anchor, embedded depth of anchor, undrained shear strength of clay, tensile strength of clay, bulk density of clay. Based on the implications from uplifting anchor in clay, it may be reasonable to assume that basal resistance of excavation in clay against 'rapid' hydraulic uplift (P) is relevant to the following variables (defined in Fig. 5.1):

(a) for clay: undrained shear strength (c_u), tensile strength (τ), density (ρ);
(b) for excavation: excavation width (B), excavation depth (H), embedment depth of wall into clay (h), thickness of clay inside excavation (D);
(c) for both clay and excavation: gravitational acceleration (g).

Therefore, P may be function of the variables listed above:

$$P = f(r, g, c_u, \tau, D, B, H, h) \tag{5.1}$$

where ρ is density of clay (ML^{3}), g is gravitational acceleration (LT^{2}), c_u is undrained shear strength of clay ($ML^{1}T^{2}$), τ is tensile strength of clay ($ML^{1}T^{2}$), D is thickness of excavation base (L), B is width of excavation (L), H is depth of excavation (L), h is penetration depth of retaining wall (L).

5.3 Dimensional Analysis

Based on Buckingham's π method, at least one dimensionless group consists of independent variables different dimensions (i.e., mass, length and time) should be selected in dimensional analysis. Preferably, the selected dimensionless group should have a clear physical meaning. In this study, independent variables are selected to be ρ, g and D. Physical meaning of the resulted dimensional group ρgD is overburden pressure of clay inside excavation.

By normalising each term in Eq. (5.1) using the selected independent variables (i.e., ρ, g and D), Eq. (5.1) can be expressed in dimensionless form:

$$P/\rho gD = f(c_u/(\rho gD), \tau/(\rho gD), B/D, H/D, h/D) \tag{5.2}$$

According to Fang and Chen (1972), τ/c_u is a constant over a large plasticity range. Therefore, the dimensionless groups given in Eq. (5.2) can be reduced to:

$$P/(\rho gD) = f(c_u/(\rho gD), B/D, H/D, h/D) \tag{5.3}$$

5.4 Key Dimensionless Groups for This Study

Given the resulted dimensionless groups from dimensional analysis (given in Eq. (5.3)), relevancy of each term to hydraulic uplift problem still can not be prioritised. By conducting a back of envelope calculation, mechanisms involved for this problem can be revealed and key dimensionless groups related to this subject can be identified.

Clay inside excavation subjected to rapid hydraulic pressure (Fig. 5.2a) can be simplified as a clay beam loaded by upwards uniformly distributed load at its bottom (Fig. 5.2b). It is valid to assume the clay as a beam only when it is loaded rapidly under ‘undrained’ condition. Under this circumstance, apparent cohesion of the clay allows it to sustain bending induced total tensile stress (Thusyanthan et al. 2007). As shown in Fig. 5.2b, clay beam inside excavation is fixed by roller supports along the centre-line of the excavation while its boundary condition along the soil-wall interface is simplified as pinned supports.

When the clay beam is loaded by a net upwards hydraulic pressure (p), bending moment and shear force would be induced in the beam. As shown in the bending moment diagram (Fig. 5.2b), the maximum bending moments are developed along the centre-line of the excavation and soil-wall interface. These bending moments result in change of horizontal stress in the beam. The bending induced change of horizontal stress ($\Delta\sigma_h$) may lead to failure of soil in triaxial compression (where $\Delta\sigma_h$ decreases) or triaxial extension (where $\Delta\sigma_h$ increases). Shear force diagram in Fig. 5.2b shows the maximum shear force is induced along the soil-wall interface. The resulted shear stress (τ) may lead to soil failure in simple shear. Bending induced $\Delta\sigma_h$ and shearing induced τ are quantified, as shown in Fig. 5.2b. It can be seen that $\Delta\sigma_h$ and τ show a linear relationship with $(B/D)^2$ and B/D, respectively. This implies that for a wider excavation (when B/D is than 1), bending moment induced $\Delta\sigma_h$ can be much larger than shear force induced τ. As a result, dominating failure mode of soil beam inside excavation would be triaxial compression and triaxial extension. While for a narrower excavation (when B/D less than 1), τ may

Fig. 5.2 **a** Problem defined; **b** A simplified model for back of envelope calculation

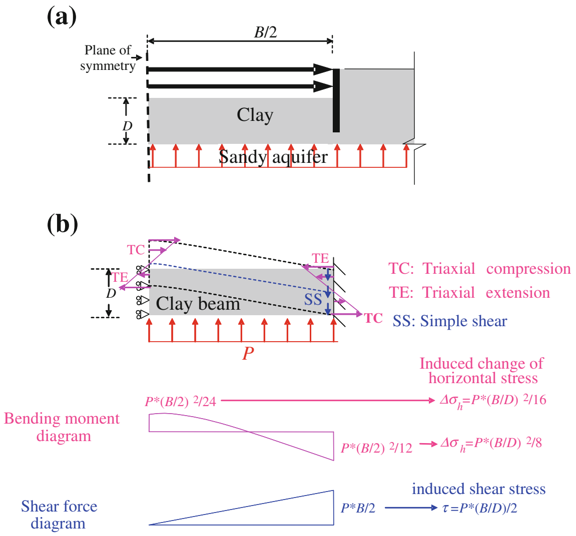

be much larger than $\Delta\sigma_h$. Accordingly, failure of soil inside the excavation would be dominated by simple shear.

The analysis above suggests that *B/D* is a key dimensionless group governing failure of a soil beam subjected to hydraulic uplift. Moreover, mobilisable $\Delta\sigma_h$ and τ in a soil beam depend on undrained shear strength of the soil (c_u). Therefore, *B/D* and $c_u/(\rho g D)$ are likely to be most relevant to basal resistance against hydraulic uplift (*P*), among all dimensionless groups in Eq. (5.3).

References

Clough GW, Reed MW (1984) Measured behaviour of braced wall in very soft clay. J Geotech Eng Div, ASCE 110(1):1–19

Davie JR, Sutherland HB (1977) Uplift resistance of cohesive soils. J Geotech Div, ASCE 103 (9):935–952

Davies (1984) Some geotechnical problems with foundations and basements in Singapore. In: Proceedings of international conference on tall buildings, Singapore, 22–26, October

Fang, HY, Chen WF (1972) Further study of double-punch test for tensile strength of soils. In: Proceedings of the 3rd Southeast Asian conference on soil engineering, Hong Kong, pp 211–215

Gue SS, Tan YC (2004) Two case histories of basement excavation with influence on groundwater. Keynote Lecture, In: International Conference on Structural and Foundation Failures (ICSFF), Singapore, 2nd–4th August

Merifield RS, Sloan SW, Yu HS (1999) Stability of plate anchors in undrained clay. Research Report No. 174.02.1999, University of Newcastle, Australia

Merifield RS, Sloan SW, Yu HS (2001) Stability of plate anchors in undrained clay. Géotechnique 51(2):141–153

Meyerhof GG, Adams JI (1968) The ultimate uplift of foundations. Can Geotech J 5(4):225–244

Milligan V, Lo KY (1970) Observations on some basal failures in sheeted excavations. Can Geotech J 7(2):136–144

Qu JL, Liu GB, Zhang JF (2002) Study on the ground settlement induced by artesian pressure release at Dongchang road metro station. China Civ Eng J 35(5):93–98

Ramaswamy SD (1979) Some aspects of practice and problems of foundations in Singapore. In: Proceeding of 6th Asian regional conference on soil mechanics and foundation engineering, Singapore

Rowe RK, Davis EH (1982) The behaviour of anchor plates in clay. Géotechnique 32(1):9–23

Sutherland HB (1988) Uplift resistance of soils. Géotechnique 38(1):493–516

Thorne CP, Wang CX, Carter JP (2004) Uplift capacity of rapidly loaded strip anchors in uniform strength clay. Géotechnique 54(8):507–517

Thusyanthan NI, Take WA, Madabhushi SPG, Bolton BM (2007) Crack initiation in clay observed in beam bending. Géotechnique 57(7):581–594

Chapter 6
Centrifuge Modelling of Multi-propped Excavation in Clay Destabilised by Hydraulic Uplift

6.1 Introduction

In this chapter, fundamentals of centrifuge modelling technique are introduced. Centrifuge test program and objectives of the tests are presented. Then a new experimental setup developed for in-flight simulation of multi-propped excavation in soft clay destabilised by hydraulic uplift is described in detail. Finally, a description of model preparation and experimental procedure is given.

6.2 Principles and Scaling Laws

It is well recongnised that soil behaviour is governed by effective stress (i.e., current stress state and stress history). The fundamental principle of centrifuge modelling is to re-create the stress conditions that would exist in a full-scale construction (prototype), using a model of a greatly reduced dimension, such that the soil could exhibit corresponding behaviour as that in the field. This is achieved by subjecting the model to a centrifugal acceleration of Ng, where g is gravitational acceleration of the Earth (9.81 m/s^2). While a soil model (with a density of ρ) is subjected to an acceleration of Ng, its vertical stress of the soil model σ_{vm} at a depth h_m (in model scale) is equal to:

$$\sigma_{vm} = \rho Ng\, h_m \tag{6.1}$$

Y. Hong and L. Wang, *Deformation and Failure Mechanism of Excavation in Clay Subjected to Hydraulic Uplift*, Advanced Topics in Science and Technology in China, DOI 10.1007/978-3-662-46507-3_6

and for the prototype

$$\sigma_{vp} = \rho g\, h_p \tag{6.2}$$

According to the fundamental principle of centrifuge, σ_{vm} should be identical to σ_{vp}:

$$\rho N g h_m = \rho g\, h_p \tag{6.3}$$

or

$$h_p / h_m = N \tag{6.4}$$

Therefore, the scaling law for length is $1/N$. Based on this basic scaling factor, it can be deduced that moment of inertia (function of fourth power of length) of a retaining wall is $1/N^4$.

As far as diffusion problems (i.e., consolidation, heat flow, or contaminant transportation) are concerned, they are governed by the differential equation as follows:

$$\partial u/\partial t = c_v(\partial^2 u/\partial z^2) \tag{6.5}$$

where u denotes pore pressure, temperature, or pollutant concentration; t denotes time; c_v is a material constant: the coefficient of consolidation or diffusion coefficient; z represents a length dimension (i.e., drainage path for consolidation problem). The pore water pressure, u, in a diffusion problem is a hydrostatic stress, in which scaling factor is 1:1 and. Thus, the dimensional similarity of Eq. (6.5) is:

$$t_{m(dif)} = L_m^2 / c_{v(m)} = (L_p/N)^2 / c_{v(p)} \tag{6.6}$$

If the same soil and pore fluid are used in the model and the prototype (i.e., $c_{v(m)} = c_{v(p)}$), scaling factor for time is:

$$t_{m(dif)} = t_{p(dif)} / N^2 \tag{6.7}$$

Accordingly, time required for diffusion processes in the model is $1/N^2$ of that in the prototype.

Table 6.1 summerises relevant scaling factors used in the centrifuge model tests in this study.

Table 6.1 Scale factors for centrifuge tests in this study

Parameter	Prototype	Model scale	Parameter	Prototype	Model scale
Gravitational acceleration	1	N	Strain	1	1
Linear dimension	1	$1/N$	Force	1	$1/N^2$
Area dimension	1	$1/N^2$	Time (consolidation)	1	$1/N^2$
Density	1	1	Moment of inertia	1	$1/N^4$
Mass	1	$1/N^3$	Axial load	1	$1/N^2$
Displacement	1	$1/N$	Bending moment	1	$1/N^4$
Stress	1	1	Bending moment (under plane strain)	1	$1/N^3$

6.3 Limitations of Centrifuge Modelling

6.3.1 Variation of Centrifugal Acceleration with Model Depth

In centrifuge model test, centrifugal acceleration slightly increases with model depth, because of varied radial distance from centre of rotation to soil at different depth. Figure 6.1 shows distribution of vertical stress in the model scale and in its corresponding prototype. It is worth noting that the nonlinear variation of stress in the model is shown exaggerated for clarity. The maximum error is:

$$r_u = r_o = h_m/(6R_e) \tag{6.8}$$

where r_u and r_o are the ratios of the maximum under-stress and overstress to the prototype stress respectively. The effective centrifuge radius (R_e) is:

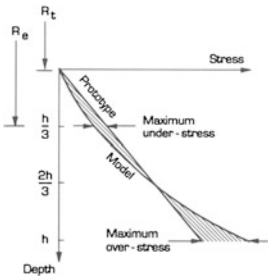

Fig. 6.1 Stress variation with depth in centrifuge model compared with a corresponding prototype

$$R_e = R_t + h_m/3 \tag{6.9}$$

where R_t denotes radius from the centre of rotation to the top of the model. In this study, maximum error is about 2 % of stress in prototype.

6.3.2 Grain Size Effect

As a general guideline, Fuglsang and Ovesen (1988) suggested that significant grain size effects only occur in tests where grain size of soil exceeds 1/30 of an important dimension of a model structure.

For centrifuge test in clay, speswhite kaolin is commonly used due to its relatively high permeability and well characterised material properties. In centrifuge model tests involving retaining wall, Powrie (1986) examined ratio of height of model retaining wall in model scale and particle size of kaolin ($d_p = 2$ μm). Calculated ratios are 4×10^4 and 5×10^6 in model scale and prototype scale, respectively. These values were significantly high to be effectively similar. For centrifuge tests in this study, ratios of particle size of kaolin to height of retaining wall are 1.5×10^5 and 7.5×10^6 in model scale and prototype scale, respectively. The difference between these two numbers is even smaller that adopted in centrifuge tests reported by Powrie (1986). Grain size effect in centrifuge tests in this study is therefore considered to be negligible.

6.3.3 Boundary Effect

Since dimension of soil model in a centrifuge is greatly scaled down, friction between side wall and soil model should be minimised in order to simulate correct boundary conditions as those in prototype.

Mair (1979) used Duckham's 'Keenomax' L3 water pump grease as a lubricant, in an attempt to reduce friction at the soil-model box interface. The grease is an off white coloured lithium based product with water resistant properties. However, to enable a clear view for image processing (PIV analysis) from the Perspex window of a model box, colourless lubricant is preferred.

Powrie (1986) lubricated the model box with colourless silicone grease. Based on direct shear test results, Powrie (1986) reported coefficients of friction for kaolin-grease-solid interfaces are in the range of 0.01–0.02. Effects of friction on his reported centrifuge tests were also quantified. It was estimated that the total restraining force due to friction from all sources would be less than 10 % of the typical fully active force (including pore water pressure) on the retained side of the model wall above excavation level (Powrie 1986).

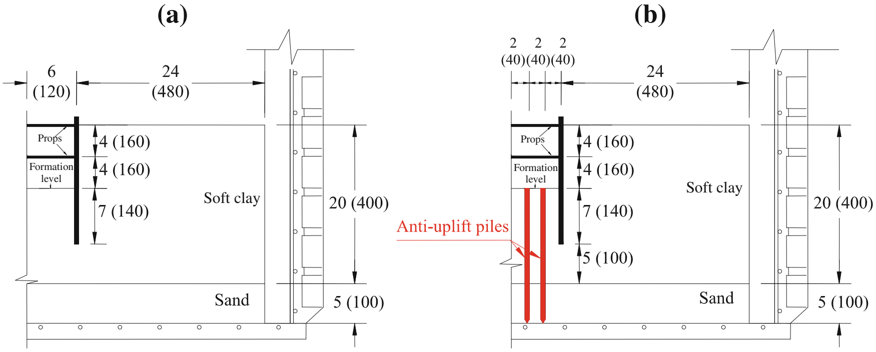

Fig. 6.2 Schematic diagrams: **a** test C_0.4 (without piles); **b** test C_0.4P (with piles) Note: (1) Numbers in parenthesis denote model scale (unit: mm); (2) In test ID (i.e., 'C_0.4' and 'C_0.4P'), 'C' refers to clay; '0.4' refers to the thickness of clay in model scale (i.e., 0.4 m); 'P' means the presence of piles

6.4 Test Program and Objectives

Figure 6.2 shows schematic diagrams (elevation views) of two centrifuge tests carried out in this study. In each test, an 8-m deep (in prototype) excavation was carried out in a 20-m thick (in prototype) soft clay layer underlain with a 5-m thick (in prototype) sandy aquifer. The only difference between the two tests is that in test C_0.4P, two rows of piles were installed in front of the wall. Four piles in each row were positioned along the direction normal to the section. Pile spacing along the direction in front of the wall and the direction normal to the section are 2*d* and 4.4*d* (*d* is pile diameter), respectively. The side boundaries were located a half pile spacing from the nearest piles.

Objectives of the two tests are:

- to investigate and understand failure mechanism of excavation in soft clay (with and without pile) destabilised by hydraulic uplift;
- to study effect of 'anti-uplift piles' in front of the wall on base stabilization.

6.5 Model Package

Plate 6.1 illustrates a typical model package of centrifuge tests carried out in this study. All centrifuge tests were performed at 50 g in a model box with a plane dimension of 600 mm × 350 mm (i.e., 30 m × 17.5 m in prototype) and a depth of 850 mm (i.e., 42.5 m in prototype). The model box is installed with a transparent side wall with a viewing area of 600 × 800 mm^2 (i.e., 30 m × 48 m in prototype).

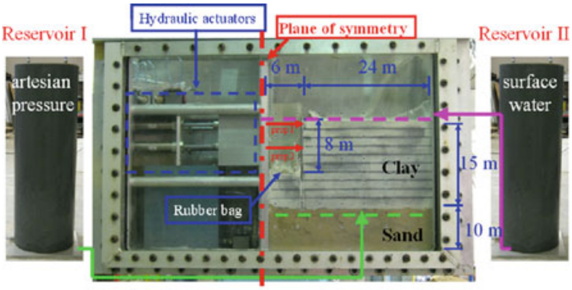

Note: Dimensions in prototype

Plate 6.1 A typical centrifuge model package

A digital camera with a maximum resolution of 2592 × 1944 pixels was mounted about 600 mm in front of the transparent side wall to capture digital images of the soil movement in the model box during each in-flight test. By processing two subsequent digital images with particle image velocimetry (PIV) analysis coupled with a close-range photogrammetry correction (White et al. 2003), soil movement can be quantified.

Only half of the excavation was simulated because of symmetry. The modelled excavation is carried out in a soft clay layer underlain with a sandy aquifer. Retaining system consists of a model wall and two levels of props (details are discussed later). Soil to be excavated was replaced by a rubber bag filled with zinc chloride solution, which has the same density as that of the clay sample (1.63×10^3 kg/m^3). Excavation was simulated by draining away zinc chloride solution. Model props were connected to hydraulic actuators, which were saturated with water prior to each centrifuge test. Prop installation was simulated by locking hydraulic actuators. Figure 6.3 illustrates the method for simulating prop installation in this present study. It can be seen that outlet of the low-friction actuator is connected to an on/off value. Prior to prop installation, the on/off value is held in the open position, such that the prop connected to the low-friction actuator can slide freely with the inward movement of wall due to excavation. Whenever there is a need for prop installation, the on/off value is turned off to hold the prop in position.

Water tables of the clay layer and the underlying aquifer were controlled individually by two water reservoirs. Control of water table in the centrifuge test is presented later.

6.5.1 Actuator: For Simulating Prop Installation

Plate 6.2 shows an experimental package consisting of two levels of hydraulic actuators (two in each level) and model prop connected to each actuator. One load cell is installed between each actuator and prop to measure prop load. For centrifuge

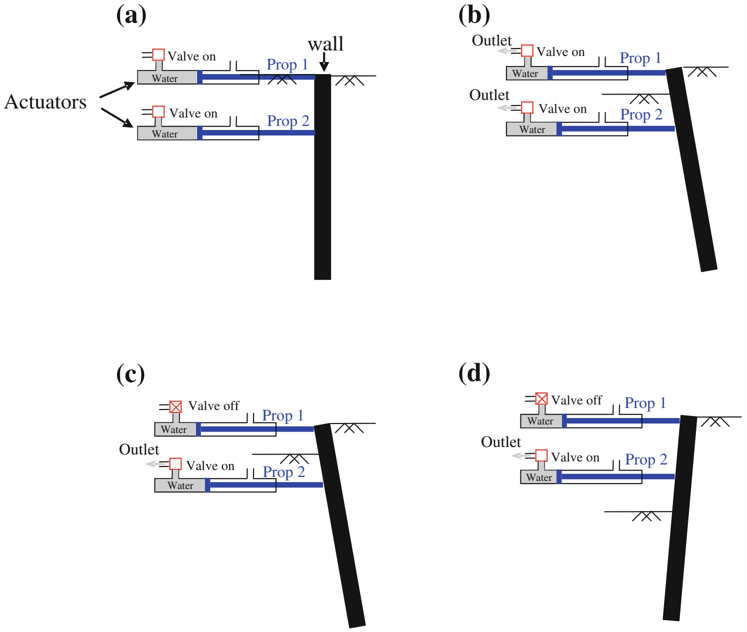

Fig. 6.3 Simulation of in-flight propping. **a** Before excavation. **b** Excavation with props 1 and 2 free to slide. **c** Lock prop 1 in place. **d** Excavation with prop 1 locked and prop 2 free to slide

Plate 6.2 Experimental setup for simulating in-flight propping

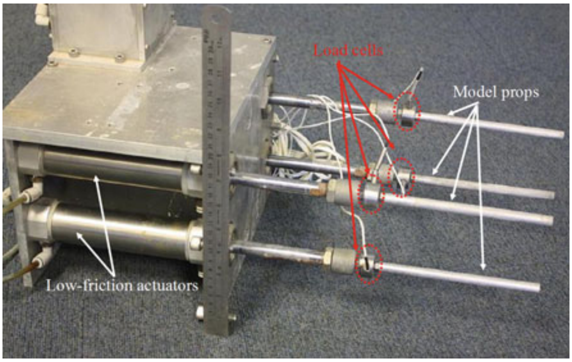

tests in this present study, twin-propped excavations are simulated. Elevations of the two levels of props are located at the crest of the wall and middle depth of excavation, respectively. To mininise passive resistance due to friction of the rod inside actuator, a type of low-friction hydraulic actuator was selected. Based on measurement from trial tests at 1 and 50 g, it is shown that frictional force of the actuator itself counts for no more than 5 % of the total axial load acting on the prop.

6.5.2 *Rubber Bag: For Simulating Excavation*

As presented, in-flight excavation in this present study is simulated by draining away zinc chloride (in a rubber bag) with equivalent density of soil to be excavated. One major challenge for manufacturing the rubber bag for this present study is: cylindrical holes should be made in the rubber bag for model props to get through, while any leakage of the rubber bag should be prevented. To meet these specific requirements, two moulds were manufactured for shaping different components of the rubber bag using silicon rubber. Plate 6.3a shows one mould for manufacturing inner tubes (to be installed inside rubber bag), from which model props would get through. After producing the four inner tubes, they are place in another mould (Plate 6.3b). Together with the pre-manufactured inner tubes and fresh silicon fluid (mixed with rubber coagulant) filled within gaps inside the mould, a final product of rubber bag is produced. Plate 6.4a, b show elevation view and plan view of the manufactured rubber bag, respectively.

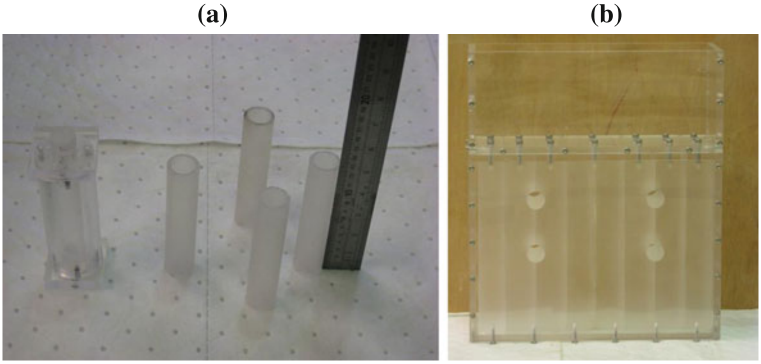

Plate 6.3 Moulds for manufacturing **a** inner tube of rubber bag; **b** outer rubber bag

Plate 6.4 A manufactured rubber bag. **a** Elevation view. **b** Plan view

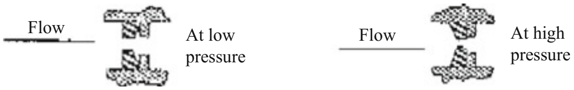

Fig. 6.4 Working principle of flow rate control valve

6.5.3 Flow Rate Control Valve: Controlling Excavation Rate

It is well recongnised that drainage rate of zinc chloride fluid at 50 g is highly nonlinear, due to reduced head difference during drainage. To ensure a constant drainage rate (i.e., excavation rate) during the in-flight simulation, a flow rate control valve (Plate 6.5) is adopted and connected to rubber bag. Figure 6.4 illustrates working principle of the flow rate control valve. The flow rate control valve contains a flexible orifice, which varies its effective area inversely to the applied pressure. As the applied pressure increases, the inset of the flexible orifice begins to distort and reduce the orifice area to maintain a desired flow rate. Working pressure of the flow rate control valve is in the range of 20–500 kPa. Based on calibration, it is found that the resulted flow rate by using this valve varies within ±15 %.

6.5.4 Model Wall

The model wall (Plate 6.6a) is made of aluminum alloy with Young's modulus equal to 72 GPa and yield strength of 241 MPa. The thickness of the wall can be converted to prototype scale by matching the bending stiffness of the wall. According to scaling law, the relationship between the model thickness and the prototype thickness of the wall is:

$$E_m I_m = N^{-3} E_p I_p \tag{6.10}$$

where N denotes the g level; E_m and E_p denote the Young' modulus of the wall in model scale and in prototype, respectively; I_m and I_p denote the second moment of

Plate 6.5 Flow rate control valve

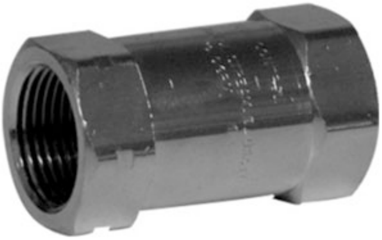

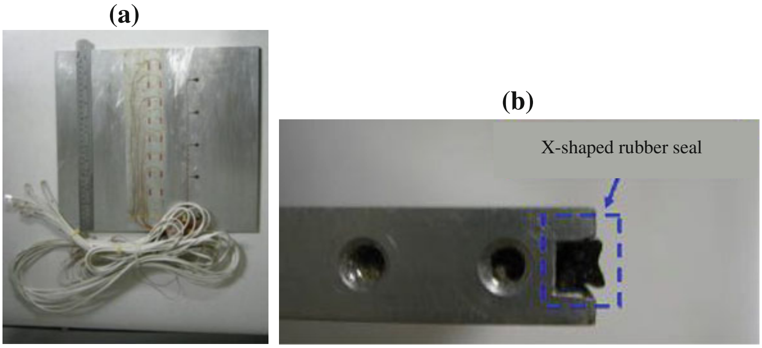

Plate 6.6 **a** Model wall. **b** Greased rubber seal for minimising friction and preventing water flow between wall and model box

area per unit length of the wall in model scale and prototype scale, respectively. Based on Eq. (6.10), the 10-mm thick aluminum alloy model wall, at an acceleration of 50 g is equal to a 600-mm thick reinforcement concrete diaphragm wall (Young's modulus of concrete is assumed to be 20 MPa).

As shown in Plate 6.6b, greased rubber seals were used to prevent water from seeping past the sides of the wall and to ensure a free sliding condition with minimal friction.

6.5.5 Model Prop

Each model prop (Plate 6.2) is also made of aluminium alloy. Overall axial stiffness of the actuator-prop system is about 10×10^6 N/m in prototype (i.e., 200 N/mm in model scale), measured by axial load-displacement tests in a loading rig. This prop stiffness is one-third of that in a typical excavation in London clay (i.e., 30×10^6 N/m, Mcnamara (2001)). According to Lam (2010), props with stiffness lower than 30×10^6 N/m (in prototype) can be classified as soft prop. In each reported centrifuge test, vertical and horizontal spacings for props are 4 and 8.75 m (in prototype), respectively.

6.5.6 Model Pile

Each model pile (Plate 6.7) is modelled by an aluminium tube with an outer diameter and thickness of 20 mm and 1.5 m, respectively. An epoxy coating of about 1.5-mm thick is applied to provide waterproof for strain gauges instrumented along the pile shaft. Each pile is anticipated to take both axial load (due to ground

Plate 6.7 Model pile

heave) and bending moment (due to lateral soil movement) in the centrifuge test. It is well recognised that different scaling laws should be applied for axial stiffness (i.e., 1:N^2 for *EA*, where *N* denotes *g* level) and bending stiffness (i.e., 1:N^4 for *EI*). Each model pile is approximately equivalent to an axially loaded cylindrical reinforced concrete (RC) pile with an outer diameter of 1 m and thickness of 0.05 m, or a solid cylindrical RC pile subjected to lateral soil movement with a diameter of 1 m in prototype.

6.6 Model Preparation and Characterisation of Undrained Shear Strength of Clay

Model preparation and characterisation of undrained shear strength of clay described in this section are applicable for both tests C_0.4 and C_0.4P, with exception of pile installation (only for test C_0.4P).

For centrifuge tests conducted with saturated soil, it is essential to prevent leakage from model box during testing. Prior to preparation of soil model, joint between each side wall of the model box was carefully sealed with silicon rubber. Then the model box was filled with water to confirm water-proof of the silicon rubber. Plate 6.8a shows a sealed model box ready for preparation of soil model. Both bottom drainage and boundary drainages were installed inside the model box (Plate 6.8b), to provide drainage boundary for soil model and shorten drainage path of clay (and hence consolidation time), respectively.

To simulate the underlying aquifer, a sandy layer was formed by raining Toyoura sand from a sand hopper (Plate 6.9) into the model box. During sand raining (see Plate 6.10), a constant falling height of sand (i.e., 500 mm, based on previous calibration) was controlled in order to result in medium dense sand. The resulted relative density of sandy layer in tests C_0.4 and C_0.4P is 57 and 60 %, respectively. The sandy layer was saturated by connecting bottom drainage system

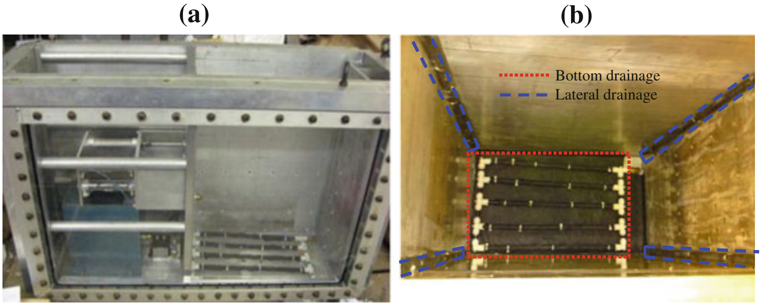

Plate 6.8 **a** Model box. **b** Bottom drainage and lateral drainages inside the mode box

Plate 6.9 Sand hopper

Plate 6.10 Raining sand into the model box

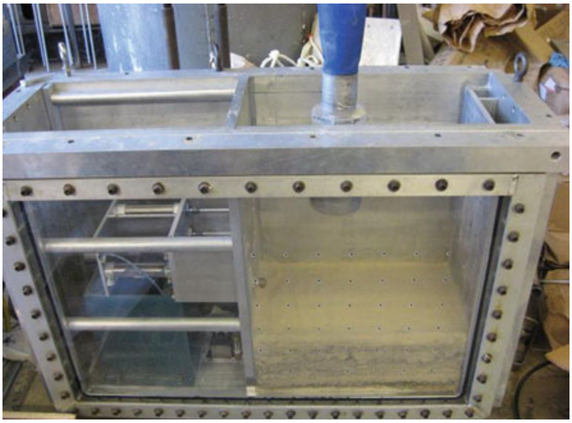

in the model box (Plate 6.8b) to a water reservoir, in which the water head was maintained at the level equal to the top of the sandy layer.

The clay layer was modeled using Speswhite China kaolin (Plate 6.11a). The kaolin powder was mixed in a mixer (Plate 6.11b) at an initial moisture content of

Plate 6.11 **a** Speswhite China clay. **b** Mixer for preparation of clay slurry

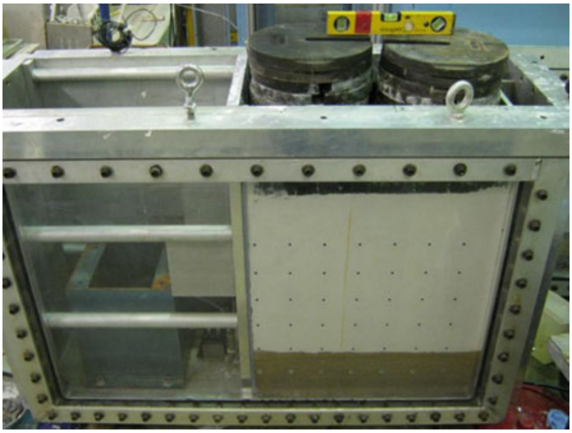

Plate 6.12 One-dimensional consolidation of clay at 1 g

120 % (about twice of the liquid limit of kaolin) with de-ionised water. The mixing process was conducted under vacuum for about 4 h. Prior to pouring the clay slurry into the model box, the inner surface of the model box was coated with silicon grease to minimise the friction between the clay and the model box. The frictional coefficient at the clay-grease interface was measured to be in the range of 0.01–0.02 by direct shear tests (Powrie 1986). After the clay slurry was placed carefully into the model box, one dimensional consolidation at 1 g was carried out, by applying vertical loadings on the top of the clay surface (Plate 6.12). Six loading steps were adopted, i.e. 1, 5, 10, 15, 30 and 50 kPa. Upon completion of 1 g consolidation, the average undrained shear strength was estimated to be 6 kPa (based on an empirical correlation proposed by Mesri (1989)), which was too soft to be cut and installed with model wall, model piles and pore water pressure transducers.

Therefore, consolidation at 50 g was carried out to increase strength of clay. Plate 6.13 shows the model box sitting on the platform of the centrifuge, prior to consolidation at 50 g. A T-bar penetrometer (Stewart and Randolph 1991) was installed on top of the model box for in-flight characterisation of undrained shear strength.

Plate 6.13 Clay bed before consolidation at 50 g

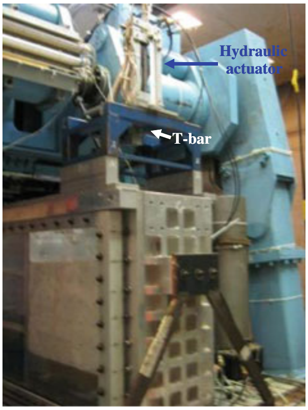

Upon completion of primary consolidation of clay at 50 g (i.e., reaching a 90 % degree of consolidation, as estimated by Tan (1991)'s method), the difference between measured consolidation settlement in tests C_0.4 and C_0.4P is about 7 %. This implies that clay samples prepared in these two tests are probably comparable.

Subsequently, the undrained shear strength profile of the clay layer was measured in-flight with T-bar penetrometer, which was driven by a hydraulic actuator. Penetration rate of the T-bar penetrometer was 1 mm/s, which was sufficiently fast to ensure undrained shearing in kaolin clay (Randolph and Hope 2004). Measured average c_u of clay is about 21 kPa (detailed in Chap. 8).

After unloading from 50 g consolidation (Plate 6.14), the clay with greatly increased undrained shear strength (i.e., increased by more than 3 times) was cut into the required profile (Plate 6.15) and installed with experimental components (i.e., rubber bag, model wall and model piles) and transducers (i.e., pore water pressure transducer).

Plate 6.14 Clay bed after consolidation at 50 g

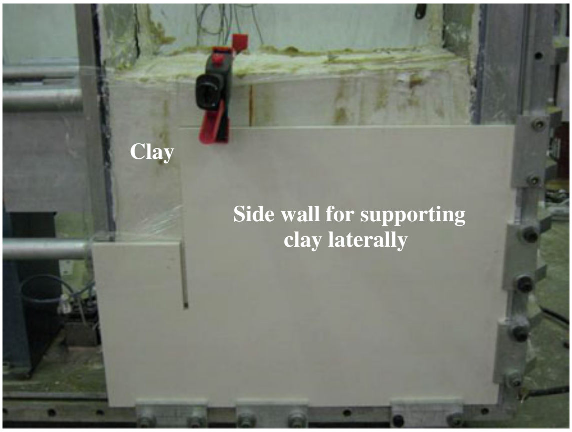

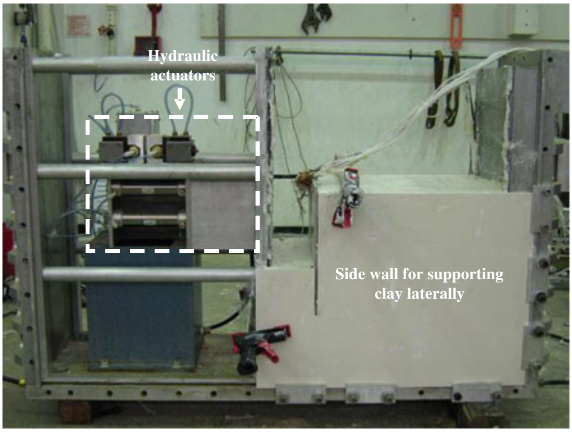

Plate 6.15 Cutting the consolidated clay bed into required profile

Piles were installed at 1 g (for test C_0.4P only). A mounting frame was used as guidance for an auger (Plate 6.16a) to drill holes through clay into the sandy aquifer, to create bored holes in the soil model before pile installation. Then each pile was installed into the pre-drilled hole (Plate 6.16b). Apart from use of guidance frame, verticality of each pile was checked by a level placed on top of each pile. Grains of black-dyed toyoura sand were then blown onto the clay to provide PIV texture (Plate 6.17). Actuators and rubber bag were also installed. Lubricant (vacuum grease) was then applied to the Perspex window to reduce friction against the soil cross-section. The hollow frame, perspex window and window frame were

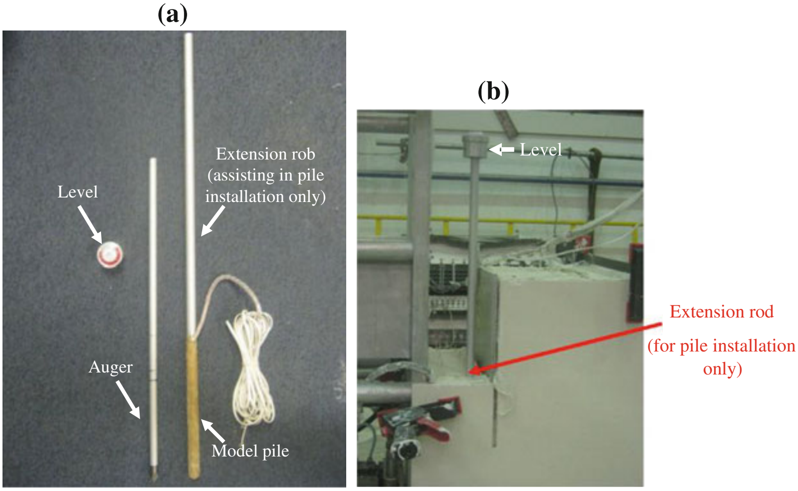

Plate 6.16 **a** Model pile and auger for pre-drilling. **b** Installing pile through clay into sandy aquifer

Plate 6.17 Installing rubber bag, model wall and spraying black sand on clay to provide texture for PIV analysis

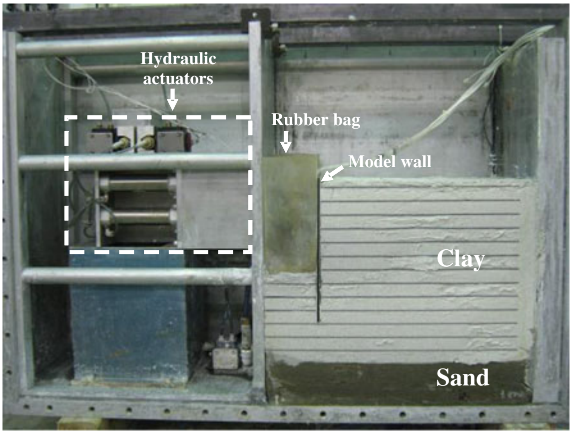

Plate 6.18 Shifting model box to the centrifuge, with digital cameras and videos installed in front of the perspex window

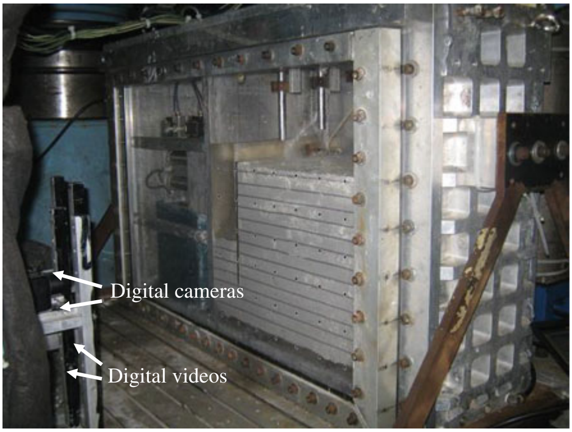

then bolted to the main body of the model box. Finally, the model box was shift to the platform of the centrifuge again, with two cameras and videos installed in front of the perspex window (Plate 6.18).

6.7 Instrumentation

Figure 6.5 shows instrumentation in a typical centrifuge test (test C_0.4P). Details of each instrument adopted are described as follows.

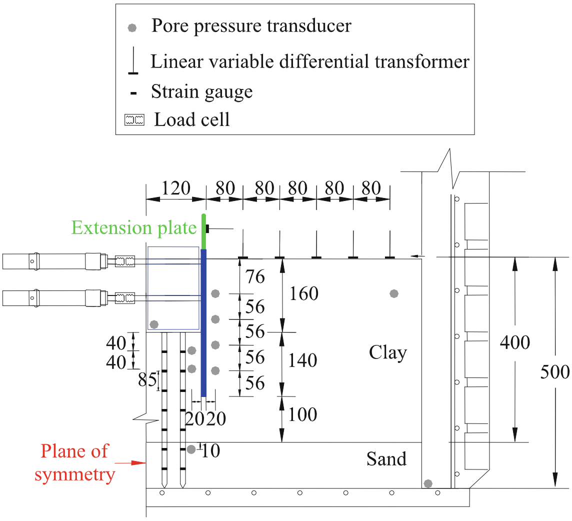

Fig. 6.5 Instrumentation in a typical centrifuge test (test C_0.4P)

6.7.1 *Measurement of Pore Water Pressure*

Change of pore water pressure in clay and sand is measured by druck PDCR-81 miniature pore water pressure transducer (i.e., PPT, Plate 6.19a). Porous filter of each PPT was saturated and the transducers were calibrated before use. When a PPT is subjected to a negative pore-water pressure, air bubbles inside the porous filter

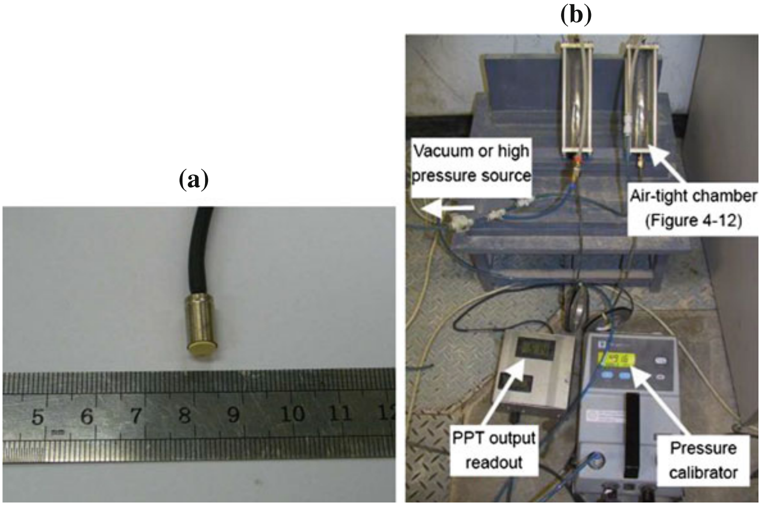

Plate 6.19 **a** Pore water pressure transducer (PPT). **b** Calibration of PPT

may expand, and might possibly touch the diaphragm. If this happened, deflection of the diaphragm may be affected by the air pressure inside the bubble, and would no longer be representative of pore-water pressure outside the PPT. As a rigorous saturation procedure was required.

Experience showed that PPTs used could be de-saturated at very small matric suction. As a result, porous filters of some PPTs were replaced with a 5-bar air-entry value disk so as to prevent entry of air at a matric suction below 500 kPa. The subsequent procedure was in essence initial saturation and pre-pressurization cycles discussed in Take and Bolton (2003). Practical details are as follows: The PPT was dried in an oven at about 55°C for 24 h so that water (with its dissolved air) in the porous filter was removed first. The PPT was then placed in a cylindrical chamber (Plate 6.19b). About one-third of the chamber was filled with water. The chamber was designed so that when it is placed horizontally, the PPT would not be in contact with the water inside the chamber. A vacuum pressure of not less than 98 kPa was first applied to the chamber to de-air the water. After one hour, the chamber was rotated by about 45° so that (then de-aired) water may slowly flow into the porous filter. Vacuum was continuously applied for another hour.

After that, the vacuum was turned off and a pore pressure of 490–500 kPa was applied in the chamber. Then, vacuum was applied again. An excitation voltage of 5 V was applied to the PPT and it was observed that at least three cycles were needed to ensure that output of PPT responded almost immediately with changes in pore pressure. As a conservative measure, seven cycles of saturation were carried out for each PPT.

6.7.2 Measurement of Ground Settlement

Ground surface settlement is measured by linear variable differential transformers (LVDTs, see Plate 6.20a). The coupling between the primary and the secondary coil depends on the position of the movable ferromagnetic core. The displacement

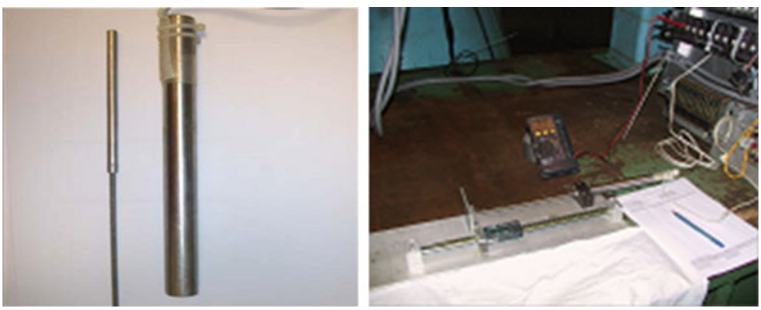

Plate 6.20 **a** Linear variable differential transformer (LVDT). **b** Calibration of LVDT

measured by LVDTs is outputted as voltage. The relationship between the displacement and the output signal could be obtained by calibration (Plate 6.20b). The LVDTs were highly sensitive with a non-linearity range of 0.3 % of their rated stroke. Accuracy of each LVDT is within ±80 μm.

6.7.3 Measurement of Undrained Shear Strength of Clay

To measured undrained shear strength profile of clay in-flight, T-bar penetrometer is adopted (Plate 6.21a). The penetrometer consists of a crossbar (with a bar diameter of 5 mm and a length of 20 mm in model scale) on the bottom. The crossbar is connected to a long, cylindrical shaft on top. Immediately above the crossbar, a full Wheatstone bridge of strain gauges is installed. The working principle of a T-bar penetrometer is discussed in detail by Stewart and Randolph (1991). Pressure on the T-bar may be correlated to undrained shear strength of clay using a plastic solution (Randolph and Houlsby 1984) and an empirical factor (bar factor). By jacking the T-bar into clay, a continuous undrained shear strength profile against depth can be obtained. Vertical displacement of T-bar could be controlled by a hydraulic actuator combined with a closed-loop control system. The T-bar was calibrated by applying axial load with a load rig, as shown by Plate 6.21b. It is loaded with known forces read from proving ring. The proving ring has a calibration certificate with relationship between force and deformation given.

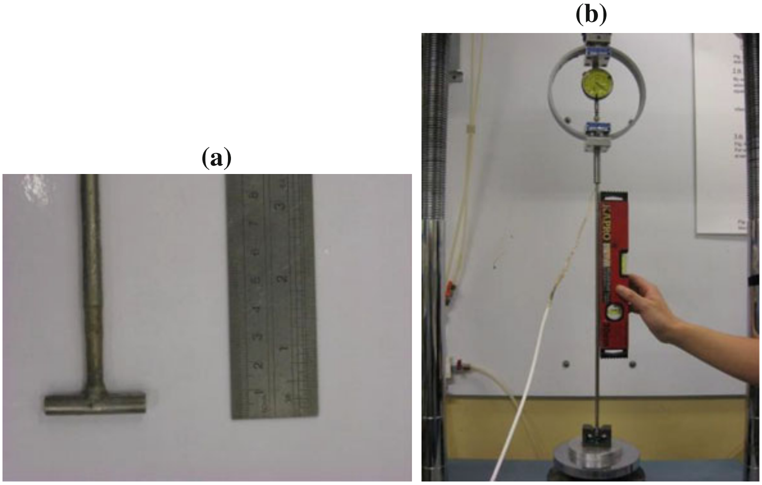

Plate 6.21 **a** T-bar penetrometer. **b** Calibration of T-bar penetrometer

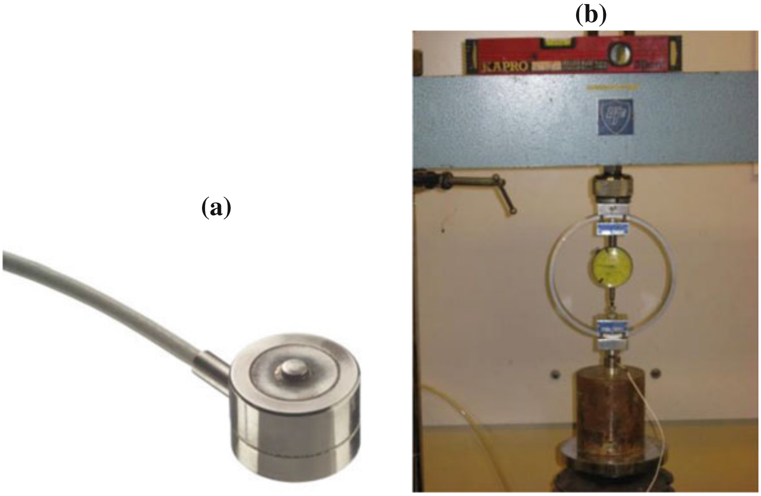

Plate 6.22 **a** Load cell; **b** calibration of load cell

6.7.4 Measurement of Prop Load

During the test, load cell (Plate 6.22a) with capacity of 500 N was used to measured prop load. Each load cell was manufactured by Entran Devices, Inc. with serial number of ELHS-T1 M-500 N. Calibration of each load cell was the same as that of T-bar penetrometer, i.e., loaded axially with a load rig (Plate 6.22b).

6.7.5 Measurement of Bending Movement and Axial Load of Pile

Bending moment and axial load in each pile are measured by strain gauges (Plate 6.7). At each measuring point, a full Wheatstone bridge of strain gauges is installed to minimise temperature effect on strain gauge reading. The strain gauges are protected by an epoxy coating to prevent possible mal-functioning due to moisture in the saturated soils.

As illustrated in Plate 6.23a, strain gauges for axial load measurement are calibrated using a load rig. The calibration procedures are the same as that for T-bar and load cell. To calibrate strain gauges for measurement of bending moment, the pile is fixed by pinned support at one end and loaded at end other end (i.e., working as a cantilever beam, see Plate 6.23b). By correlating output voltage and known bending moment at each level, calibration factor of each Wheatstone bridge of strain gauges can be obtained.

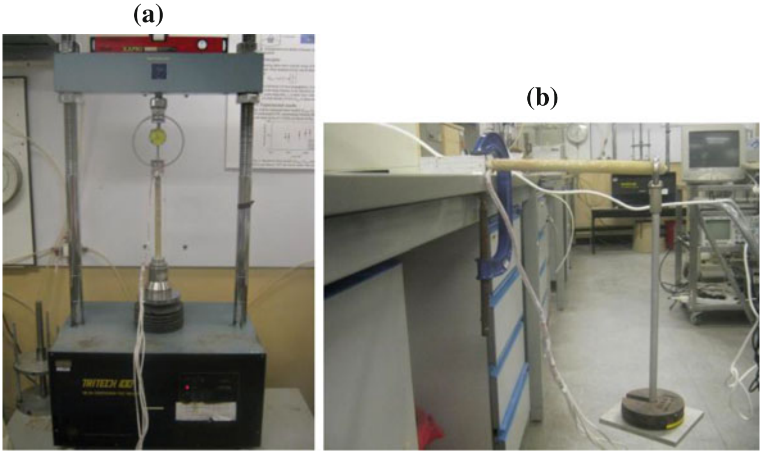

Plate 6.23 Calibration of strain gauges: **a** Axial load; **b** bending moment

6.7.6 Measurement of Subsurface Soil Movement

PIV is a deformation measurement system based on particle image velocimetry technical coupled with close-range photogrammetry correction (White et al. 2003). It makes use of digital photography to capture images of planar soil deformations. Figure 6.6 shows basic principle of PIV analysis, which works by tracking the texture (i.e. the spatial variation of brightness) within an image of soil through a series of images. The initial image is divided into a mesh of PIV test patches. Consider a single test patch, located at coordinates (u_1, v_1) in Image 1. To find the displaced location of this patch in a subsequent image, the following operation is carried out. The correlation between the patch extracted from Image 1 (time = t_1) and a larger patch from the same part of image 2 (time = t_2) is evaluated. The location at which the highest correlation is found indicates the displaced position of the patch (u_2, v_2). The location of the correlation peak is established to sub-pixel precision by fitting a bi-cubic interpolation around the highest integer peak. This operation is repeated for the entire mesh of patches within the image, and then repeated for each image within the series, to produce complete trajectories of each test patch.

It is worth noting that PIV is only capable of measuring soil displacement in image-space coordinates. Displacements are expressed in the unit of pixels of the image. To understand ground deformation mechanisms, displacements in terms of object-space coordinates are of interest. Displacements in image-space are not linearly related to displacements in object-space. Instead, these coordinate systems are related by a set of physical laws in close-range photogrammetry. These physical laws in optics are governed by a total of 16 parameters, which characterises (a) non-coplanarity of CCD and object plane, (b) lens distortion, (c) refraction of

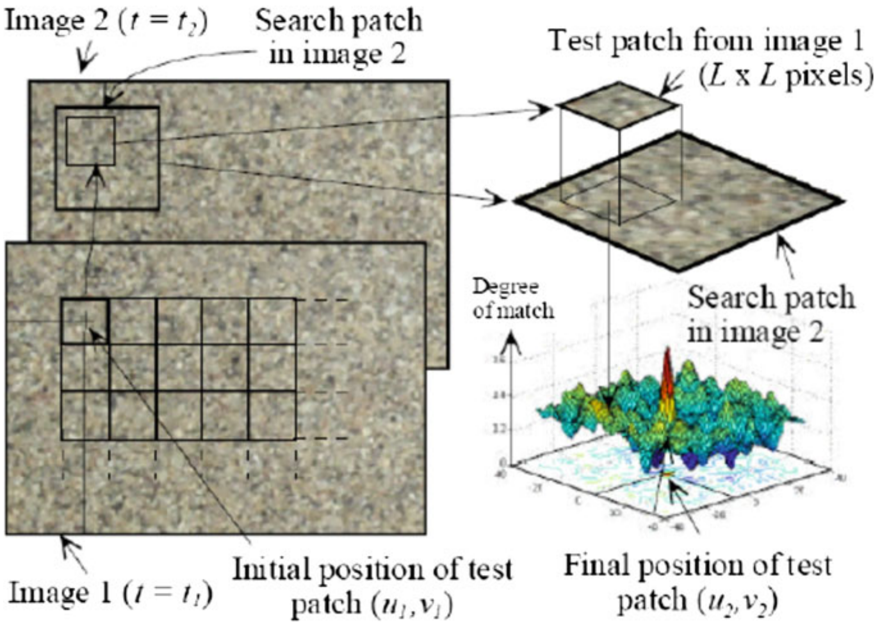

Fig. 6.6 Basic principle of PIV analysis (White et al. 2003)

Perspex window, (d) CCD pixel non-squareness and (e) focal length and principal point. With these 16 parameters, displacement vectors in terms of image-space coordinates obtained from PIV are converted to displacement vectors in terms of object-space coordinates. Figure 6.7 shows a flow chart illustrating procedures of PIV analysis. More details are given by White et al. (2003).

Since lens of a camera may deform slightly during a centrifuge test due to increased gravity, some of these 16 parameters may also be different among images taken during a test. As a result, conversion of image-space coordinates to object-space coordinates of each image must be carried out separately. The 16 parameters for the conversion are obtained from back-calculation using known image-space coordinates of centroid of each control marker and their pre-determined object-space coordinates. Object-space coordinates of control markers are, in turn, calibrated by using known image-space coordinates and object-space coordinates of a grid of reference targets prior to the experiment.

In the present study, five-million pixel digital cameras were installed in front of the model box (Plate 6.18). Digital images were taken every 30 s (model scale) through the transparent Perspex window of the strongbox. These digital cameras were controlled remotely by computers installed near the centre of the centrifuge through universal serial bus (USB) cables and the cameras were powered by an AC source. Since these computers rotate with the centrifuge, they were remotely controlled in the Control Room via wireless LAN using Remote Desktop in Windows system.

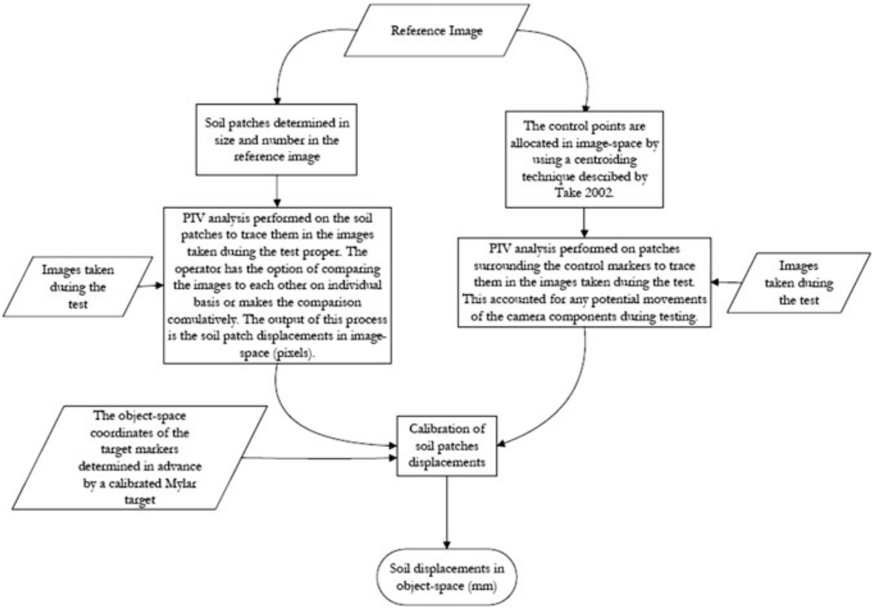

Fig. 6.7 A flow chart showing procedures of PIV analysis

6.8 Test Procedure

On completion of reconsolidation at 50 g (i.e., with a degree of consolidation >90 %), in-flight excavation was simulated by draining away zinc chloride fluid in a rubber bag. The drainage rate was maintained constantly by a flow rate control valve to simulate a constant excavation rate, which was equivalent to 0.6 m deep per day (in prototype). The modelled excavation rate is generally comparable to that of the case history studied herein (0.4 m deep per day, see Chap. 4). The 8 m deep excavation (in prototype) was conducted by three stages. Target levels for each excavation stage are 1, 5 and 8 m below ground surface (in prototype), respectively. Each excavation stage was followed by prop installation, except the last excavation stage. Each level of props was installed 1 m above the bottom of the previous excavation stage.

Immediately after excavation, artesian pressure in the sand aquifer was increased step by step to destabilise the excavation. It is intentionally to simulate excavation and hydraulic uplift separately so as to differentiate the two effects on the excavation base instability. Table 6.2 summarises detailed centrifuge modelling procedures. In the table, the stability factor associated with hydraulic uplift N_{c_HU} is defined as:

Table 6.2 Centrifuge modelling procedure (numbers in parenthesis denote model scale)

Stage		Modelling activity	Duration
Reconsolidation	REC	Reconsolidation at 50 g	11.5 yr (40 h)
Multi-stage excavation	EXC1(a)	Excavate to −1 m (−0.02 m)	1.7 d (60 s)
	EXC1(b)	Install prop 1 at 0 m (0 m)	0.15 d (5 s)
	EXC2(a)	Excavate to −5 m (−0.1 m)	6.9 d (240 s)
	EXC2(b)	Install prop 2 at −4 m (−0.08 m)	0.15 d (5 s)
	EXC3	Excavate to −8 m (−0.16 m)	5.2 d (180 s)
Hydraulic uplift	HU1	Apply artesian pressure to N_{c_HU} = 0.90	0.9 d (30 s)
	HU2	Increase artesian pressure to N_{c_HU} = 1.05	0.9 d (30 s)
	HU3	Increase artesian pressure to N_{c_HU} = 1.10	0.9 d (30 s)
	HU4	Increase artesian pressure to N_{c_HU} = 1.15	0.9 d (30 s)
	HU5	Increase artesian pressure to N_{c_HU} = 1.20	0.9 d (30 s)
	HU6	Increase artesian pressure to N_{c_HU} = 1.25*	0.9 d (30 s)

*In both tests C_0.4 and C_0.4P, ultimate state of hydraulic uplift was achieved when N_{c_HU} was increased to about 1.22

$$N_{c\_HU} = P_a/(\gamma_{clay}D) \tag{6.11}$$

where P_a denotes the artisan pressure acting on the bottom of the clay layer; γ_{clay} denotes bulk density of clay and D refers to thickness of clay inside excavation. The inverse of N_{c_HU} is corresponding to the conventionally defined factor of safety against hydraulic uplift FOS_{uplift} (Harr 1962).

During the entire process of centrifuge modelling, water table of the clay layer is maintained at the ground surface. In the sandy aquifer, water table varies with testing procedures. During spinning up of the model and reconsolidation of clay, water table of the sandy aquifer is maintained at the ground surface. During excavation, water table of the sandy aquifer is not specified. Its water table changes freely as internal drainage occurs. During the subsequent hydraulic uplift, water table of the sandy aquifer is increased step by step according to predefined artesian pressure (Table 6.2).

References

Fuglsang LD, Ovesen NK (1988) The theory of modelling to centrifuge studies, centrifuge in soil mechanics. Balkema, Rotterdam

Harr ME (1962) Groundwater and seepage. McGraw-Hill Book Company, New York

Lam SY (2010) Ground movements due to excavation in clay: physical and analytical models. PhD thesis, University of Cambridge, UK

Mair RJ (1979) Centrifugal modelling of tunnel construction in soft clay. PhD thesis, University of Cambridge, UK

Mcnamara MA (2001) Influence of heave reducing piles on ground movements around excavations. Ph.D thesis, City University of London, UK

Mesri G (1989) A reevaluation of $c_u = 0.22\sigma'_v$ using laboratory shear tests. Can Geotech J 26 (1):162–164

Powrie W (1986) The behaviour of diaphragm walls in clay. PhD thesis, University of Cambridge, UK

Randolph MF, Houlsby GT (1984) The limiting pressure on a circular pile loaded laterally in cohesive soil. Géotechnique 34(4):613–623

Randolph MF, Hope S (2004) Effect of cone velocity on cone resistance and excess pore pressures. In: Proceedings of the international symposium engineering practice and performance of soft deposits, Osaka, pp 147–152

Stewart DP, Randolph MF (1991) A new site investigation tool for the centrifuge. In: Proceedings of the international conference on centrifuge modelling: centrifuge 91, Boulder, Colorado, pp 531–538

Tan TS, Inoue T, Lee SL (1991) Hyperbolic method for consolidation analysis. J Geotech Eng 117 (11):1723–1737

Take WA, Bolton MD (2003) Tensiometer saturation and the reliable measurement of soil suction. Géotechnique 53(2):159–172

White DJ, Take WA, Bolton MD (2003) Soil deformation measurement using particle image velocimetry (PIV) and photogrammetry. Géotechnique 53(7):619–631

Chapter 7
Finite Element Analyses: For Back-Analysis and Parametric Study

7.1 Introduction

The previous chapter describes centrifuge modelling of multi-propped excavation in soft clay destabilised by hydraulic uplift. As centrifuge tests in clay are rather time consuming and relatively costly, only limited numbers of centrifuge tests are carried out in this study. Systematical study on the initiation and failure mechanism of base instability due to hydraulic uplift relies on three-dimensional, coupled consolidation finite element analyses.

In this chapter, finite element analyses conducted for the following two chapters (i.e., Chaps. 8 and 9) are described, in terms of (a) finite element mesh and boundary conditions; (b) constitutive model and model parameters; (c) numerical modelling procedure.

Four types of analyses were carried out:

(1) numerical back-analyses of centrifuge tests, aiming at calibrating a constitutive model, model parameters and modelling procedures against measured data and obtaining better understanding of centrifuge tests;
(2) numerical parametric study of centrifuge tests, aiming at investigating influence of embedment depth of 'anti-uplift piles' on effectiveness of base stabilisation;
(3) numerical parametric study for investigating effects of key dimensionless groups (indentified in Chap. 5) on the initiation and failure mechanism of base instability due to hydraulic uplift;
(4) numerical analysis for verifying another proposed alternative method for base stabilisation (apart from 'anti-uplift pile', details are given in Chap. 9).

Y. Hong and L. Wang, *Deformation and Failure Mechanism of Excavation in Clay Subjected to Hydraulic Uplift*, Advanced Topics in Science and Technology in China, DOI 10.1007/978-3-662-46507-3_7

It is worth noting that in all four types of finite element analyses presented above, excavation and hydraulic uplift are simulated separately, in order to differentiate both effects on excavation base instability. It is understood that in practice, excavation is conducted with presence of hydraulic pressure. To examine the validity of the 'idealised modelling technique' adopted in this study, one additional numerical analysis with 'rigorous modelling technique' (excavation with presence of hydraulic pressure) was carried out. Computed results from 'idealised modelling technique' and 'rigorous modelling technique' are shown to be almost identical (presented in Chap. 8). Based on this validation, the 'idealised modelling technique' is adopted in all finite element analyses in this study.

7.2 Back-Analyses of Centrifuge Tests

7.2.1 Finite Element Mesh and Boundary Conditions

Figure 7.1a shows an isometric view of a typical finite element mesh (simulating the centrifuge test with piles (i.e., C_0.4P)). Only half of the centrifuge model was simulated because of the symmetrical nature of the problem with respected to plane *YZ* (Fig. 7.1a). All dimensions are in model scale and are identical to those in the centrifuge tests. Each lateral boundary of the mesh is fixed by roller supports while the bottom of the mesh is fixed by pinned supports. Water tables of the clay layer and the sandy aquifer are controlled the same as those in the centrifuge.

To simulate the presence of zinc chloride fluid, pressure was applied on the wall and the formation level of the excavation, as shown in Fig. 7.1b. The applied pressure is equivalent to the vertical and horizontal pressure of the zinc chloride fluid adopted in the centrifuge test. The drainage process of heavy fluid was

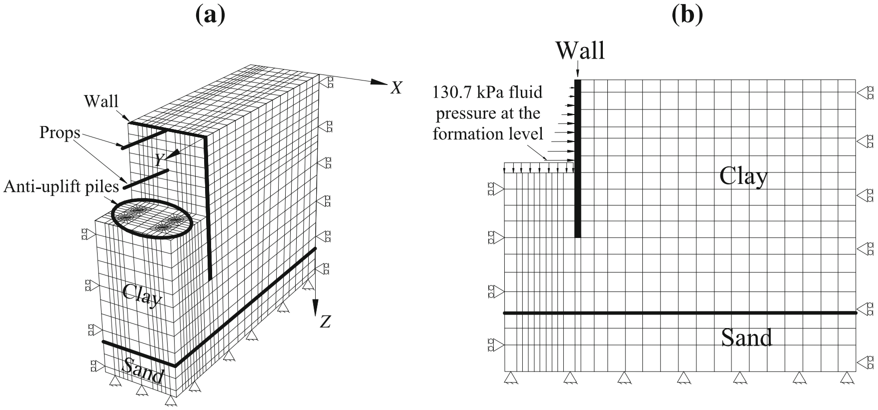

Fig. 7.1 Finite element mesh and boundary conditions simulating the excavation installed with piles (i.e., C_0.4P). **a** Isometric view. **b** Elevation view

simulated by decreasing the pressure acting on the wall and on the formation level of the excavation simultaneously.

Regarding the mesh size, a numerical test shows that further halving current mesh size (Fig. 7.1a, b) can only lead to a further convergence of no more than 0.2 %.

In back-analysis of the test without piles (i.e., C_0.4), finite element mesh and boundary conditions are the same as those shown in Fig. 7.1a, b, but no piles are modelled.

7.2.2 *Constitutive Model and Model Parameters*

Modified Cam clay (MCC) model is adopted to simulate the clay layer, since the majority of the clay bed is lightly overconsolidated. Table 7.1 summarises material parameters of kaolin clay adopted in the numerical analysis. All parameters are from literatures except initial void ratio, which is deduced from measured water content of clay sample before consolidation at 50 g. The sandy aquifer is modelled using an elasto-plastic model with Mohr–Coulomb failure criterion. Table 7.2 summarises material parameters of Toyoura sand adopted in the numerical analysis.

The soil-pile interface and soil-wall interface were modelled as zero thickness by using duplicated nodes (ABAQUS (Hibbitt et al. 2008)). The interface was modelled by the Coulomb friction law, in which interface friction coefficient (μ) and limiting displacement (γ_{lim}) are required as input parameters. The μ and γ_{lim} of epoxy-kaolin interface have been reported by Ng et al. (2008), based on numerical back-analyses of centrifuge tests on piles (coated by epoxy) in kaolin clay. Their back-analysed interface parameters (i.e., $\mu = 0.3$; $\gamma_{lim} = 5$ mm) are adopted in this study.

Table 7.1 Material parameters of kaolin clay adopted in the numerical analyses

Description	Parameter	Reference
Stress ratio: M	0.92	Stewart (1992)
Specific volume of the critical state line at unit pressure: Γ	3.48	Phillips (1987)
Slope of one-dimensional compression line in v-lnp' space: λ	0.25	Al-Tabbaa (1987)
Slope of unload-reload line in v-lnp' space: κ	0.05	Al-Tabbaa (1987)
Possion's ratio for effective stress analysis: μ'	0.33	Nadarajah (1973)
Critical state angle of shearing resistance: ϕ'_{cs}	22°	Powrie (1986)
Initial void ratio (at 1 g): e	1.71	Deduced from measured water content
Dry density (kN/m^3): γ_d	978	Deduced from void ratio
Coefficient of earth pressure at rest: K_o	0.63	Jacky (1944)
Saturated horizontal permeability (m/s): k_h	3.49×10^{9}	Al-Tabbaa and Wood (1987)
Saturated horizontal permeability (m/s): k_v	2.58×10^{9}	Al-Tabbaa and Wood (1987)

Table 7.2 Material parameters of Toyoura sand adopted in the numerical analyses

Description	Parameter	Reference
Effective angle of shearing resistance: ϕ'	31°	Ishihara (1993)
Angle of dilation: ψ'	5°	Bolton (1986)
Young's modulus for effective stress analysis: E'	50 MPa	Estimated
Initial void ratio (at 1 g): e	0.64	Deduced from measured average soil density
Dry density: kN/m^3	1616	Deduced from void ratio
Possion's ratio for effective stress analysis: μ'	0.17	Hicher and Chang (2006)
Coefficient of earth pressure at rest: K_o	0.50	Jacky (1944)
Saturated permeability: k	1.40×10^{4}	Ishihara (1993)

7.2.3 Numerical Modelling Procedure

Each centrifuge test conducted in this study consists of excavation, propping and hydraulic uplift. In the numerical analysis, excavation is simulated by ramp linearly deactivating soil elements on the excavated side. While excavation is reduced to each pre-determined level, prop elements are activated simultaneously. Hydraulic uplift is simulated by applied an increased surface pressure and a pore water pressure boundary (with pore water pressure increased in the same manner as the surface pressure) at the bottom of the clay layer. Increment of the surface and the pore water pressure in each modelling procedure is identical to that in the centrifuge tests. In each coupled consolidation analysis, numerical modelling procedure and duration are the same as those modelled in the centrifuge tests, as summarised in Table 6.2. It is worth noting that spinning up of soil model is simulated in each numerical analysis, by increasing gravitational acceleration of the whole model ramp linearly to 50 g.

7.3 Numerical Parametric Study

The calibrated numerical tool (i.e., constitutive model, its model parameters and numerical modelling procedure) is used to investigate embedment depth of 'anti-uplift piles' on effectiveness of base stabilisation, by carrying out numerical parametric study. In the parametric study, finite element mesh is identical to that for back-analysis (Fig. 7.1), except including an additional clay layer (30 m thick in prototype) underneath the existing sandy aquifer. 'Anti-uplift piles' are extended into the lower clay layer, with varied embedment depths (reasons explained in

Chap. 8). Diameter and spacing of piles in the parametric study are identical to those in the numerical back-analysis.

Moreover, the calibrated numerical tool is also used for parametric study to investigate effect of key variables on the initiation and failure mechanism of base instability due to hydraulic uplift (in Chap. 9). As suggested in Chap. 5, two key variables examined are excavation width and undrained shear strength of clay. Considering excavation width is varied in the parametric study, length of finite element mesh of the retained soil adopted in the back-analysis (Fig. 7.1) is extended to be 10 times of final excavation depth, to minimise boundary effect. In each analysis, the target undraintabled shear strength of clay is obtained by applying corresponding pre-consolidation pressure (determined based on trial-and-error) to the clay.

References

Al-Tabbaa A (1987) Permeability and stress-strain response of Speswhite kaolin. PhD thesis, University of Cambridge, UK

Al-Tabbaa A, Wood DM (1987) Some measurements of the permeability of kaolin. Géotechnique 37:499–503

Bolton MD (1986) The strength and dilatancy of sands. Géotechnique 36(1):65–78

Hibbitt, Karlsson and Sorensen Inc. (2008) ABAQUS User's Manual, version 6.8.2

Hicher PY, Chang C (2006) An isotropic nonlinear elastic model for particulate materials. J Geotech Geoenviron Eng 132(8):1052–1061

Ishihara K (1993) Liquefaction and flow failure during earthquakes. Géotechnique 43(3):351–415

Jacky J (1944) The coefficient of earth pressure at rest. J Soc Hung Archit Eng 7:355–358 (In Hungarian)

Nadarajah V (1973) Ground stress-strain properties of lightly over-consolidated clays. PhD thesis, University of Cambridge, UK

Ng CWW, Poulos HG, Chan VSH, Lam SY, Chan GCY (2008) Effects of tip location and shielding on piles in consolidating ground. J Geotech Geoenviron Eng 134(9):1245–1260

Phillips R (1987) Ground deformations in the vicinity of a trench heading. PhD thesis, University of Cambridge, UK

Powrie W (1986) The behaviour of diaphragm walls in clay. PhD thesis, University of Cambridge, UK

Stewart DP (1992) Lateral loading of piled bridge abutments due to embankment construction. PhD thesis, The University of Western Australia, Perth, Australia

Chapter 8

Interpretations of Measured and Back-Anlaysed Results of Centrifuge Tests

8.1 Introduction

This chapter reports and compares measured results of two centrifuge tests (as described in Chap. 6) and back-analysed results of the centrifuge tests by three-dimensional coupled-consolidation analyses (as described in Chap. 7). The physical and numerical investigation aim at studying (a) the initiation and failure mechanism of base instability due to hydraulic uplift; (b) base stabilisation effect of 'anti-uplift piles' installed inside excavation. Moreover, numerical parametric study was carried out to investigate effect of embedment depth of 'anti-uplift piles' on effectiveness of base stabilisation.

8.2 Interpretation of Measured and Computed Results

8.2.1 *Profiles of Over-Consolidation Ratio and At-Rest Lateral Earth Pressure Coefficient*

Figure 8.1a shows distribution of over-consolidation ratio (OCR) of clay with depth after the completion of reconsolidation. The *OCR* values are obtained by handy calculation based on known stress history of the clay layer at each elevation. As expected, *OCR* decreases with depth. The *OCR* profile suggests clay above −5 m is on the dry side of the critical state line ($OCR > 2$) and that below −5 m is on the wet side of the critical state line ($OCR < 2$). Based on the calculated OCR values and effective angle of shearing resistance (ϕ') of kaolin clay (reported in Chap. 7), at-rest earth pressure coefficient (K_o) of clay can be estimated using the commonly adopted empirical correlation as follows:

Y. Hong and L. Wang, *Deformation and Failure Mechanism of Excavation in Clay Subjected to Hydraulic Uplift*, Advanced Topics in Science and Technology in China, DOI 10.1007/978-3-662-46507-3_8

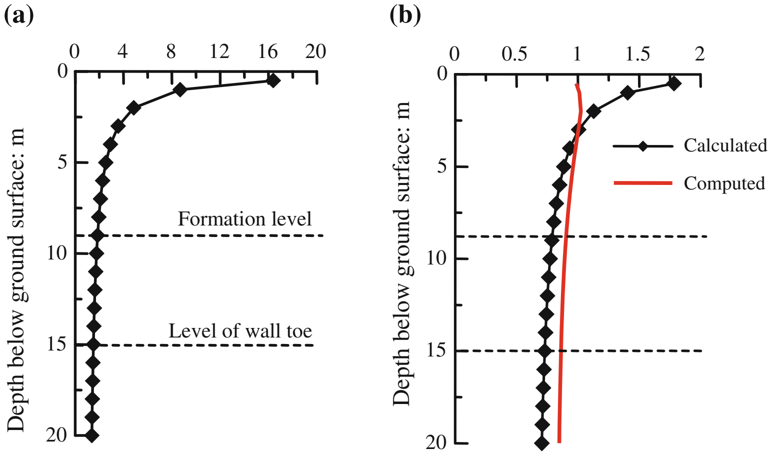

Fig. 8.1 **a** Over-consolidation ratio (OCR); **b** At-rest earth pressure coefficient (K_o) of clay after consolidation at 50 g

$$K_o = (1 - \sin\phi')OCR^{\sin\phi'} \tag{8.1}$$

Figure 8.1b shows estimated K_o values of clay with depth. Computed K_o profile is also included for comparison. The most significant difference between the estimated and computed K_o is near the ground surface (i.e., top 1 m), where the clay is heavily overconsolidated ($OCR > 8$, see Fig. 8.1a). It is generally recognised that that MCC model is not good at modelling heavily overconsolidated clay. Below −1 m, the difference between the estimated and computed K_o becomes smaller, with an average overestimation of 14 % by the computed results. Both estimated and computed results show that K_o of the clay is generally smaller than 1.0, except the clay above −3 m. This implies that horizontal earth pressure acting on the wall (on the retained side) could be smaller than that horizontal pressure of zinc chloride fluid (on the excavated side). Result of PIV analysis shows that due to reconsolidation of clay at 50 g, the model wall moved towards the retained side with a maximum lateral movement of about 1.8 mm (in model scale) at the wall top.

8.2.2 *Undrained Shear Strength Profile*

Figure 8.2 shows profiles of undrained shear strength (c_u) deduced from in-flight T-bar penetrometer tests. A constant T-bar factor of 10.5 was adopted to deduce the undrained shear strength, as suggested by Randolph and Houlsby (1984) from a plasticity analysis. It was reported by Barbosa-Cruz and Randolph (2005) that the actual T-bar factor increases from approximately 5 at the clay surface to 10.5 at a

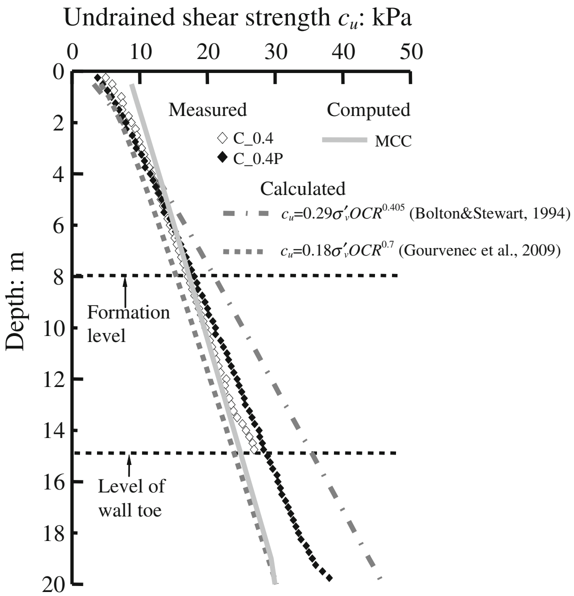

Fig. 8.2 Measured and computed undrained shear strength profile

penetration depth of 4–5 times of T-bar diameter (i.e., −1 m in prototype in this study). Therefore, the deduced strengths in the upper 1 m of clay are expected to be overestimated. In the same figure, calculated strength profiles based on two empirical correlations for kaolin clay (Bolton and Stewart 1994; Gourvenec et al. 2009) and computed strength profile by MCC are also included for comparisons.

It can be seen that the measured c_u profiles of clay samples in the two reported centrifuge tests (i.e., tests C_0.4 and C_0.4P) show a reasonable agreement, with a maximum difference of about 11 %. This implies clay samples in these two tests are likely to be comparable. The average c_u of clay between the formation level and level of wall toe (i.e., a key parameter to determine stability factor N_c, detailed in the subsequent section) is approximately 21 kPa. The measured c_u profiles are bounded by calculated strength profiles based on two empirical correlations for kaolin clay (Bolton and Stewart 1994; Gourvenec et al. 2009). Calculated strength profile based on the empirical correlation proposed by Gourvenec et al. (2009) is closer to the measured ones, than that calculated based on Bolton and Stewart (1994). This is expected as Gourvenec et al. (2009)'s empirical correlation was obtained by curve fitting c_u data in lightly overconsolidated clay (measured by in-flight T-bar penetrometer tests), while Bolton and Stewart (1994)'s empirical correlation was obtained by curve fitting c_u data of heavily overconsolidated clay (measured by triaxial tests). Comparison between measured and computed c_u profiles (by MCC) shows that near the ground surface (i.e., up to −2 m), where clay is heavily overconcolidated (i.e., $OCR > 4$, deduced based on known pre-consolidation pressure), the computed c_u overestimates the measured values significantly (i.e., about 40 %). It is well know that MCC is not suitable for modelling heavily overly consolidated clay. Below −5 m, where clay is lightly overconsolidated (i.e., $OCR < 2$, deduced), the computed c_u is much closer to the measured values, with a maximum difference of 10 %.

8.2.3 Lateral Wall Displacement

Figure 8.3 shows measured lateral wall displacement (δ_h, normalised by final excavation depth (H_e)) at various modelling stages in centrifuge tests with and without piles (i.e., tests C_0.4P and C_0.4, respectively). All presented data were measured by PIV analysis.

It is observed that upon commencement of excavation, the wall in both tests kept deforming in a cantilever manner even after props were installed at the crest of the wall (stage EXC2(a)). It was anticipated that after installing props, lateral movement near the crest of the wall would be restrained and the wall would deform in a 'deep-seated' profile. The measured cantilever type of wall movement suggests that stiffness of props adopted in these centrifuge tests may not be sufficient (as discussed in Chap. 6). At stage EXC2(a), the maximum lateral wall displacement ($\delta_{h\text{-}max}$) in the test with piles is 21 % smaller than that in the test without piles, due to stiffened ground on the excavated side. While the excavation reached approximately −6.5 m, the wall in the test without piles (test C_0.4) suddenly moved towards the excavation significantly. The incremental lateral wall displacement occurred at this stage consists of a translational movement (probably due to 'soft

Fig. 8.3 Measured lateral wall displacement

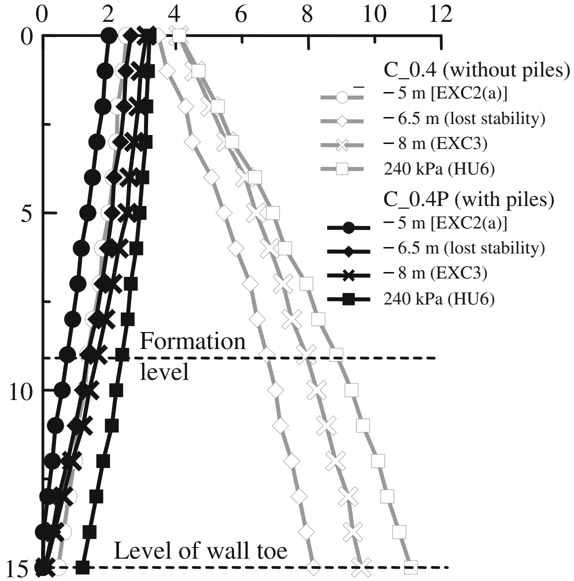

prop' effect) and a rotation with respect to the propped region (i.e., toe kick-out). The latter is a typical indication of base instability due to insufficient passive resistance in front of the wall.

To quantify the potential instability of this excavation, the stability factor due to excavation N_c (Bjerrum and Eide 1956) is calculated based on the following equation:

$$N_c = \gamma_{clay} h / c_u \tag{8.2}$$

where γ_{clay} and h are the bulk density of the clay and the excavation depth, respectively. c_u denotes average undrained shear strength of the clay between formation level and wall toe. Equation (8.2) implies that a larger stability factor N_c corresponds to a higher potential of base instability. In the test without piles installed (test C_0.4), when the excavation approached −6.5 m, the calculated stability factor N_c was 5.1 ($\gamma_{clay} = 16.3$ kN/m^3, $c_u = 20$ kPa). The N_c which triggers instability of excavation in the centrifuge test without piles (as deduced above) is close to the back-analysed N_c in this study (i.e., $N_c = 5.5$) and that computed by Poulos and Chen (1997) (i.e., $N_c = 5.0$). At the same stage in the test with piles installed (test C_0.4P), however, lateral movement at the wall toe was still well constrained. This indicates the excavation could have been stablilised due to presence of piles. Till the end of excavation (EXC3), deformed shape of wall in both tests with and without piles remains the same as that measured in the previous stage (i.e., −6.5 m) with a further 13 % and 19 % increase in $\delta_{h\text{-max}}$, respectively. Considering the maximum lateral wall movement ($\delta_{h\text{-max}}$) in the test with piles and without piles occurred at different locations (i.e., at the wall top and wall toe, respectively), it is not appropriate to compare these two directly. Instead, comparison is made between lateral wall displacements at the formation level ($\delta_{h\text{-}f}$) in the two tests. The comparison shows that by installing two rows of piles in front of the wall, $\delta_{h\text{-}f}$ has been reduced by 75 % at the end of excavation. During the subsequent hydraulic uplift (HU6), lateral movement at the wall toe in tests with and without piles increased (10 % and 33 %, respectively) due to the upward movement of clay inside the excavation induced in this stage (illustrated later).

8.2.4 Ground Deformation Mechanism Due to Excavation

Figure 8.4a, b compare measured incremental displacement vectors of clay (by PIV analysis) due to excavation in tests without and with piles (tests C_0.4 and C_0.4P), respectively.

It is illustrated in Fig. 8.4a that due to excavation in the test without piles, soil on the excavated side heaved upwards along a distinctive logspiral type sliding wedge. Horizontal inward movement of the soil increases with depth (up to wall toe), resulting in a kick-out at the wall toe (Fig. 8.3). This is likely to be induced by insufficient passive resistance in front of the wall, as indicated by high stability

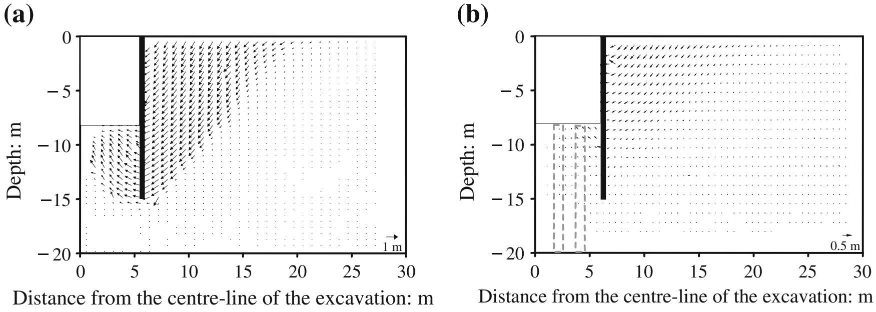

Fig. 8.4 Measured incremental displacement vectors due to excavation **a** in test C_0.4 (without piles); **b** in test C_0.4P (with piles)

factor ($N_c = 5$) of this excavation calculated in the previous section. By installing two rows of piles in front of the wall (Fig. 8.4b), sliding wedge type of soil movement on the excavated side was prevented. Opposite to the excavation without piles (Fig. 8.4a), horizontal inward movement of soil on the excavated side in the excavation with piles (Fig. 8.4b) decreases with depth. At the wall toe, horizontal movement in the excavation with piles is rather limited than that in the excavation without piles. Presence of piles could have increased passive resistance in front of the wall (evidence is given later) and hence stabilised excavation. Behind the wall, ground deformation mechanisms in the test with and without piles are also distinctive. In the test without piles (Fig. 8.4a), soil behind the wall moved downwards as a rigid body along a sliding wedge, which extended from the wall toe to the ground surface. This ground movement is compatible with toe kick-out of the wall (Fig. 8.3). In the excavation stabilised with piles (Fig. 8.4b), no sliding wedge was developed behind the wall. Soil movement maximised the crest of the wall decreased with depth. This ground deformation mechanism is compatible with the cantilever type of lateral wall movement (Fig. 8.3).

Due to the presence of the piles, the maximum lateral wall displacement at the formation level and the maximum ground settlement behind the wall ($\delta_{v\text{-max}}$) induced by excavation was 75 and 68 % smaller than that in the test without piles, respectively. Mcnamara (2001) carried out centrifuge tests to investigate 'strengthening effect' of piles (installed in front of the wall) on reduction of ground movements around excavation in stiff clay (with average c_u larger than 100 kPa). Each Pile modelled in the reported centrifuge tests is equivalent to a reinforced concrete pile with a diameter of 1 m in prototype (the same as that in this present study) and spacing between piles is $3d$ (in this study, pile spacings in two perpendicular directions are $2d$ and $4.4d$). As reported by Mcnamara (2001), presence of two rows of piles in front of the wall can lead to reductions in lateral wall displacement (near the formation level) and settlement behind the wall of 70 and 55 %, respectively. The reported percentage reductions of movement due to 'strengthening effect' of piles in stiff clay are less pronounced than those in soft clay reported herein (i.e., percentage reductions of $\delta_{h\text{-}f}$ and $\delta_{v\text{-max}}$ are 75 and 68 %, respectively). Compared to stiff clay, excavation in soft clay has less passive resistance such that piles in soft clay (in front of the wall) have to share more passive load from the soil. As a result, presence of piles in soft clay leads to a larger reduction of mobilised shear strength (and hence shear deformation) than that in stiff clay.

Figure 8.5a, b show computed incremental displacement vectors of clay due to excavation in tests without and with piles (tests C_0.4 and C_0.4P), respectively. In the test without piles, the most significant difference between measured (Fig. 8.4a) and computed (Fig. 8.5a) displacement vectors is influence area of rigid body movement behind the wall. This influence area is governed by inclined angle of sliding wedge behind the wall. It is generally well recongnised that a relatively simple elasto-plastic soil model (MCC in present study) may not be able to accurately capture strain localisation associated with failure of soil along sliding wedge (Poulos and Chen 1997). Apart from this aspect, computed ground deformation mechanism shows a general agreement with the measured one. In the test with piles, computed ground deformation mechanism (Fig. 8.5a) is similar to that measured in the centrifuge test (Fig. 8.4b).

Quantitatively, the differences between the measured and the computed $\delta_{h\text{-max}}$ and $\delta_{v\text{-max}}$ in tests with and without piles are no larger than 15 %. The measured $\delta_{h\text{-max}}$ in both tests are overestimated by the computed results. This can be due to many reasons, such as ignorance of strain dependency and stress path dependency of soil stiffness in MCC model. In the meantime, the measured $\delta_{v\text{-}max}$ in both tests are underestimated. It is well recognised that ignorance of strain dependency of soil in a constitutive model would result in an underestimation of $\delta_{v\text{-}max}$, because influence zone of settlement trough would be overestimated (Burland 1989; Ng and Lings 1995; Ng et al. 1998).

Reasonable agreement between measured and computed soil movement is important, as it increases confidence in computed soil strains. Computed incremental plastic deviatoric strain due to excavation in tests without and with piles is also included in Fig. 8.5a, b, respectively. In the test without piles (Fig. 8.5a), the most significant plastic strain of clay was mobilised along sliding wedge on both

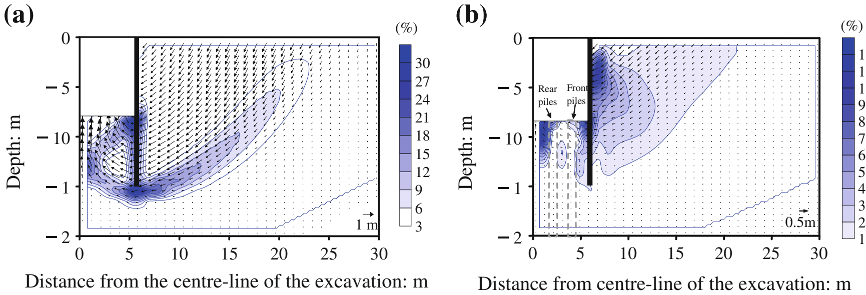

Fig. 8.5 Computed incremental displacement vectors due to excavation **a** in test C_0.4 (without piles); **b** in test C_0.4P (with piles)

sides of the wall and at soil-wall interface in front of the wall. In the test with piles (Fig. 8.5b), the most significant plastic strain of clay on the excavated side took place in front of the rear piles (near the pile head). This is because piles were subjected to lateral soil movement adjacent to the wall and deforms laterally (towards centre-line of the excavation), with a maximum lateral movement at the pile head. As a result, soil in front of rear piles was sheared due to lateral movement of the piles. Behind the wall, the most significant plastic strain was located near the crest of the wall, because the largest ground movement behind the wall took place near the wall top, as a result of cantilever-type wall movement (Fig. 8.3).

8.2.5 Ground Deformation Mechanism Due to Hydraulic Uplift

Immediately after excavation, pore water pressure (i.e., artesian pressure) in the sandy aquifer was increased step by step to destabilise the excavation. Figure 8.6a, b illustrate measured incremental displacement vectors of clay (by PIV analysis) due to hydraulic uplift in tests without and with piles (tests C_0.4 and C_0.4P), respectively. By applying artesian pressure at the bottom of clay in the test without piles (Fig. 8.6a), clay inside the excavation was uplifted while clay outside the excavation remained stationary. On the excavated side, clay located outside the pre-formed sliding wedge (due to the previous excavation) generally moved upwards vertically as a rigid body. Within the pre-formed sliding wedge, vertical upwards ground movement dominates while some horizontal ground movement is also included. The horizontal movement of clay is due to further lateral wall displacement during hydraulic uplift (Fig. 8.3). In the test with piles (Fig. 8.6b), clay inside the excavation moved upwards vertically as a rigid body. No distinguishable horizontal movement of clay can be observed. This is because further lateral wall

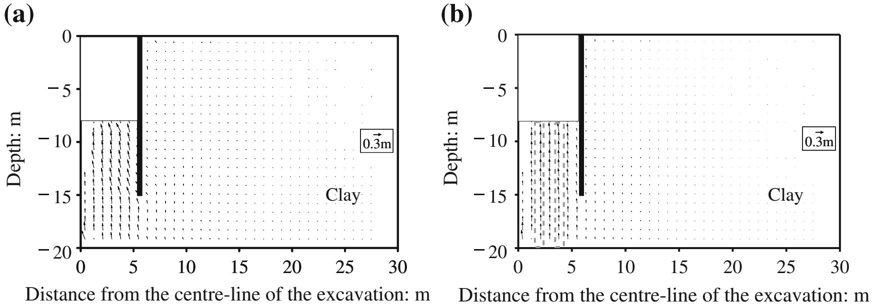

Fig. 8.6 Measured incremental displacement vectors due to hydraulic uplift **a** in test C_0.4 (without piles); **b** in test C_0.4P (with piles)

displacement during hydraulic uplift in this test is much less (i.e., 70 % less) than that in the test without piles (Fig. 8.3), due to 'strengthening effect' of piles. Comparison between Fig. 8.6a, b suggests that presence of piles does not help to reduce the ultimate uplift movements of clay inside the excavation. It is generally recognised that effectiveness of 'anti-uplift' piles is related to their pull-out resistance in deep stratum (i.e., sandy aquifer in this study). During hydraulic uplift, increased pore water pressure results in significant reduction of effective stress in the sandy aquifer (discussed in the subsequent section). Hence, shaft resistance (i.e., pull-out resistance) along piles in the sandy aquifer reduced significantly such that the 'anti-uplift' piles can be pull out from the sandy aquifer easily. Figure 8.7a, b show computed incremental displacement vectors for tests with and without piles due to hydraulic uplift, respectively. Computed results also show that uplift movement of clay inside excavation in the tests with and without piles is almost identical. This confirms that 'anti-uplift' piles can not work, if sandy aquifer is taken as the only bearing stratum to 'hold' the piles. Compared to measured ground deformation mechanism (Fig. 8.6a, b), the computed result (Fig. 8.7a, b) show a reasonable agreement.

To better understand failure mechanism of excavation subjected to hydraulic uplift, computed incremental plastic deviatoric strain is also included in Fig. 8.7a, b. In the excavation without piles (Fig. 8.7a), it can be seen that the most significant plastic strain was mobilised along the soil-wall interface and extended almost vertically downwards to the bottom of the clay. Shearing along the vertical plane should have been induced by relative movement between the uplifting clay inside the excavation and the stationary clay outside the excavation. Due to presence of piles in front of the wall (Fig. 8.7b), the 'intensive shearing zone' (where most significant plastic strain occurred) is only confined between wall and piles and its width becomes narrower than that in the excavation without piles. However, distribution of the 'intensive shearing zone' in the two cases is similar because of similar ground deformation mechanism of the two cases.

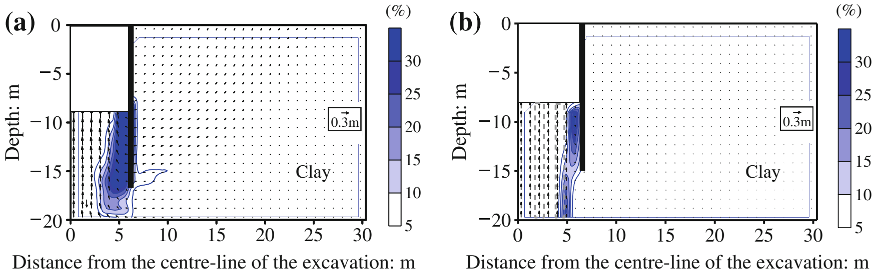

Fig. 8.7 Computed incremental displacement vectors due to hydraulic uplift **a** in test C_0.4 (without piles); **b** in test C_0.4P (with piles)

8.2.6 Uplift Movement in Response to Hydraulic Uplift

Figure 8.8 shows measured and computed uplift movement of clay inside excavation δ_u (normalised by final excavation depth H_e) in response to artesian pressure P_a (normalised by overburden pressure of the clay inside excavation $\gamma_{clay}D$).

In both tests with and without piles, the measured results show that clay inside excavation was not uplifted till the artesian pressure was larger than about $1.20\gamma_{clay}D$. The computed artesian pressures which initiate uplift movement of clay inside excavation (P_i) in the tests with and without piles are very close to the measure values (i.e., $1.21\gamma_{clay}D$ and $1.23\gamma_{clay}D$, respectively). It is revealed by the numerical analysis that in the test without piles, P_i is contributed by overburden pressure of clay inside excavation ($\gamma_{clay}D$) and by downward shear stress along soil-wall interface generated by excavation (about $0.23\gamma_{clay}D$). While in the test with piles, P_i is contributed by overburden pressure of clay inside excavation ($\gamma_{clay}D$) and downward shear stress generated along both soil-wall interface and soil-pile interface (about $0.21\gamma_{clay}D$). By ignoring contribution from the downward shear stress, Eurocode 7 (2004) and British Standard Code (1985) both underestimate P_i of the relatively narrow excavation (i.e., with ratio of excavation width over thickness of clay inside excavation equal to 1) simulated in this study.

When the applied P_a exceeds P_i, clay inside excavation in both centrifuge tests is uplifted, with a gap formed between the clay and its underlying sandy aquifer. The uplift movement increases with P_a and with an increasing rate. At each given P_a, measured uplift movement in tests with and without piles differs no more than 8 %. Computed uplift movements in both tests are close to measured values and also suggest presence of piles does not help to reduce uplift. Numerical back-analysis further reveals that immediately before clay inside excavation was uplifted (when $P_a = P_i$), average horizontal effective stress (σ'_h) acting on the piles in the sandy aquifer was only about 8 kPa. As P_a continues to increase, σ'_h in the sandy aquifer reduced to zero. Therefore, pile lost its pull-out resistance in the sandy aquifer and failed to resist uplift movement of clay inside the excavation. A possible way to

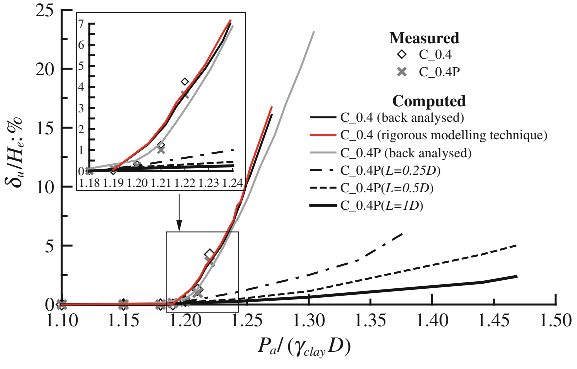

Fig. 8.8 Measured and computed uplift movement in response to artesian pressure

increase pull-out resistance of pile is proposed and verified by numerical parametric study (given later).

As shown in Fig. 8.8, the measured ultimate hydraulic uplift resistance in both centrifuge tests is about $1.22\gamma_{clay}D$. When P_a exceeded $1.22\gamma_{clay}D$ in both centrifuge tests, water started to flow from the sandy aquifer to the formation level of the excavation through the greased clay-model box interface. To obtain the maximum hydraulic pressure the greased clay-model box interface can sustain ($P_{\max}$), an additional test was conducted at 50 g. It is confirmed that $P_{\max}$ is about $1.22\gamma_{clay}D$ (i.e., about 240 kPa). Given the accidental water leakage did not occur, the applied maximum artesian pressure (i.e., $1.22\gamma_{clay}D$) in the two centrifuge tests may be insufficient to cause hydraulic uplift failure. Numerical back-analyses, in which the accidental water leakage was not simulated, show that the ultimate hydraulic uplift resistances (P_u) of the tests with and without piles are $1.30\gamma_{clay}D$ and $1.26\gamma_{clay}D$, respectively. The numerical analyses further reveal that any artisan pressure in excess of P_i is transferred to a vertical shear plane adjacent to soil-wall interface (Fig. 8.7a, b) and resisted by mobilising c_u along the plane, till a fully mobilisation of c_u (details are given later). Compared to the case without piles, slightly higher computed P_u in the case with pile is a result of higher mobilisable c_u (remained after excavation) along the shear plane.

8.2.7 *Bending Moment and Axial Load in Piles*

Figure 8.9 shows measured and computed axial loads in front and rear piles after excavation at the end of excavation. Each computed axial load is normalised by tensile capacity of a concrete pile with an equivalent axial stiffness (EA) in prototype (i.e., with an outer diameter of 1 m and a thickness of 0.05 m). In the calculation of tensile capacity, it is assumed that there is no reinforcement in the pile for simplicity. Tensile strength of concrete is assumed to be 2 MPa, which is typical for concrete with grade ‘C30’. Both measured and computed results show that piles inside excavation are under tension, as expected. It can be seen that overall trends of computed axial loads are similar to the measured ones, but overestimate maximum axial at front and rear piles by about 30 %. One possible reason could be attributed to overestimated basal heave of soil in front of the wall, due to ignorance of stress-path dependency of soil stiffness in the MCC model (as discussed). The maximum measured axial load is about 30 % of tensile capacity of an equivalent concrete pile in prototype. Poulos and Davies (1980) proposed elastic solutions for estimating maximum axial load of single pile subjected to soil heave. Input parameters for the elastic solutions are: pile length, pile diameter, embedment depth of piles in heaving soil (known from PIV analysis), maximum soil heave around the pile (known from PIV analysis) and elastic modulus of soil (assumed to be 3 MPa). Calculated results based on the elastic solution overestimate maximum bending moment at front and rear piles by about 400 and 270 %, respectively. Two major reasons attributed to the significant difference between measured and

Fig. 8.9 Measured and computed axial load after excavation

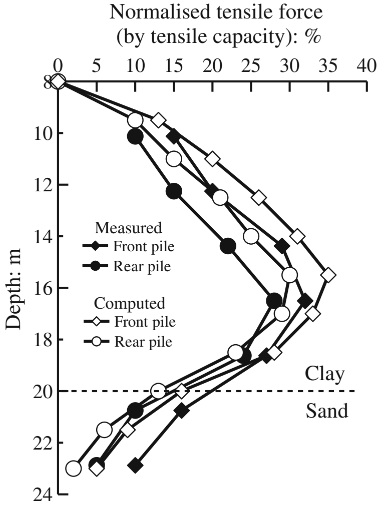

computed values may be ignorance of soil yielding and pile group effect in the elastic solution.

Figure 8.10 shows measured and computed bending moments in front pile and rear pile at the end of excavation. Each presented bending moment is normalised by yield moment of a reinforced concrete pile in prototype (about 800 KNm, according to Loganathan et al. 2000). It can be seen that computed bending moments show a generally similar trend with measured ones, but overestimate maximum bending moment at front and rear piles by about 20 %. The overestimation can be due to many reasons. One possible reason could be attributed to overestimated lateral ground movement in front of the wall (as discussed). As expected, the maximum bending moment in front pile is larger than that in rear pile, as the former is subjected to more lateral soil movement (Fig. 8.4b). The measured maximum bending movement in front pile is about 35 % of its yield moment. Chen and Poulos (1997) proposed elastic solutions for estimating maximum bending moment of single pile subjected to lateral soil movement. Input parameters for the elastic solutions are: pile length, pile diameter, embedment depth of piles in horizontally moved soil (known from PIV analysis), maximum horizontal soil movement around the pile (known from PIV analysis) and elastic modulus of soil (assumed to be 3 MPa). Calculated results based on the elastic solution overestimate maximum bending moment at front and rear piles by about 290 and 280 %, respectively. Two major reasons attributed to the significant difference between measured and computed values may be ignorance of soil yielding and pile group effect in the elastic solution.

During the subsequent hydraulic uplift, bending moment and axial load of pile in the ‘liquefied’ sandy aquifer reduced to almost zero, as expected. Therefore, measured pile responses during hydraulic uplift are not presented.

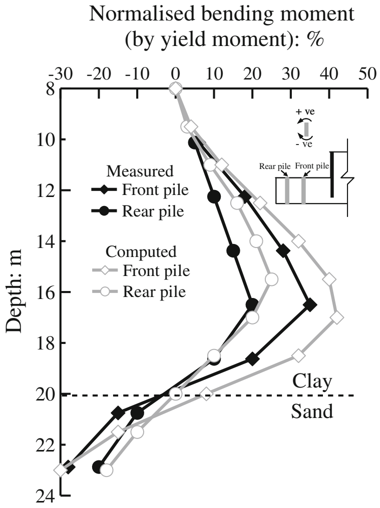

Fig. 8.10 Measured and computed bending movement after excavation

8.2.8 *Prop Load*

Figure 8.11 shows measured and computed prop loads (converted to apparent earth pressure) in tests with and without piles at the end of excavation. The apparent earth pressure envelope proposed by Peck (1969) with $K_a = 1.0$ for excavations supported by stiff walls in soft clay is also included for comparison.

It can be seen that computed apparent earth pressure at each level is larger than that measured, with a maximum percentage difference of no more than 20 %. Larger computed apparent earth pressure (i.e., prop load) than the measured result may be attributed to larger computed initial lateral earth pressure coefficient (Fig. 8.1b).

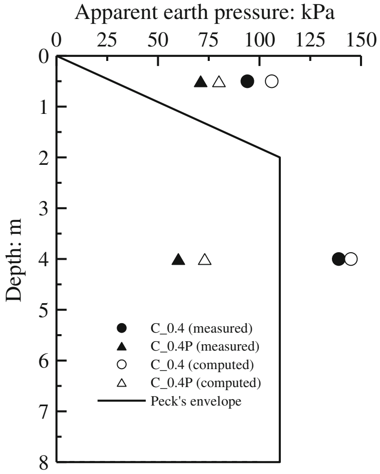

Fig. 8.11 Measured and computed prop load (converted to apparent earth pressure)

Both measured and computed results show that due to presence of piles in front of the wall, axial loads at the first and second levels of props are reduced by about 25 and 57 %, respectively. This implies that there is a load transfer from soil to pile, which reduce passive load taken by the soil in front of the wall and axial load taken by the props (evidence is given later). It is expected that the maximum reduction of axial load occur at the second level of props, as they are closer to the strengthed clay in front of the wall by piles.

Compared to measured and computed apparent earth pressure for cases with and without piles, Peck's (1969) envelope failed to include apparent earth pressure at the first level of props. This is because of high elevation of the props. Similar observations are also made from the case history documented in this study (Chap. 3). At the bottom prop, both measured and computed results show that apparent earth pressures in the case with piles are bounded by Peck's envelope. With absence of piles, apparent earth pressures are larger than that proposed by Peck (1969).

8.3 Improved Understanding from Numerical Back-Analysis

The general agreements between measured and computed results (as reported above) give confidence of the numerical analyses, which are used to improve understanding of the centrifuge tests in this section.

8.3.1 Comparison Between "Idealised Modelling Technique" and "Rigorous Modelling Technique"

In both centrifuge tests and numerical back-anlayses reported above, excavation and hydraulic uplift are separately simulated, in order to differentiate both effects on excavation base instability. It is understood that in practice, excavation is conducted with presence of hydraulic pressure. To examine the validity of the 'idealised modelling technique' adopted in this study, one numerical analysis with 'rigorous modelling technique' (excavation with presence of hydraulic pressure) was carried out. In the numerical analysis with 'rigorous modelling technique', the applied hydraulic pressure is defined as the previously computed ultimate hydraulic pressure from the analysis with 'idealised modelling technique'. Computed result is included in Fig. 8.8 for comparison. It can be seen that computed basal response to hydraulic uplift from both modelling technique is almost identical. This confirms the validity of the 'idealised modelling technique' adopted in this study. Therefore, the 'idealised modelling technique' is adopted in the subsequent numerical parametric studies in this chapter and in the next chapter (i.e., Chap. 9).

8.3.2 Mobilised Undrained Shear Strength

As discussed, the two observed distinct ground deformation mechanisms due to excavation in the test with and without piles (Fig. 8.4a, b) are found to be governed by soil yielding in front of the wall (Fig. 8.5a, b). Considering soil yielding is related to mobilisation undrained shear strength (c_u), Fig. 8.12 compares mobilisation of c_u at two typical soil elements in front of the wall in tests with and without piles (i.e., elements A and B, see the inset in Fig. 8.12) with excavation depth. The moblisation of c_u is defined as the ratio of mobilised undrained shear strength (c_{u_mob}) to undrained shear strength at critical state (c_u). In the same figure, occurrence of soil yielding of each element is also illustrated (by open circular symbols).

It can be seen that in the test without piles (i.e., test C_0.4), yielding of soil elements A and B took place when the excavation was carried out to −4 and −4.5 m, respectively. When the excavation reached −7 m, c_u of elements A and B had been full mobilised. At the same time, the computed results show that the lateral inward movement of the wall suddenly increased significantly (similar to measured data shown in Fig. 8.3) and one sliding wedge was developed on each side of the excavation (Fig. 8.4a). This directly proves that the base instability of this excavation is induced by insufficient passive resistance. In the test with piles (i.e., test C_0.4P), mobilised c_u of elements A and B in response to each excavation step are smaller than those in the test without piles. In addition, larger excavation depths (i.e., −6 and −7 m, respectively) are required to trigger yielding of soil elements A and B. At the end of excavation, c_u of soil elements A and B were not fully mobilised (i.e., $c_{u\_mob}/c_u = 90$ and 94 %, respectively) and hence the excavation remained stable. Due to the presence of the piles, the c_{u_mob} of elements A and B were reduced by 10 and 6 %, respectively. In fact, total passive resistance required to be mobilised for equilibrium of the wall in both tests with and without

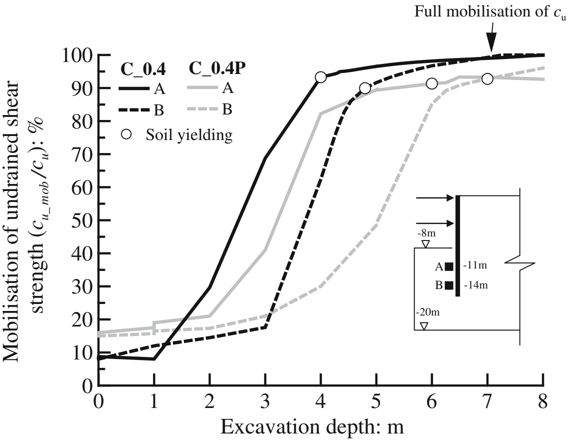

Fig. 8.12 Mobilisation of undrained shear strength during excavation

piles should be the same, due to identical final excavation depths in the two tests. It is very likely that in the test with piles, part of passive load should have been transferred from clay to the piles, such that less mobilisation of c_u is required than that in the test without piles (load transfer between soil and pile are discussed later).

Figure 8.13 compares computed mobilisation of c_u of three typical elements (i.e., elements A, B and C in Fig. 8.13) located in the 'intensive shear plane' during hydraulic uplift in the two tests. As expected, the initial mobilised c_u (prior to hydraulic uplift) of three elements in the test without piles are all larger than those in the test with piles. In another words, less mobilisable c_u was left after excavation in the test without piles. After artesian pressure was applied, c_u of all elements in both tests did not start to mobilise till P_a was larger than $1.2\gamma_{clay}D$. This is because any P_a less than $1.2\gamma_{clay}D$ was counter-balanced by the apparent overburden pressure of clay inside excavation (i.e., $1.2\gamma_{clay}D$). When P_a was larger than $1.2\gamma_{clay}D$, uplift movement of the excavation base was triggered in both tests (Fig. 8.8). Simultaneously, mobilisation of c_u of all selected elements commenced, except elements A and B in the test without piles (in which the c_u had been fully mobilised due to excavation). This implies that as the applied artesian pressure exceeded the apparent overburden pressure of the excavation base, further increase in artisan pressure was resisted by mobilising shearing resistance of clay along the shear plane induced by hydraulic uplift (Fig. 8.7a, b). As shown in Fig. 8.13, increased artesian pressure resulted in a continuous mobilisation of c_u (except elements A and B in the test without piles) in the two tests. Upon full mobilisation of c_u of all elements A, B and C, the excavation base was not able to take any further increase of artesian pressure and an ultimate state of hydraulic uplift was reached. Based on mobilised c_u of each element along the shear plane, contribution of the shearing resistance to the ultimate hydraulic uplift resistance can be calculated. The calculated shearing resistances in test with and without piles are equivalent to $0.04\gamma_{clay}D$ and $0.1\gamma_{clay}D$, respectively. These values are almost the

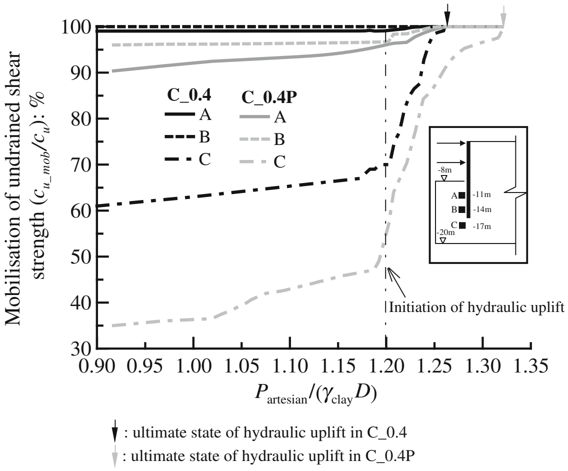

Fig. 8.13 Mobilisation of undrained shear strength during hydraulic uplift

same as the amount of artesian pressure in excess of P_i (i.e., $0.05\gamma_{clay}D$ and $0.11\gamma_{clay}D$, respectively, as deduced from Fig. 8.13). This indicates that the ultimate hydraulic uplift resistance for these two excavations consists of 'apparent overburden pressure' of the excavation base and shearing resistance along the shear plane induced by hydraulic uplift (Fig. 8.7a, b). The shearing resistance depends on mobilisable c_u after excavation. In this study, mobilisable c_u after excavation in the test with piles is larger than that in the test without piles. Therefore, a larger P_u is resulted. Nonetheless, contribution of shearing resistance in the test with and without piles in this study (i.e., 3 and 8 % of P_u, respectively) may be too small to be considered. For excavations in ground with relatively large c_u, contribution of shearing resistance to P_u may not be ignored.

8.3.3 Load Transfer from Soil to Pile

Stabilisation effect of piles during excavation has been demonstrated based on comparison of ground deformations in cases with and without piles (Fig. 8.4a, b). The presence of piles is considered to stabilise excavation by increasing passive resistance in front of the wall. To verify this postulation, Fig. 8.14a compares computed total horizontal earth pressure in front of the wall at the end of excavation ($\sigma_{h\_8\ \mathrm{m}}$) in cases with and without piles (i.e., tests C_0.4P and C_0.4). For clarity, only distribution of earth pressures along A-A′ and at a typical depth (4 m below the formation level of the excavation) is shown. Each presented $\sigma_{h\_8\ \mathrm{m}}$ is nomalised by its corresponding horizontal total earth pressure before excavation ($\sigma_{h\_0\ \mathrm{m}}$). It can be seen that at the end of excavation, average $\sigma_{h\_8\ \mathrm{m}}$ in the case with and without piles decreased to about 82 and 51 % of $\sigma_{h\_0\ \mathrm{m}}$, respectively. This implies that by installing piles in front of the wall, $\sigma_{h\_8\ \mathrm{m}}$ has been increased by about 70 %. As shown in the case with piles, $\sigma_{h\_8\ \mathrm{m}}$ acting on the pile is about 35 % larger than that on soil between piles. This suggests there is a load transfer from soil to piles. As a result, passive resistance in front of the wall is increased.

Figure 8.14b compares change of horizontal and vertical effective stress due to excavation ($\Delta\sigma'_h$ and $\Delta\sigma'_v$) in the cases with and without piles. Each presented $\Delta\sigma'_h$ and $\Delta\sigma'_v$ is normalised by its corresponding horizontal and vertical effective stress before excavation (σ'_{h0} and σ'_{v0}), respectively. In the figure, positive sign refers to an increase of effective stress after excavation, and vice versa. It is illustrated that vertical effective stress in both cases decreased after excavation, regardless of presence of piles. However, presence of piles helped to reduce $\Delta\sigma'_v$ by about 51 %. This is because during excavation, soil in front of the wall heaves in relative to piles and is 'dragged down' by piles (by mobilising downward shear stress along pile shaft). This downward shear stress partially compensates vertical unloading in soil. In another words, part of vertical unloading in soil is transferred to pile. During the same period, horizontal effective stress in both cases with and without piles increased slightly (less than 10 %), due to inward movement of wall. $\Delta\sigma'_h$ in the case with piles is 7 % larger than that in the case without piles. In summary, soil

Fig. 8.14 Computed **a** nomalised total horizontal stress, **b** normalised effective horizontal & vertical stress and **c** mobilisation of undrained shear strength in front of the wall (along A-A′) at the end of excavation

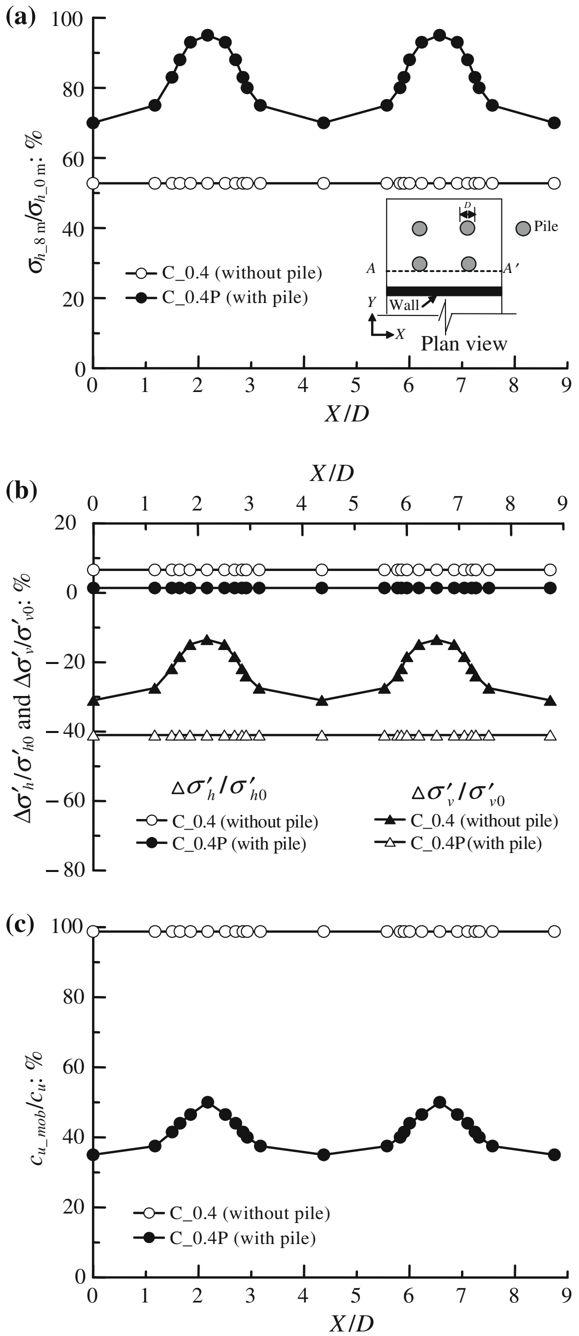

elements adjacent to the wall were subjected to horizontal loading and vertical unloading (in terms of effective stress) during excavation in both cases with and without piles. Due to presence of piles, vertical unloading of soil is greatly reduced (i.e., 51 %) while horizontal loading is slightly increased (i.e., 7 %). Therefore, deviatoric stress of soil (and hence mobilised c_u) at the end of excavation in the case with piles should have been less than that in the case without piles.

Figure 8.14c shows mobilisation of undrained shear strength (i.e., c_{u_mob}/c_u, where c_{u_mob} and c_u denotes mobilised and initial undrained shear strength, respectively) of the same soil elements as those in Figs. 8.14a, b. Comparison of c_{u_mob}/c_u between tests with and without piles shows that due to presence of piles, average c_{u_mob}/c_u of soil adjacent to the wall is reduced by about 53 %. Accordingly, plastic deformation of soil in front of the wall is reduced, so is lateral wall displacement (Fig. 8.3).

8.4 Numerical Parametric Study on Embedment Depth of Piles

As discussed in the previous section, the sandy aquifer liquefies due to hydraulic uplift. Accordingly, piles in the aquifer lose pull-out resistance and fail to resist uplift of clay inside excavation. To obtain sufficient pull-out resistance for piles, one possible way is to extend length of piles to soil layers underneath the sandy aquifer (given the aquifer is not too thick). In some regions such as Shanghai, the sandy aquifer could be as thin as 4 m (as reported in the documented case history Chap. 3) and is underlain by clay layers. Under such circumstance, it may not cost too much to install piles into the clay layer underneath the aquifer. To investigate influence of embedded depth of piles in the lower clay layer on effectiveness of 'anti-uplift', parametric studies were carried out using the numerical tool calibrated in this study. Finite element mesh adopted for the numerical parametric analysis is identical to that for back-analysis, except including an additional clay layer (30 m thick in prototype) underneath the existing sandy aquifer. c_u profile of this lower clay layer is approximately a linear extension of that in the upper clay layer (Fig. 8.2). In the parametric study, piles are installed into the lower clay layer with their embedment depths in the layer (L) varied. Diameters and spacings of piles in the parametric study are identical to those in numerical back-analyses.

8.4.1 Influence of Pile Length on Effectiveness of Base Stabilisation

Figure 8.8 shows computed uplift movement of clay inside excavations installed with piles with three typical L (i.e., $L = 0.25D$, $0.5D$ and $1D$, where D is embedded depth of pile in the upper clay layer). As illustrated, P_i does not change with L. P_u

increases with L till it reaches $0.5D$. A further increase in L from 0.5 to 1 D leads to a further reduction of ultimate uplift movement while P_u remains unchanged (explained later). Comparison of computed results between cases without piles (C_0.4 (back-analysed)) and with piles (C_0.4P ($L = 1D$)) indicates that presence of piles can increase P_u by 16 % while reduce ultimate uplift movement by 80 %.

8.4.2 Axial Load and Unit Shaft Friction of Piles with Varied Lengths

While resisting uplift, piles inside excavation are anticipated to be under tension. Figure 8.15a shows computed axial load in rear pile in cases with varied L (i.e., $L = 0.25D$, $0.5D$ and $1D$) at the end of hydraulic uplift. Axial load in each front pile is not included, as its distribution is similar to that of rear pile while its maximum value is slightly less than that in rear pile (i.e., no more than 15 %). It can be seen that piles with varied L are all subjected to tension, with neutral plane located at the boundary between upper clay layer and sandy aquifer. The maximum axial load ($AL_{\max}$) of each pile is in the sandy aquifer and it remains constant with depth. $AL_{\max}$ increases with L till L reaches $0.5D$. With a further increase in L, $AL_{\max}$ remains constant (explained later).

Figure 8.15b shows computed mobilised unit shaft friction (USF) in rear pile in cases with varied L (i.e., $L = 0.25D$, $0.5D$ and $1D$) at the end of hydraulic uplift. In the figure, USF (f_s) is only referred to the portion of the pile in the two clay layers and is normalised by c_u. The f_s/c_u ratio is equivalent to the conventionally defined adhesion factor α. It can be seen that along each pile shaft embedded in the upper clay layer, positive skin friction (soil tends to heave in relative to pile) is induced. This is because clay inside excavation heaves upwards in relative to pile. In another word, the artesian pressure acting on the bottom of clay is transferred to pile via shearing (positive skin friction). This positive skin friction (PSF) is counter-balanced by negative skin friction (soil tends to settle in relative to pile) mobilised along each pile shaft embedded in the lower clay layer. No shaft friction is induced along each pile shaft embedded in the sandy aquifer, because of zero effective stress in the layer (as discussed). Therefore, tensile force of each pile in the sandy aquifer remains unchanged (Fig. 8.15a). Comparison of shaft friction between piles with varied L shows that mobilised NSF along piles in the upper clay layer increases with L till it reaches $0.5D$. This implies that while L increases to $0.5D$, NSF mobilised along the lower part of the pile becomes sufficient to counter balance a fully-mobilised PSF along pile shaft in the upper clay layer. While L is further increased from $0.5D$ to $1D$, no more PSF is mobilised, so is the maximum tensile load (Fig. 8.15a). Therefore, mobilised NSF reduces with L due to increased area of pile shaft embedded in the lower clay layer. Because of reduced PSF, uplift movement of pile in relative to the lower clay layer decreases, so does the total uplift movement of clay inside excavation (Fig. 8.8).

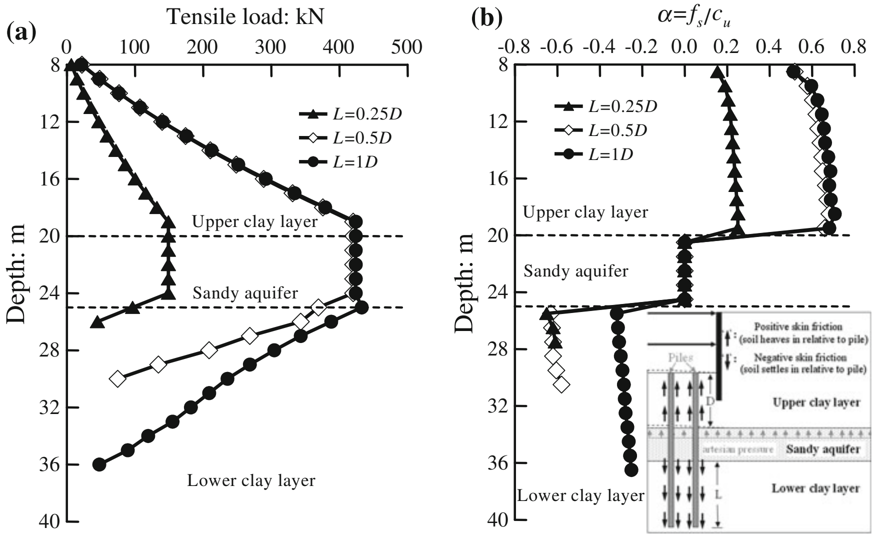

Fig. 8.15 Computed response of piles with varied lengths at the end of hydraulic uplift. **a** Axial load; **b** Mobilised unit shaft friction

As shown in Fig. 8.15b, the average ultimate mobilised NSF is about 63 % of c_u (i.e., adhesion factor $\alpha = 0.63$). Previously published centrifuge test results (Ng et al. 2008) show that the ultimate α value for a single pile (with the same interface as that in this study) in kaolin clay is about 1.12. If the reported α by Ng et al. (2008) is applicable to this study, group efficiency in this study is about 58 %. At the ultimate state of hydraulic uplift for excavations with piles, computed results show that the most significant plastic strain is mobilised along soil-pile interface.

8.5 Summary and Conclusions

Two centrifuge model tests and three-dimensinal finite element back-analyses (with and without piles) were carried out to study failure mechanism of excavation subjected to hydraulic uplift and stabilisation effects due to piles installed inside excavation. In addition, parametric studies using the calibrated numerical tool were conducted to investigate influence of pile length (and hence its pull-out resistance) on effectiveness of base stabilisation. Based on the physical and numerical investigation, the following conclusions can be drawn:

(1) Based on the geometry and ground conditions modeled, both measured and computed results show that artesian pressure required to initiate uplift movement of clay (P_i) inside excavation without piles is about 1.2 times of overburden pressure of the clay (P_o). Numerical back-analysis reveals that the basal

resistance (i.e., $1.2P_o$) consists of overburden pressure of clay inside excavation and downward shear stress developed along the soil-wall interface (i.e., $0.2P_o$). By ignoring the contribution of downward shear stress, Eurocode 7 (2004) and British Standard Code (1985) may underestimate P_i.

(2) When an applied artesian pressure is larger than P_i, clay inside the excavation without the use of anti-uplift piles moves upwards vertically as a rigid body. Shearing between clays on both sides of the wall (due to their relative movement) results in a distinct shear plane. Any artisan pressure in excess of P_i is transferred to the shear plane and resisted by mobilising undrained shear strength (c_u) along the plane, till full mobilisation of c_u is achieved.

(3) When 'anti-uplift' piles are installed in front of the wall, the resulted P_i is almost the same as that of excavation without piles. When applied artesian pressure is larger than P_i, clay inside the excavation heaves upwards. The uplift movement of the clay is partially suppressed by downward shear stress mobilised along the soil-pile interface. The effectiveness of 'anti-uplift' pile depends on its pull-out resistance (i.e., embedded depth in this study) in soil layers beneath the top clay layer. To acquire sufficient pull-out resistance, anti-uplift piles should be extended to clay layers underneath sandy aquifer. Numerical parametric studies reveal that the optimum embedded depth of piles in the lower clay layer (L) is about half of its embedded depth in the top clay layer. The ultimate uplift movement of clay inside the excavation can then be reduced by 80 % while the ultimate basal resistance against hydraulic uplift is increased by 16 %. Each pile is subjected to tension with a group efficiency of about 58 %.

(4) The presence of anti-uplifts increases the passive resistance in front of the wall by about 70 %, while they reduce c_u mobilised in the clay by about 53 % on the excavated side. This is because some passive loads were transferred from clay to piles. Due to increased passive resistance, the potentially unstable excavation can be stabilised. The maximum ground surface settlement ($\delta_{v\text{-max}}$) and lateral wall displacement due to excavation can be reduced by 68 and 75 %, respectively.

References

Barbosa-Cruz ER, Randolph MF (2005) Bearing capacity and large penetration of a cylindrical object at shallow embedment. In: Proceedings of the international symposium on frontiers in offshore geotechnics SFOG, Perth, pp 615–621

Bjerrum L, Eide O (1956) Stability of strutted excavation in clay. Géotechnique 5(1):7–17

Bolton MD, Stewart DI (1994) The effect on propped diaphragm walls of rising groundwater in stiff clay. Géotechnique 44(1):111–127

British Standards Institution (1985) Code of Practise for Foundations. BS 8004: 1986

BS EN 1997-1:2004 (2004) Eurocode 7: geotechnical design – Part 1: general rules. BSI

Burland J (1989) Small is beautiful: the stiffness of soil at small strains. Can Geotech J 26(4): 499–516

Chen LT, Poulos HG (1997) Piles subjected to lateral soil movement. J Geotech Geoenvironmental Eng 123(9):802–811

Gourvenec S, Acosta-Matinez HE, Randolph MF (2009) Uplift resistance of shallow skirted foundations in clay under transient and sustained concentric loading. Géotechnique 59(6): 525–537

Loganathan N, Poulos HG, Stewart DP (2000) Centrifuge model testing of tunnelling-induced ground and pile deformations. Géotechnique 50(3):283–294

Mcnamara MA (2001) Influence of heave reducing piles on ground movements around excavations. Ph D Thesis, City University of London, UK

Ng CWW (1998) Observed performance of multipropped excavation in stiff clay. J Geotech Geoenvironmental Eng, ASCE 124(9):889–905

Ng CWW, Lings ML (1995) Effects of modelling soil non-linearity and wall installation on the back-analysis of a deep excavation in stiff clay. J Geotech Geoenvironmental Eng, ASCE 121 (10):687–695

Ng CWW, Poulos HG, Chan VSH, Lam SY, Chan GCY (2008) Effects of tip location and shielding on piles in consolidating ground. Can Geotech J 134(9):1245–1260

Peck RB (1969) Deep excavation and tunneling in soft ground. In: Proceeding of the 7th international conference on soil mechanics and foundation engineering, Mexico City, State-of-the-Art Volume, pp 225–290

Polous HG, Chen LT (1997) Pile response due to excavation-induced lateral soil movement. J Geotech Geoenvironmental Eng, ASCE 123(2):94–99

Poulos HG, Davies EH (1980) Pile foundation analysis and design. Wiley, New York

Randolph MF, Houlsby GT (1984) The limiting pressure on a circular pile loaded laterally in cohesive soil. Géotechnique 34(4):613–623

Chapter 9
Numerical Parametric Study

9.1 Introduction

In Chap. 8, the initiation and failure mechanisms of excavation subjected to hydraulic uplift are investigated by carrying out two centrifuge tests and numerical back-analyses. In spite of the reported initiation and failure mechanisms, the conclusions may be limited to the geometry of excavation and undrained shear strength of clay (c_u) modelled.

In this chapter, a systematic numerical investigation on the initiation and failure mechanisms of excavations with varied geometries of excavation and undrained shear strength of clay (c_u) is presented.

Based on the parametric studies, key factors governing initiation and failure mechanisms of base instability due to hydraulic uplift are investigated and quantified. A calculation chart for estimating hydraulic pressure which initiates uplift of excavations with varied geometries and c_u is developed. Two typical types of failure mechanism are identified and discussed.

9.2 Numerical Parametric Study

Figure 9.1 shows a schematic diagram of excavation in clay overlying an aquifer. Based on dimensional analysis and a back of envelope calculation conducted in Chap. 5, it is suggested that the following two dimensionless groups are likely to be most relevant to basal response subjected to hydraulic uplift:

Y. Hong and L. Wang, *Deformation and Failure Mechanism of Excavation in Clay Subjected to Hydraulic Uplift*, Advanced Topics in Science and Technology in China, DOI 10.1007/978-3-662-46507-3_9

Fig. 9.1 A schematic diagram showing excavation in clay subjected to hydraulic uplift

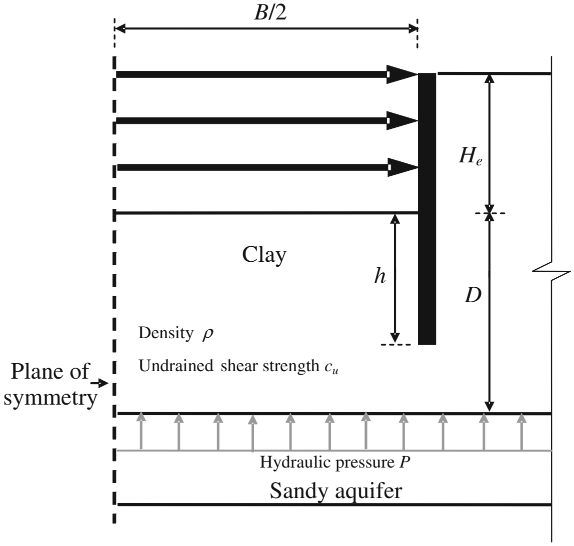

(a) ratio of excavation width over thickness of clay on the excavate side: B/D;

(b) ratio of undrained shear strength of clay over overburden pressure of clay on the excavated side: $c_u/(\rho gD)$.

To study and quantify effects of these two dimensionless groups on the initiation and failure mechanisms of excavation subjected to hydraulic uplift, two series of coupled-consolidation finite element analyses are carried out using a program ABAQUS. Details of finite element analysis (i.e., mesh and boundary conditions, constitutive model and model parameters, modelling procedures) are given in Chap. 7. Constitutive model, model parameters and modelling procedures adopted in each analysis in this chapter have been validated against results of centrifuge tests, as reported in Chap. 8.

In each analysis, the final excavation depth (H_e) and thickness of clay on the excavated side (D) are kept the same (i.e., 8 and 12 m in prototype, respectively). Each excavation is retained by a 600-mm thick diaphragm wall, which is supported horizontally by two levels of props (with a vertical prop spacing = 4 m).

The excavation width (B) is varied from 8 to 120 m, resulting a B/D ratio encompassing the range of practical interest (i.e., from 0.75 to 10). For each B/D, five c_u values are considered (i.e., 25, 30, 35, 40 and 70 kPa). The adopted c_u ranging from 25 to 40 kPa corresponds to soft clay while the c_u of 70 kPa refers to firm clay, based on classification on clay by BSI (1981). Corresponding to these selected five c_u values, the dimensionless group $c_u/(\rho gD)$ = 0.13, 0.16, 0.18, 0.21 and 0.36. Each c_u quoted in this study refers to average undrained shear strength of clay between the formation level and the bottom of each excavation.

Table 9.1 summarises the numerical parametric study in this chapter.

Table 9.1 Summary of numerical parametric study

Excavation width over thickness of excavation base ratio: B/D	Undrained shear strength over overburden pressure of excavation base ratio: $c_u/(\rho g D)$
0.75, 1.0, 2.0, 3.0, 4.0, 5.0, 6.0, 7.0, 8.0, 10.0	0.13 (c_u = 25 kPa)
	0.16 (c_u = 30 kPa)
	0.18 (c_u = 35 kPa)
	0.21 (c_u = 40 kPa)
	0.36 (c_u = 70 kPa)

9.3 Results of Numerical Parametric Study

9.3.1 Uplift Movement in Response of Hydraulic Pressure

Figure 9.2 shows uplift movement δ_u (normalised by D) of clay inside excavation (at point A) in response to increased artesian pressure P_a (normalised by $\rho g D$). Presented cases with two B/D ratios of 1 and 6 are intended to represent relatively narrow and wide excavations, respectively. For each B/D ratio, two $c_u/(\rho g D)$ ratios of 0.13 and 0.26 are adopted to represent soft clay and firm clay (based on BSI (1981)), respectively.

For the relatively narrow excavation (B/D = 1), artesian pressures required to initiate uplift movement of clay inside excavation (P_i) for soft clay and firm clay are equal to $1.22\rho g D$ to $1.33\rho g D$, respectively. P_i increases slightly with undrained shear strength (i.e., with an increase of 9 %). In EC 7 (2004) and BSI Code (1985), P_i is simply estimated as $\rho g D$. This simplified solution is shown to underestimate relatively narrow excavations.

For the relatively wide excavation (B/D = 6), less artesian pressure is required to initiate uplift. It can be seen that P_i for the relatively wide excavation in soft clay and firm clay is almost identical (i.e., $P_i = \rho g D$), being about 30 % smaller (on average) than those in the relatively narrow excavation.

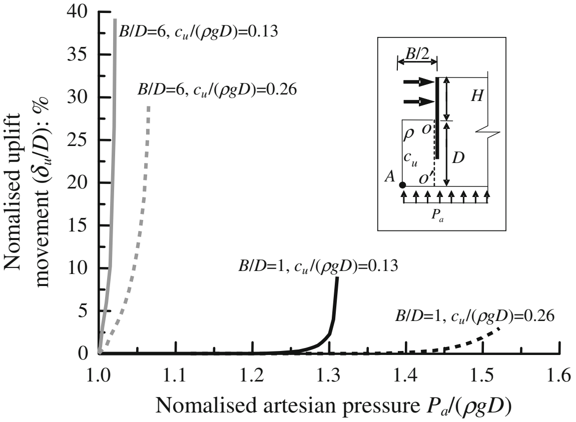

Fig. 9.2 Uplift movement (of point A) in response to artesian pressure

While comparing the ultimate artesian pressure (P_u) required to cause failure in all cases presented, it can be seen that increase of c_u can result in a slightly larger P_u (no more than 19 %). However, the mobilisation of c_u is accompanied by substantial uplift movement (no less than 3.2 %D, equal to 384 mm). This is much larger than tolerable basal heave (no more than 2 mm per day) specified in design codes such as SMCC (1997) for excavations in Shanghai. CIRIA report C515 (Preene et al. 2000), which recommends to make use of undrained shear strength to resist hydraulic uplift, is therefore not applicable to excavations where basal heave should be strictly controlled.

9.3.2 Initiation of Hydraulic Uplift

In this study, initiation of hydraulic uplift is defined as the moment when uplift movement of clay inside exacavation starts to be larger than zero. It is illustrated in the previous section that artesian pressure required to initiate (P_i) is related to excavation width (B/D) and undrained shear strength of clay ($c_u/(\rho gD)$). From equilibrium point of view, uplift is only initiated when applied artesian pressure is larger than contact pressure of clay inside excavation acting on the sandy aquifer (defined as 'apparent overburden pressure' in this study). It is obvious that apparent overburden pressure of clay inside excavation (P_{ap}) is a function of overburden pressure (P_o) and downward shear stress (τ_d) mobilised the soil-wall interface. This section aims at explaining the observed dependency of P_i (in the previous section) on B/D and $c_u/(\rho gD)$, by investigating effect of these two dimensionless groups on P_{ap}.

Figure 9.3 shows distribution of apparent overburden pressure inside excavation (P_{ap}) along the distance from the centre-line of the excavation (i.e., along X-abscissa, see inset of Fig. 9.3). All presented data are taken from the moment immediately after excavation and before applying artesian pressure. The difference between P_{ap} and P_o corresponds to additional downward pressure (P_τ) due to shear stress mobilised along the soil-wall interface inside excavation (plane O–O', see Fig. 9.3).

As expected, maximum P_τ in each case is found along the soil-wall interface. The P_τ decreased with distance from the soil-wall interface and reduced to a minimum value along the centre-line of the excavation. Therefore, a wider excavation results in a smaller P_τ and hence a smaller P_{ap} at the centre-line of the excavation (i.e., $X = 0$). It is worth noting that P_{ap} at the centre-line of the excavation corresponds to the artesian pressure required to initiate uplift (P_i). It can be seen that for the relatively wide excavations ($B/D = 6$), P_τ at the centre-line of the excavation is almost negligible, hence P_i of this relatively wide excavation is governed by P_o (i.e., ρgD). Therefore, the simplified solution ($P_i = \rho gD$) in EC 7 (2004) and BSI (1985) gives a good estimation for P_i of relatively wide excavations. For the relatively narrow excavation ($B/D = 1$), however, P_τ at the centre-line of the excavation is equivalent to about $0.25\rho gD$ (i.e., $P_{ap} = 1.25\rho gD$). As a result, this relatively narrow excavation ($B/D = 1$) has a 25 % larger resistance to hydraulic

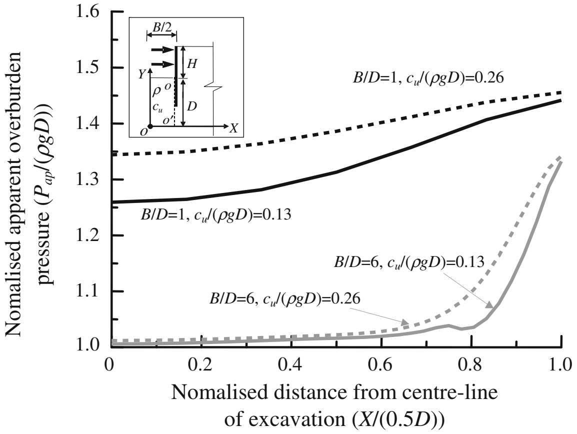

Fig. 9.3 Apparent overburden pressure of clay inside excavation

uplift than that of the relatively wide excavation ($B/D = 6$). This suggests that by neglecting effect of P_τ, the simplified solution in current practice (i.e., $\rho g D$) underestimates P_i of relatively narrow excavations.

For a given B/D, P_{ap} increases $c_u/(\rho g D)$. This is because larger undrained shear strength allows more shear stress to be mobilised along the soil-wall interface. Accordingly, larger P_τ is resulted and hence P_{ap}.

9.3.3 *Calculation Chart for Estimating Initiation of Hydraulic Uplift (P_i)*

By conducting numerical parametric study on excavations with different combinations of B/D and $c_u/(\rho g D)$ (see Table 9.1), varied values of P_i (equal to P_{ap}) are resulted. Figure 9.4 shows a calculation chart correlating the dimensionless groups B/D and $c_u/(\rho g D)$ to $P_i/(\rho g D)$. Artesian head corresponding to $P_i/(\rho g D)$ is also included in the figure for reference.

The calculation chart reveals that for a relatively narrow excavation with a B/D of 0.75, P_i is about 1.45$\rho g D$. This implies the contribution of downward shear stress along the soil-wall interface inside excavation to hydraulic uplift resistance is 0.45$\rho g D$. Current practice (EC 7 (2004) and BSI (1985)) ignoring the contribution of downward shear stress may underestimate P_i of relatively narrow excavations by up to 45 %. For this case, tolerable artesian head is about 7.5 m. This is larger than reported artesian head in case histories worldwide, as summarized in Table 9.2. It is also shown that $P_i/(\rho g D)$ decreases as B/D increases, implying contribution of downward shear stress along the lateral boundary of clay in excavation to P_i becomes less significant as excavation becomes wider. When B/D increases to larger than 3, $P_i/(\rho g D)$ reduces to almost 1. This indicates for relatively wide excavations (B/D no less than 3), P_i is dominated by overburden pressure of clay inside

Fig. 9.4 Calculation chart for estimating artisan pressure to initiate uplift movement

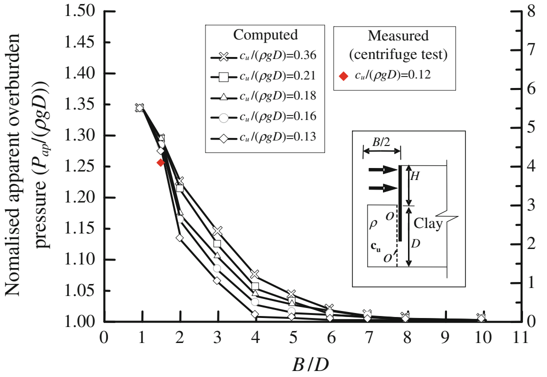

Table 9.2 Reported artesian head from case histories worldwide

Region	Artesian head* (m)	References
Goderich, Ontario, Canada	6.1	Milligan and Lo (1970)
Sudbury, Ontario, Canada	5.5	Milligan and Lo (1970)
Southampton, U.K.	2.8	Ward (1957)
Toronto, Ontario, Canada	2.1	Milligan and Lo (1970)
Mel bone, Australia	1 to 2.3	Ervin et al. (2004)
San Francisco, U.S.	1	Clough and Reed (1984)
Oxford, U.K.	0.2	Moore and Longworth (1979)
Singapore	1.0	Davies (1984)
Shanghai, China	5	Ng et al. (2012)

*Datum is defined at the ground surface

excavation (ρgD) and effect of downward shear stress can be negligible. Therefore, the simplified solution adopted in current practice ($P_i/(\rho gD)$) gives a close estimation for relatively wide excavations.

For excavations with a give width (B/D) but varied undrained shear strength ($c_u/(\rho gD)$), the maximum percentage difference of resulted P_i is no more than 9 %. Therefore, P_i is more dominated by excavation width (which varies P_i by up to 45 %) than undrained shear strength.

Measured P_i of an excavation ($B/D = 1$ and $c_u/(\rho gD) = 0.12$) in a centrifuge test conducted in this study (see Chap. 8) is also included in the calculation chart for comparison. It can be seen that measured P_i is close to corresponding computed value, with a percentage difference of about 3 %.

9.3.4 Failure Mechanism

Figure 9.5a shows incremental displacement vectors due to hydraulic uplift in a relatively narrow excavation in soft clay ($B/D = 1$ and $c_u/(\rho gD) = 0.13$). In response

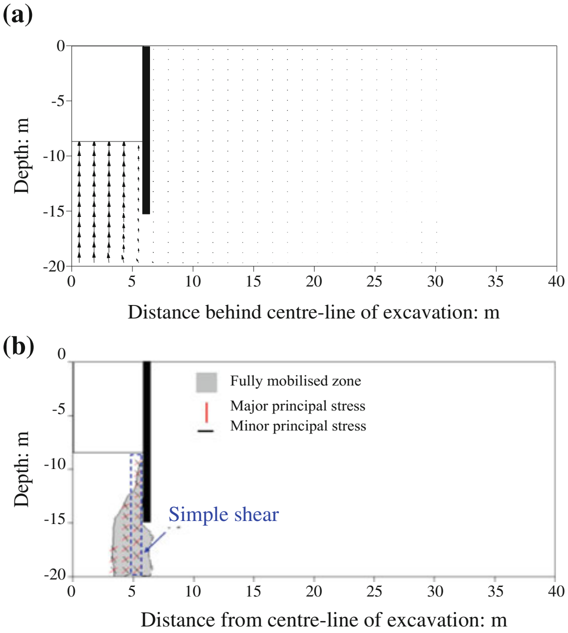

Fig. 9.5 Failure mechanism of a relatively narrow excavation in soft clay ($B/D = 6$, $c_u/(\rho g D) = 0.13$). **a** Incremental displacement vector due to hydraulic uplift; **b** Failure zone and failure mode

to the hydraulic pressure acting on bottom of the clay layer, clay inside excavation moves upwards vertically in a rigid body manner while clay outside the excavation remains stationary. This computed ground deformation mechanism is consistent with that observed from the centrifuge test reported in Chap. 8. It is worth pointing out that geometries of excavation, undrained shear strength of clay and modelling procedure in the reported centrifuge test ($B/D = 1$ and $c_u/(\rho g D) = 0.12$) are similar to that in this numerical analysis.

Figure 9.5b illustrates failure zone (where c_u is fully mobilised) and principal stress in the failure zone in the relatively narrow excavation in soft clay. It can be seen that c_u is fully mobilised along a vertical plane adjacent to the soil-wall interface. Directions of principal stresses in the failure zone are about 45° relative to the horizontal and vertical directions. This suggests soil fails by simple shear, which is induced by relative vertical movement between uplifted clay inside excavation and stationary clay outside excavation (Fig. 9.5a). The numerical analysis further reveals that prior to failure, any artisan pressure in excess of P_i is resisted by mobilising c_u along the soil-wall interface.

Figure 9.6a shows incremental displacement vectors due to hydraulic uplift in a relatively wide excavation in soft clay (i.e., $B/D = 1$ and $c_u/(\rho g D) = 0.13$) in soft clay. It can be seen that clay inside excavation is uplifted and rotates in clockwise direction with respect to a point adjacent to the wall (i.e., point P in Fig. 9.6a). Movement of clay inside excavation is generally dominated by upwards vertical displacement. The vertical displacement increases with horizontal distance from the wall and maximises at plane of symmetry (PS), corresponding to the rotational

Fig. 9.6 Failure mechanism of a relatively wide excavation in soft clay ($B/D = 6$, $c_u/(\rho g D) = 0.13$). **a** Incremental displacement vector due to hydraulic uplift; **b** Failure zone and failure mode

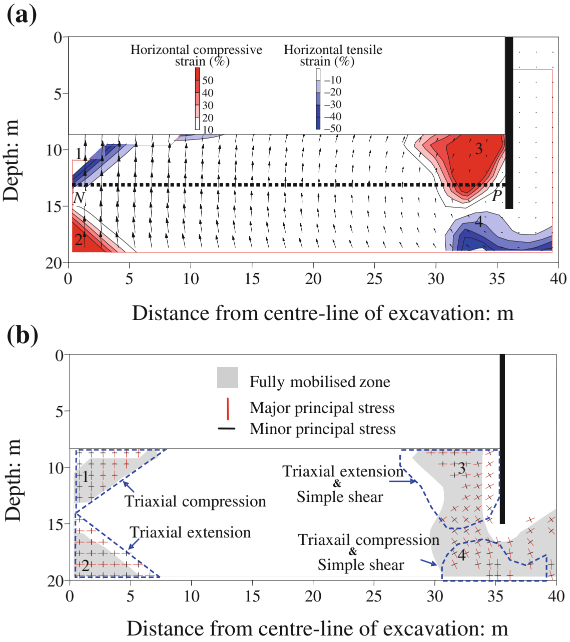

motion of soil. Different from ground deformation mechanism of the relatively narrow excavation (Fig. 9.5a), some horizontal displacement is observed in the relatively wide excavation. It is worth noting that direction and magnitude of the horizontal displacement change with depth. A neutral plane, in which horizontal displacement is zero, is identified and shown in the figure (see '*NP*'). It can be observed that horizontal displacement of soil above *NP* tends to move away from *PS* of the excavation while that below *NP* tends to move towards *PS*. Moreover, magnitude of horizontal displacement of soil increases with its vertical distance from the *NP*. This suggests clay inside excavation is also subjected to bending deflection, in addition to the previously observed rotational motion. Bending deflection of clay inside excavation is suppressed at its two ends, as shown by greatly reduced horizontal displacement near the middle of the excavation and near the wall. Horizontal strain is anticipated to be induced. Therefore, computed incremental horizontal strain due to hydraulic uplift is also included in Fig. 9.6. For soil adjacent to middle of the excavation and above *NP* (zone 1), significant horizontal tensile strain (about 35 % on average) is induced as the soil tends to move away from *PS*. On the contrary, significant horizontal compressive strain (about 32 % on average) is induced in soil adjacent to *PS* but below *NP* (zone 2), as the soil tends to move towards *PS*. For similar reasons, substantial horizontal compressive strain is induced in front of soil-wall interface (zone 3) while tensile strain is induced below wall toe (zone 4).

Figure 9.6b shows zones where c_u are fully mobilised and directions of principal stress in each failure zone in the relatively wide excavation. As illustrated, c_u is fully mobilised in zones where substantial horizontal strain is induced (i.e., zones 1, 2, 3 and 4). In zones 1 and 2, directions of major principal stress align vertically and horizontally, respectively. This indicates soil in zones 1 and 2 fails in triaxial compression and triaxial extension, which are corresponding to horizontal tensile strain and horizontal compressive strain (Fig. 9.6a), respectively. In the vicinity to the wall, soil does not only fail in triaxial extension (zone 3, where horizontal tensile strain is induced) and in triaxial compression (zone 4, where horizontal compressive strain is induced) but also in simple shear (in both zones 3 and 4). The latter is induced by relatively vertical movement between uplifted clay inside excavation and stationary clay outside the excavation.

It is worth noting that the transition *B/D* ratio which differentiates narrow and wide excavations in this study is indentified to be 3. In the section discussed above, the cases with *B/D* = 1 and 6 are just two typical cases representing a narrow and a wide excavation, respectively.

The distinct failure mechanisms due to varied width of excavation can be explained by the back of envelope calculation conducted in Chap. 5 (see Fig. 9.7). In that calculation, for clay inside excavation subjected to hydraulic pressure, a simple analogy was made with a statically indeterminate beam loaded by an upward uniformly distributed load (provide clay has apparent cohesion). The calculation shows that due to hydraulic uplift, both bending moment and shear force are

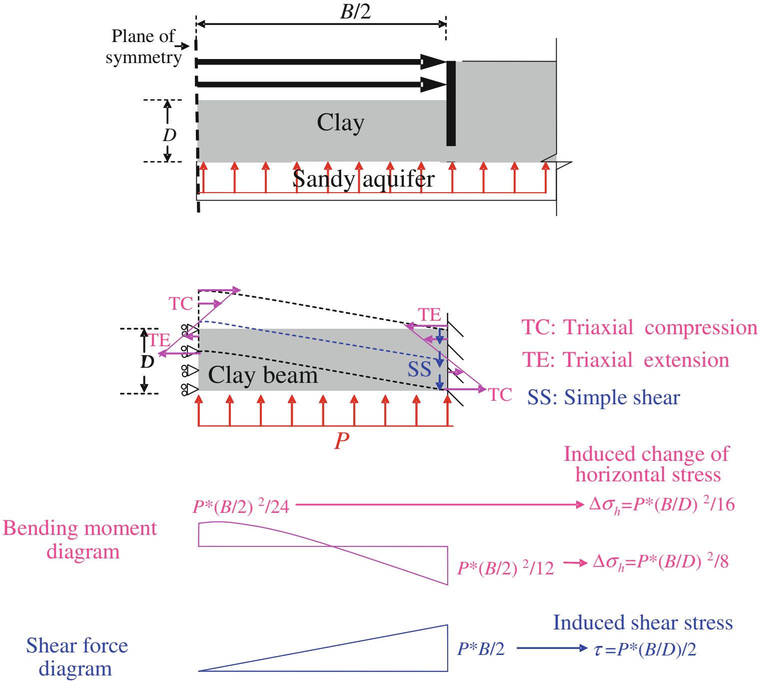

Fig. 9.7 **a** Problem defined; **b** A simplified model for back of envelope calculation

induced in the soil beam. The maximum bending moment is induced near the centre-line of the excavation and adjacent to the soil-wall interface in front of the wall, while the maximum shear force is induced near the soil-wall interface. The calculation further revealed that bending induced change of horizontal stress is function of $(B/D)^2$ while shearing induced shear stress is function of B/D. Therefore, for a narrow excavation (B/D not larger than 1), failure of the soil beam inside excavation is governed by shearing near the-soil wall interface (see Fig. 9.5b). For a wide excavation (B/D larger than 1), failure of the soil beam inside excavation is governed by bending induced change of horizontal stress near the centre-line of the excavation and along the soil-wall interface (see Fig. 9.6b).

9.3.5 Change of Pore Water Pressure in Response to Hydraulic Uplift

It is illustrated in the previous section that the major difference of failure mechanism between relatively narrow and wide excavations is near the middle of the excavation. To better understand this difference, changes of pore water pressure and effective stress near the middle of the two excavations due to hydraulic uplift are compared and discussed in this section and in the subsequent section, respectively.

Figure 9.8 compares change of pore water pressure at two typical locations (see the inset of Fig. 9.8) near the centre-line of a relatively narrow (B/D = 1) and a relatively wide excavation (B/D = 6) in soft clay during hydraulic uplift. Each initial reading refers to computed pore water pressure at the end of excavation (and prior to hydraulic uplift). Calculated pore water pressure (at the end of excavation) with

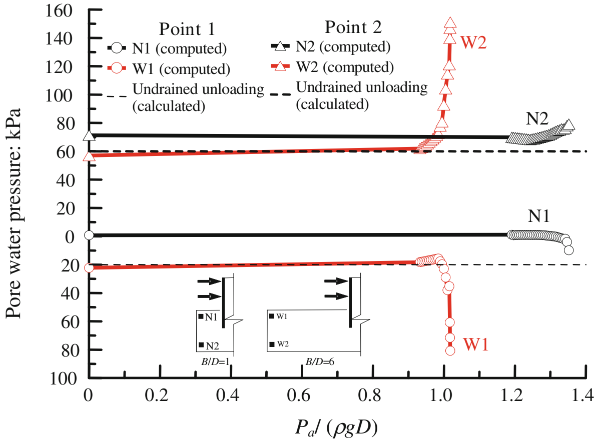

Fig. 9.8 Comparison of changes of pore water pressure between a relatively narrow (B/D = 1) and a relatively wide excavation (B/D = 6) in soft clay ($c_u/(\rho g D)$ = 0.13) during hydraulic uplift

the assumption of undrained unloading due to excavation is also included for reference. It can be seen that in the relatively wide excavation ($B/D = 6$), computed pore water pressures at the end of the excavation (see W1 and W2 in Fig. 9.8) are fairly close to calculated values with the assumption of undrained unloading. This implies an undrained unloading type of response (elastic response) for soil near the centre-line of the relatively wide excavation. On the contrary, computed pore water pressures in the relatively narrow excavation (N1 and N2) reduce less than unloaded total stress due to excavation. This implies that reductions of pore water pressures at N1 and N2 due to undrained unloading should have been partially compensated by positive excess pore water pressure due to shearing. In another word, soil yielding occurs at N1 and N2. It is expected that soil in a relatively narrow excavation tends to approach passive state, which makes soil yield.

Before occurrence of uplift, pore water pressures in both relatively narrow (N1 and N2) and wide excavations (W1 and W2) increase slightly (no more than 3 %) due to dissipation of negative excess pore pressure generated during excavation. Once clay inside excavation is uplifted ($P_a > P_i$), the artesian pressure in excess of apparent overburden pressure serves as a net pressure acting on the bottom of clay inside excavation. Due to this external net pressure, pore water pressures near the bottom of the two excavations both increase (see W2 and N2) but with significantly different magnitudes. In the relatively narrow excavation ($B/D = 1$), the net pressure acting on the bottom of clay inside excavation (up to the ultimate state of hydraulic uplift) is 17 kPa, which accounts for 90 % of increase of pore water pressure (i.e., 23 kPa) at N2 during uplift. This seems to suggest that the increase of pore water pressure at N2 is mainly induced by undrained loading (10 %) and partially results from shearing (10 %). In the relatively wide excavation ($B/D = 6$), the net pressure acting on clay inside excavation (up to the ultimate state of hydraulic uplift) is 3 kPa, which is only 3 % of increase of pore water pressure (94 kPa) at N2 during uplift. As illustrated in Fig. 9.6a), substantial compressive horizontal strain (35 %) is generated near the bottom of the clay inside excavation during uplift of this relatively wide excavation. Accordingly, the increase of pore water pressure at N2 is considered to be mainly induced by the compressive deformation of soil. Near the formation level (along the centerline of the excavation) of the relatively narrow excavation, pore water pressures (at N1) almost remain unchanged during uplift. This is because change of soil strain adjacent to N1 is almost zero during hydraulic uplift, as implied by the observed rigid body movement (see Fig. 9.5a). However, pore water pressure at similar location in the relatively wide excavation (W1) response rather differently to uplift as compared with that at N1. It can be seen that pore water pressures at W1 reduces by 58 kPa due to uplift. This reduction of PWP is very likely to be related to the horizontal tensile strain generated near the formation level of the relatively wide excavation during uplift (see Fig. 9.6a).

9.3.6 Change of Effective Stress Path in Response to Hydraulic Uplift

Figure 9.9 shows effective stress paths of selected elements in both relatively narrow and wide excavations (N1, N2 and W1, W2, respectively) during hydraulic uplift. Since each selected element is located along centre-line of excavation, horizontal and vertical stresses (denoted by σ'_h and σ'_v, respectively) of each element should be principal stresses. Therefore, effective stress paths in Fig. 9.9 are shown in σ'_h–σ'_v space. Rankine's passive and active limiting lines (K_p and K_a, respectively) are also included in the figure for comparison.

During hydraulic uplift, vertical total stress (σ_v) W1 remains constant while its pore water pressure decreases significantly (see Fig. 9.8). This leads to an increase of σ'_v at W1 (see Fig. 9.9). Corresponding to this increase in σ'_v, σ'_h of W1 has to decrease as effective mean normal stress (P') of this lightly over-consolidated soil element either keeps constant (in elastic state) or decreases (in plastic state) while subjected to undrained shearing. As a result of increase in σ'_v and decrease in σ'_h, the locus of stress path of W1 moves towards and reaches K_a line at the end of hydraulic uplift. So W1 fails in compression due to hydraulic uplift (see principal stress in zone 1 in Fig. 9.6b). For the soil element located near the formation level of the relatively narrow excavation (i.e., N1), its stress state prior to hydraulic uplift (immediately after excavation) is closer to K_p line than that of W1. This is expected because during excavation, horizontal pressure at N1 is larger than that at W1 due to its much closer distance to the wall. During the subsequent hydraulic uplift, the locus of stress path of N1 follows a similar trend as that of W1, moving towards K_a line, but the change of σ'_v and σ'_h in N1 is much smaller than at of N1, due to much smaller decrease of pore water pressure (Fig. 9.8). At the end of hydraulic uplift, the stress state of N1 is well below K_a line.

For soil element located near the bottom of the clay inside the relatively wide excavation (i.e., W2), vertical total stress (σ_v) W1 increases slightly (about 3 kPa)

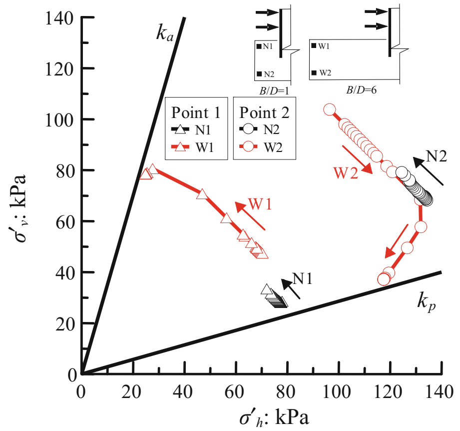

Fig. 9.9 Comparison of effective stress path between a relatively narrow (B/D = 1) and a relatively wide excavation (B/D = 6) in soft clay ($c_u/(\rho g D)$ = 0.13) during hydraulic uplift

while its pore water pressure increases significantly (80 kPa, see Fig. 9.8). A constant reduction of σ_v' at W2 (see Fig. 9.9) is resulted. Before occurrence of yielding in W1 (as marked in Fig. 9.9), σ'_h increases to maintain a constant p'. After soil yields, additional excess pore water pressure should have been generated due to dilation of this slightly over-consolidated clay (*OCR* is about 1.7). Therefore, σ'_h turns to a decrease. The overall locus of stress path of W2 moves towards and touches K_p line at the end of hydraulic uplift. So the failure mode of W2 is extension, as illustrated by principal stress in Fig. 9.6b (zone 2). For the soil element located near the formation level of the relatively narrow excavation (i.e., N1), its stress state prior to hydraulic uplift (immediately after excavation) is closer to K_p line than that of W1. This is expected because during excavation, horizontal pressure at N1 is larger than that at W1 due to its much closer distance to the wall.

During the subsequent hydraulic uplift, the locus of stress path of N1 follows a similar trend as that of W1, moving towards K_a line, but the change of σ'_v and σ'_h in N1 is much smaller than at of N1, due to much smaller decrease of pore water pressure (Fig. 9.8). At the end of hydraulic uplift, the stress state of N1 stays well below K_a line.

9.4 An Alternative Method for Base Stabilisation

The previous section shows that hydraulic pressure required to initiate base instability decreases with excavation width (Fig. 9.4). Although excavation width is pre-determined before construction, width for each excavation step can be narrowed as one wish during construction. Based on this idea, an alternative method is proposed in this study (Fig. 9.10). Figure 9.10a shows a schematic diagram of a multi-propped excavation in clay with an underlying sandy aquifer, prior to excavating the last layer of clay (denoted by shaded area in the figure). It is worth noting that before this last stage, the excavation follows conventional procedures (i.e., alternatively excavating soil and installing props). The proposed method is only applied while excavating the last layer of clay. As illustrated, the last layer of clay is divided into '*n*' zones and is excavated from zone '1' to zone '*n*'. Immediately after excavating zone '1' (Fig. 9.10b), a basement slab is cast above the excavated region (Fig. 9.10c) to compensate vertical unloading due to excavation of zone '1'. Then the same procedures (i.e., alternatively excavating each earth berm and casting basement slab above the excavated area) are repeated till the end of excavation (Fig. 9.10d). By adopting this proposed method, it is hoped to preserve overburden pressure of clay inside excavation. To verify this proposed method, a numerical analysis was carried out, using the calibrated numerical tool in this study.

Assume there is an excavation with *B*/*D* of 2 (*B* = 12 m). Width and height earth beam to be removed in each excavation step is 3 m (with an overburden pressure of 48 kPa) and 1 m, respectively. Sloping angle of each berm is 45°. After removal of each earth berm, a 2-m thick concrete basement slab (with an overburden pressure of 48 kPa) is constructed on the excavated area. The excavation and construction of

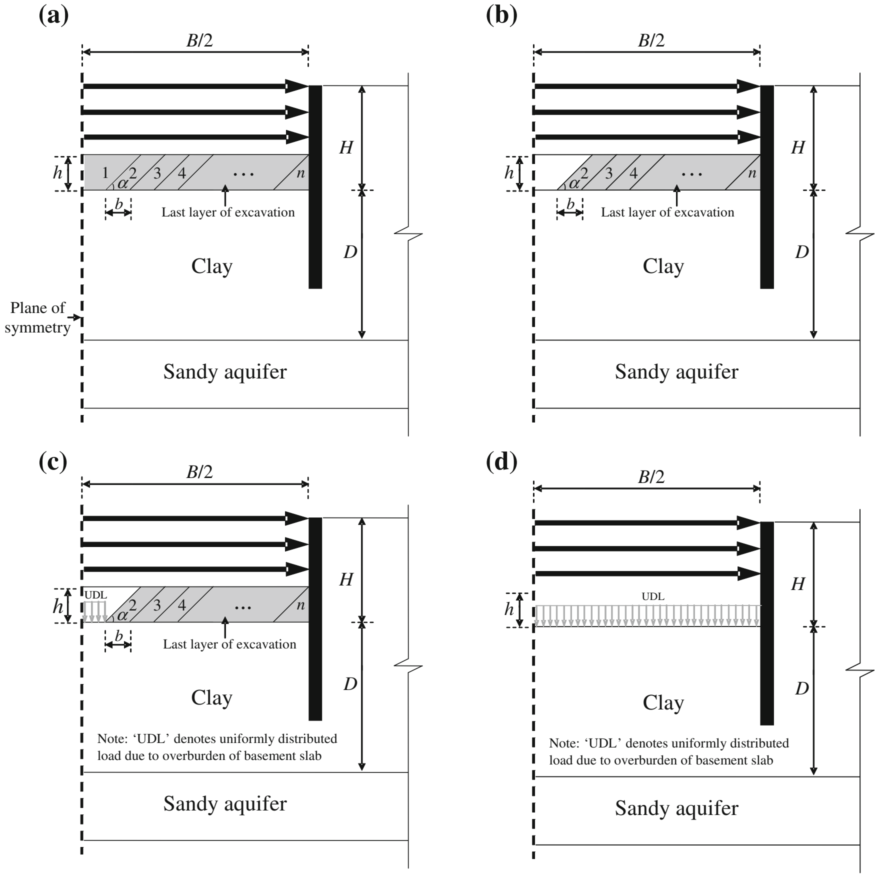

Fig. 9.10 A schematic diagram showing a proposed alternative method for base stabilisation

basement slab are conducted alternatively from the centre of the excavation towards the retaining wall. Apart from numerical analysis adopting this proposed method, another analysis with conventional method (keep excavating earth berms without constructing basement slab till the end of excavation) is also conducted.

Figure 9.11 shows comparison of apparent overburden pressure of clay inside excavation resulted from the proposed method and conventional method. In the same figure, artesian head corresponding to each apparent overburden pressure is also included for reference. In the legend of the figure, the stage 'before excavation' means before the last excavation stage (see Fig. 9.10a). 'E1' and 'S1' refer to stages immediately after excavating the first earth berm and after constructing the first basement slab, respectively. 'E12' means the 12th excavation stage (i.e., the last stage). It can be seen that each excavation stage results in a slight reduction of apparent overburden pressure in the middle of the excavation (less than 3 %), while construction of each basement slab increases apparent overburden pressure slightly

Fig. 9.11 Apparent overburden pressure resulted from excavations carried out by the proposed method and the conventional method

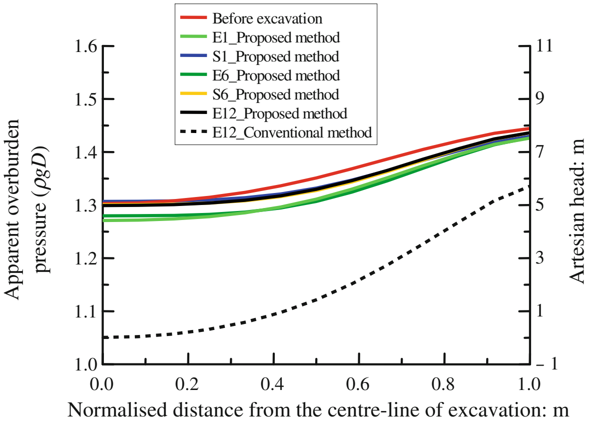

(less than 3 %). By adopting the proposed method, apparent overburden pressure is well preserved even after removing the entire layer of soil (see 'E12_proposed method'), while the conventional method leads to a reduction in apparent overburden pressure of about $0.25\rho gD$ after excavation (see 'E12_conventional method'). At the end of excavation (Stage E12), it can be seen that tolerable artesian heads for the excavation carried out with the proposed method and conventional method are about 5 m and 0 m above the ground surface, respectively. By referring to reported artesian head from case histories worldwide (Table 9.2), it can be seen that artesian heads in most of cities worldwide are smaller than 5 m. By adopting the proposed method, basal resistance against hydraulic uplift is greatly increased.

9.5 Summary and Conclusions

A series of coupled-consolidation finite element analyses were carried out to investigate effect of excavation geometries and undrained shear strength of clay on the initiation and failure mechanism of base instability by hydraulic uplift. Based on the numerical parametric study, the following conclusions can be drawn:

(1) Artesian pressure which initiates base instability (P_i) is affected by ratios of excavation width over thickness of clay inside excavation (B/D) and undrained shear strength over overburden pressure of clay inside excavation ($c_u/(\rho gD)$). P_i reduces as excavation becomes wider, from $1.45\rho gD$ (when $B/D = 0.75$) to ρgD (when $B/D > 3$). For excavations with a given B/D, doubling undrained shear strength of clay can only increase P_i by no more than 9 %. By ignoring effect of excavation width and undrained shear strength, EC 7 (2004) and BSI (1985) are shown to underestimate P_i of relatively narrow excavations.

(2) Failure mechanism is found to vary with B/D but not $c_u/(\rho gD)$. Two typical failure mechanisms are indentified. During uplift of relatively narrow

excavations (i.e., $B/D < 3$), clay inside excavation moves upwards vertically in a rigid body manner while clay outside the excavation remains stationary. Failure occurs due to simple shear between clay inside and outside excavation, as suggested by rotation of principle stresses in the failure zone. The computed ground deformation mechanism is consistent with that measured from a relatively narrow excavation in a centrifuge test reported in Chap. 8.

(3) For relatively wide excavations (i.e., $B/D > 3$), uplift movement of clay inside excavation consists of rotational motion and bending deflection. Bending deflection is suppressed near centre-line of excavation and near the soil-wall interface, where substantial horizontal strains (up to 50 %) are induced and failures occur. Three failure modes are indentified, namely triaxial extension (where horizontal compressive strain occurs), triaxial compression (where horizontal tensile strain occurs) and simple shear (where relative vertical movement occurs due to uplift).

(4) At failure in all analysis undertaken, contribution of mobilised c_u to the ultimate hydraulic uplift resistance is no more than 13 %. However, mobilisation of c_u is accompanied by uplift movement (in the middle of the excavation) of no less than 3.2 $\%D$ (i.e., 384 mm). This is not tolerable according to current design codes such as SMCC (1997) in Shanghai, which specifies a daily maximum allowable basal heave of 2 mm. CIRIA report C515 (Preene et al., 2000), which recommends to make use of undrained shear strength to resist hydraulic uplift, is therefore not applicable to excavations where basal heave should be strictly controlled.

(5) Another alternative method for base stabilisation (apart from use of ‘anti-uplift piles’ discussed in Chap. 8) is proposed. The effectiveness of the proposed method is verified by one numerical analysis. Computed result shows that by adopting the proposed method, the excavation may sustain an additional 5 m of artesian head prior to losing base stability.

References

British Standards Institution (BSI) (1981) Code of practice for site investigations, BS 5930. British Standards Institution, London

British Standards Institution (BSI) (1985) Code of practice for foundations. BS 8004:1986

BS EN 1997-1:2004 (2004) Eurocode 7: Geotechnical design-part 1: general rules. British Standards Institution, London

Clough GW, Reed MW (1984) Measured behavior of braced wall in very soft clay. J Geotech Eng Div ASCE 110(1):1–19

Davies RV (1984) Some geotechnical problems with foundations and basements in Singapore. In Proceedings of the International Conference on Tall buildings, Singapore, 22–26 October

Ervin MC, Benson ND, Morgan JR, Pavlovic N (2004) Melbourne's Southbank Interchange: a permanent excavation in compressible clay. Canadian Geotech J 41(5):861–876

Milligan V, Lo KY (1970) Observations on some basal failures in sheeted excavations. Canadian Geotech J 7(2):136–144

Moore JFA, Longworth T (1979) Hydraulic uplift at the base of a deep excavation in Oxford Clay. Géotechnique 29(1):35–46

Ng CWW, Hong Y, Liu GB, Liu T (2012) Ground deformations and soil-structure interaction of a multi-propped excavation in Shanghai softclays. Géotechnique 62(10):907–921

Preene M, Roberts TOL, Powrie W, Dyer MR (2000) Groundwater control: design and practice. Publication, CIRIA C515

SMCC (1997) Shanghai stand code for design of excavation engineering, DBJ-61-97. Shanghai Municipal Construction Committee, Shanghai

Ward WH (1957) The use of simple relief wells in reducing water pressure beneath a trench excavation. Géotechnique 7(3):134–139

Chapter 10
Conclusions and Future Work

10.1 Summary of This Research

Major objective of this research is to investigate ground deformation, soil-structure interaction and base instability of excavations in clay subjected to hydraulic uplift. Three methodologies, namely field monitoring, centrifuge modelling and finite element analysis, are adopted.

To study ground deformation and soil-structure interaction of multi-propped excavation, a diaphragm wall panel constructed in a greenfield site in Shanghai soft clay was comprehensively instrumented and closely monitored. Monitoring programme includes lateral earth pressure and pore water pressure on both sides of the wall, prop load, lateral wall displacement, lateral ground movement behind the wall and ground surface settlement behind the wall. Measured ground deformations and prop loads in the greenfield site were compared to those measured from densely built area in Shanghai to deduce so-called greenfield effect. Reliability of the measured earth pressures and prop forces was validated by force and moment equilibrium analyses of the instrumented panel. Based on measured lateral earth pressure and pore water pressure, effective stress paths for soil elements on both sides of the wall are deduced and compared to those from reported case histories in stiff clay. A new apparent earth pressure envelope for deep excavations in Shanghai was developed, based on prop loads measured in this site and in other 24 multi-propped excavations in Shanghai. The comprehensively-documented case history was back-analysed by a coupled-consolidation finite element analysis. Based on general agreement between measured and computed results, numerical parametric studies were carried out to investigate and quantify effects of jet grouted prop and prestress on ground deformations and soil-structure interaction, respectively. Moreover, undrained analysis was conducted and compared to the back-analysis for investigating effect of dissipation of pore water pressure during excavation on ground deformations.

Y. Hong and L. Wang, *Deformation and Failure Mechanism of Excavation in Clay Subjected to Hydraulic Uplift*, Advanced Topics in Science and Technology in China, DOI 10.1007/978-3-662-46507-3_10

In the reported case history, observed excessive basal heave during excavation raises concerns of base instability due to hydraulic uplift and leads to motivation of investigating this subject. Dimensional analysis was conducted to propose dimensionless groups relevant to this problem. To investigate effect of these dimensionless groups on basal response subjected to hydraulic uplift, centrifuge modelling and finite element analysis were adopted.

To study base instability associated with hydraulic uplift, a new experimental setup was developed for simulating in-flight multi-propped excavation in clay destabilised by hydraulic uplift in centrifuge. Two tests (with and without anti-uplift piles installed underneath excavation) were carried out to study the initiation and failure mechanisms of excavation base instability due to hydraulic uplift and base stabilisation effect provided by piles. Three-dimensional, coupled-consolidation analyses were conducted to back-analyse and deepen understanding of the centrifuge tests. Based on the calibrated numerical tool, parametric study was carried out to investigate influence of embedment depth of piles on effect of base stabilisation.

By considering dimensionless groups (from dimensional analysis) relevant to this subject, numerical parametric study was performed to investigate and quantify effect of these variables (related to excavation width and undrained shear strength of clay) on the initiation and failure mechanisms of base instability. A new calculation chart is developed for estimating hydraulic pressure required to initiate base instability of excavations with varied geometries and undrained shear strength of clay. Two typical failure mechanisms are identified.

Based on mechanisms revealed by physical and numerical investigation, another alternative method (in addition to 'anti-uplift piles') for base stabilisation is proposed. Effectiveness of the proposed method was verified by numerical analysis.

In this chapter, major conclusions of this research are summerised. Some recommendations for further work are suggested.

10.2 Ground Deformation of Multi-propped Excavation in Soft Clay

10.2.1 Comparison Between Excavation in Greenfield Site and Densely Built Area

The instrumented excavation for this present study was carried out in a park, which was a farmland twenty years ago. Therefore, this site can be considered as a greenfield site. Comparisons were made between excavation-induced deformations in this unique greenfield site (at three instrumented panels) and those in other eight similar multi-propped excavations (with similar ground conditions, retaining systems and construction methods) but constructed in densely built areas in Shanghai (Wang et al. 2005; Tan and Wei 2011; Liu et al. 2011). The following conclusions can be drawn:

(1) At the end of excavation, the maximum lateral wall displacements ($\delta_{h\text{-max}}$) in this greenfield site is about 0.25 % of final excavation depth (H_e), which is comparable to those $\delta_{h\text{-max}}$ values ranging from 0.13 to 0.43 $\%H_e$ measured from eight other similar excavations in densely built areas in Shanghai.

(2) The maximum ground surface settlements ($\delta_{v\text{-max}}$) measured in this greenfield site at the end of excavation ranges from 0.25 $\%H_e$ to 0.32 $\%H_e$ and the influence zone of settlement trough is larger than 2.5 H_e behind the wall. Both measured $\delta_{v\text{-max}}$ and influence zone of ground settlement in the greenfield site are generally larger than those at other eight excavations in densely built areas of Shanghai (with $\delta_{v\text{-max}}$ ranging from 0.01 $\%H_e$ to 0.21 $\%H_e$ and influence zone of settlement trough in the range of $1.0H_e$ to $2.1H_e$). The observed larger magnitude and wider ground settlement troughs in the greenfield site are likely to be due to the lack of stiffening effects provided by adjacent underground structures, foundations and services.

(3) Measured $\delta_{v\text{-max}}/\delta_{h\text{-max}}$ ratios in the greenfield site range from 1.0 to 1.1 while measured $\delta_{v\text{-max}}/\delta_{h\text{-max}}$ ratios in the eight other excavations in densely built areas are in the range of 0.2 to 1.2. This seems to suggest that there is no discernable dependency of greenfield effects on $\delta_{v\text{-max}}/\delta_{h\text{-max}}$ ratios.

10.2.2 *Influence Factors on Ground Deformation of Excavations in Shanghai*

Measured deformations in the case history reported in this study and eight others in Shanghai (Liu et al. 2005; Wang et al. 2005; Tang and Wei 2011; Liu et al. 2011) are shown to be relatively small compared to other similar excavations in soft clay worldwide (Long 2001; Moormann 2004). Major reasons for the relatively small deformations of excavations in Shanghai were considered to be use of jet grouted prop and prestressed props (Liu et al. 2005; Wang et al. 2005; Liu et al. 2011; Ng et al. 2012). These postulations have not been justified, due to difficulties in de-coupling effect of each factor on ground deformation from the field data. Moreover, effect of dissipation of excess pore water pressure on ground deformation should also be considered and quantified.

To investigate key factors governing ground deformation for excavations in Shanghai, five coupled-consolidation finite element analyses were carried out, namely (i) back-analysis; (ii) analysis with only upper half of jet grouted prop; (ii) analysis with only bottom half of jet grouted prop; (iv) analysis without jet grouted prop; (v) analysis without prestressed props. Moreover, one undrained analysis was carried out. Based on these five analyses, it is revealed that:

(1) Due to presence of jet grouted prop in front of the wall, excavation-induced $\delta_{h\text{-max}}$ and $\delta_{v\text{-max}}$ may have been reduced by 66 and 81 %, respectively.
(2) Reduction of deformation benefits more from presence of the upper half of jet grouted prop than the bottom half. This is because the upper half of grouted prop is located near the formation level of the excavation, where most significant shear strain is induced by excavation.
(3) Compared to effect of grouted prop, effects of use of prestressed props on reduction of $\delta_{h\text{-max}}$ and $\delta_{v\text{-max}}$ are much less significant (i.e., with percentage reduction of about 1 %).
(4) In this relatively rapid excavation (daily excavation rate is about 0.37 m deep), additional $\delta_{h\text{-max}}$ and $\delta_{v\text{-max}}$ due to dissipation of excess pore water pressure are no more than 2 %.

10.3 Soil-Structure Interaction of Multi-propped Excavation in Soft Clay

10.3.1 Lateral Total Earth Pressure

Before excavation, lateral total earth pressures (σ_h) on both sides of the panel generally fall between the at-rest earth pressure and the theoretical concrete pressure envelope proposed by Ng (1992). The concreting process prior to excavation had resulted in an increase in the lateral earth pressure adjacent to the panel. This is in contrast to the observed significant reduction in lateral stress after the construction of diaphragm wall in overconsolidated clay (Tedd et al. 1984; Milligan 1970).

During excavation, σ_h on the retained side within the propped region decreased first and then increased when the excavation level proceeded below their corresponding elevations. The increase in lateral earth pressure is a result of upward shear stress transfer (soil arching) during excavation.

At the end of excavation, σ_h behind the wall generally stayed above Rankine's active limiting boundary (K_a line). σ_h on the retained side should have been increased by construction of diaphragm wall and soil arching during excavation.

10.3.2 Pore Water Pressure

Different from measured pore water pressure near formation level of an excavation in stiff clay (Ng 1998), negative excess pore water pressure was not measured and computed in this study in soft clay. Negative excess pore water pressure due to unloading inside the excavation in soft clay could have been cancelled out by positive excess pore water pressure due to shearing and inward movement of the wall.

10.3.3 Effective Stress Path

Based on measured earth pressures and pore water pressures at the soil-wall interface, effective stresses were deduced. After diaphragm walling, the lateral earth pressure coefficient (effective stress) at the soil-wall interface was increased by a factor of more than 1.4. During excavation, the stress paths for the retained soil within the propped region generally moved towards the passive state, instead of the active state, during the last few stages of main excavation. On the excavated side, stress paths for soil located near the formation level approached the passive failure state. Numerical back-analysis reveals that the grouted prop near the formation level prevents the ground in front of the wall from experiencing passive failure.

By comparing of effective stress paths around excavations in soft clay and stiff clay, two major differences are found:

(1) Construction of diaphragm wall in soft clay in this study results in an increase in σ'_h at soil wall interface while it leads to substantial reductions in σ'_h in stiff clay (Tedd et al. 1984; Milligan 1970). This is because the lateral fresh concrete pressure (Ng 1992) is larger than the lateral earth pressure in soft clay but is smaller than that in stiff clay.

(2) After excavation, increase in σ'_h behind the wall within propped region (probably due to upward shear stress transfer) was observed in this study and other case histories in soft clay (Ou et al. 1998; Tanaka 1994; Liu et al. 2005). On the contrary, case histories in stiff clay (Tedd et al. 1984; Milligan 1970; Richards et al. 2007) show that σ'_h within propped region decreased after excavation. This is probably because excavation in stiffer soil induces relatively larger stress release, which is less likely to be compensated by subsequent upward shear stress transfer.

10.3.4 Effect of Jet Grouted Prop on Soil-Structure Interaction

Numerical analyses reveal that at the end of the excavation, about 18 % of passive load in front of the wall is transferred from soil to grouted prop. Because of the load sharing by grouted prop, mobilised undrained shear strength of clay in front of the wall is reduced by 20 % (on average). Potential passive failure of soil adjacent to the formation level of the excavation has been prevented. Reduced shearing and yielding of soil in front of the wall lead to a decrease of the maximum lateral wall displacement and maximum ground surface settlement by 66 and 81 %, respectively.

10.3.5 Prop Load

A new apparent earth pressure envelope was developed based on the maximum prop loads measured at 25 excavations (including this study) in Shanghai. The maximum apparent earth pressure in Shanghai is found to be $1.1\gamma H_e$ (γ and H_e denote bulk density of soil and final excavation depth, respectively). In this greenfield site, the maximum apparent earth pressures are generally larger than the average values from the other 24 excavations in Shanghai.

10.4 Excavation Base Instability Associated with Hydraulic Uplift

10.4.1 Initiation of Base Instability

Base instability is initiated while down-thrust of clay inside excavation becomes smaller than up-thrust acting on the bottom of the clay due to hydraulic uplift. As revealed by numerical analyses, the down-thrust consists of overburden weight of clay inside excavation and resultant downward shear force due to friction along clay-wall interface. The former is a constant while the latter depends on excavation width over thickness of clay inside excavation ratio (*B/D*) and undrained shear strength of clay (c_u). For excavations in soft clay (i.e., c_u = 35 kPa), hydraulic pressure (P_i) required to initiate base instability decreases from 1.45 times of overburden pressure of clay inside excavation (P_o) in a relatively narrow excavation (*B/D* = 0.75) to P_o in a relatively with excavation (*B/D* = 3). By doubling c_u (i.e., c_u = 70 kPa), the maximum percentage increase in P_i is about 9 %. When *B/D* is larger than 3, effect of friction along clay-wall interface on down-thrust of clay inside excavation becomes negligible. Accordingly, base instability can be initiated once hydraulic pressure exceeds overburden pressure of clay inside excavation ($P_i = P_o$).

A new calculation chart is developed for estimating P_i for excavations with varied *B/D* and c_u, based on results of numerical parametric study.

10.4.2 Failure Mechanisms

Failure mechanism is found to vary with *B/D* but not c_u. Two typical failure mechanisms are indentified. For relatively narrow excavations (i.e., *B/D* < 3), clay inside excavation is uplifted upwards vertically in a rigid body manner while clay outside the excavation remains stationary. Relative movement between clays inside and outside excavations leads to simple shear failure along soil-wall interface. For relatively wide excavations (i.e., *B/D* > 3), uplift movement of clay inside excavation consists of rotational motion and bending deflection. Bending deflection near the centre-line of the excavation and adjacent to soil-wall interface leads to significant changes of horizontal effective stress (σ'_h) at corresponding regions. As a result, triaxial compression and triaxial extension types of failure occur where σ'_h decreased and increased, respectively.

10.4.3 Proposed Alternative Methods for Base Stabilisation

Two alternative methods for base stabilisation were proposed in this present study. Basic concept of both methods is to increase down-thrust of clay inside excavation, one by preserving overburden of clay while the other by mobilising downward shaft friction of piles installed inside excavation. Brief introduction and effectiveness of the two proposed methods are given below.

- *Method 1: Preservation of overburden pressure of clay inside excavation*
  To preserve overburden pressure of clay inside excavation, it is proposed to alternatively excavating relatively narrow earth berm and constructing basement slab (providing surcharge) on the previously excavated area. Effectiveness of this proposed method is demonstrated by one numerical analysis. Computed result shows that by using the proposed method, increased P_i can be equivalent to an artesian head of 5 m.
- *Method 2: Anti-uplift pile*
  The other method is to use piles which are readily installed as part of top-down construction inside excavation, to resist uplift of clay between piles. Based on physical and numerical investigation, it is revealed that presence of piles does not alter P_i, but can reduce uplift movement significantly (i.e., 80 %) by mobilising c_u at soil-pile interface.

10.4.4 Verification of 'Idealised Modelling Technique'

It is worth noting that in centrifuge tests and numerical analyses in this study, excavation and hydraulic uplift are simulated separately, in order to differentiate both effects on excavation base instability. It is understood that in practice, excavation is carried out with presence of hydraulic pressure. The 'idealised modelling technique' adopted in this study has been verified against numerical analysis with 'rigorous modelling technique' (excavation with presence of hydraulic pressure). It is shown that computed results from both modelling techniques are almost identical.

10.5 Recommendations for Further Work

10.5.1 Further Verification of 'Greenfield Effect'

In this study, measured ground settlement due to excavation in a greenfield site is shown to have lager magnitude and influence zone than those reported from eight similar excavations in densely built areas in Shanghai soft clay. To further confirm the observed 'greenfield effect', more field data from greenfield sites should be collected or measured.

Given the 'greenfield effect' is further confirmed, systematic study is required to investigate and quantify effect of adjacent existing underground utilities on excavation-induced ground deformation.

10.5.2 Further Verification of 'Idealised Modelling Technique'

As concluded, the 'idealised modelling technique' (simulating excavation prior to hydraulic uplift) adopted in this study has been verified against numerical analysis with 'rigorous modelling technique' (excavation with presence of hydraulic pressure). This conclusion should be further confirmed by experimental evidence. One more centrifuge test with 'rigorous modelling technique' should be carried out and compared to the test with 'idealised modelling technique'.

10.5.3 Alternative Methods for Base Stabilisation

In this study, two alternative methods for base stabilisation were proposed (i.e., surcharge loading method and 'anti-uplift pile'). Effectiveness of the surcharge loading method depends on weight of basement slab (i.e., thickness). It may not be applicable where thickness of basement slab is constrained. While 'anti-uplift piles' may not be readily available inside excavation which is not conducted by top-down construction. Under this circumstance, it may be costly to construct 'anti-uplift piles' only for base stabilisation purpose. Therefore, it is desirable to propose more alternative methods for base stabilisation.

References

Liu GB, Ng CWW, Wang ZW (2005) Observed performance of a deep multi-strutted excavation in Shanghai soft clays. J Geotech Geoenviron Eng ASCE 131(8):1004–1013

Liu GB, Jiang J, Ng CWW, Hong Y (2011) Deformation characteristics of a 38 m deep excavation in soft clay. Can Geotech J 48(12):1817–1828

Long M (2001) Database for retaining wall and ground movements due to deep excavation. J Geotech Geoenviron Eng ASCE 127(3):203–224

Milligan V, Lo KY (1970) Observations on some basal failures in sheeted excavations. Can Geotech J 7(2):136–144

Moormann C (2004) Analysis of wall and ground movements due to deep excavations in soft soil based in a new worldwide database. Soils Found 44(1):87–98

Ng CWW (1992) An evaluation of soil-structure interaction associated with a multi-propped excavation. PhD thesis, University of Bristol

Ng CWW (1998) Observed performance of multi-propped excavation in stiff clay. J Geotech Geoenviron Eng ASCE 124(9):889–905

Ng CWW, Hong Y, Liu GB, Liu T (2012) Ground deformations and soil-structure interaction of a multi-propped excavation in Shanghai soft clays. Géotechnique 62(10):907–921

Ou CY, Liao JT, Lin HD (1998) Performance of diaphragm wall construction using top-down method. J Geotech Geoenviron Eng ASCE 124(9):798–808

Richards DJ, Powrie W, Roscoe H, Clark J (2007) Pore water pressure and horizontal stress changes measured during construction of a contiguous bored pile multi-propped retaining wall in Lower Cretaceous clays. Géotechnique 57(2):197–205

Tan Y, Wei B (2011) Observed behavior of a long and deep excavation constructed by cut-and-cover technique in Shanghai soft clay. J Geotech Geoenviron Eng ASCE 138(1):69–88

Tanaka H (1994) Behavior of a braced excavation in soft clay and the undrained shear strength for passive earth pressure. Soils Found 34(1):53–64

Tedd P, Chard BM, Charles JA, Symons IF (1984) Behaviour of a propped embedded retaining wall in stiff clay at Bell Common Tunnel. Géotechnique 34(4):513–532

Wang ZW, Ng CWW, Liu GB (2005) Characteristics of wall deflections and ground surface settlements in Shanghai. Can Geotech J 42(5):1243–1254

Index

Y. Hong and L. Wang, *Deformation and Failure Mechanism of Excavation in Clay Subjected to Hydraulic Uplift*, Advanced Topics in Science and Technology in China, DOI 10.1007/978-3-662-46507-3